



Quantifying Feedback from Narrow Line Region Outflows in Nearby Active Galaxies.

III. Results for the Seyfert 2 Galaxies Markarian 3, Markarian 78, and NGC 1068^{*†}

Mitchell Revalski¹ , Beena Meena² , Francisco Martinez³ , Garrett E. Polack² , D. Michael Crenshaw² ,
Steven B. Kraemer⁴ , Nicholas R. Collins⁵ , Travis C. Fischer⁶ , Henrique R. Schmitt⁷ , Judy Schmidt⁸ ,
W. Peter Maksym⁹ , and Marc Rafelski^{1,10}

¹ Space Telescope Science Institute, 3700 San Martin Drive, Baltimore, MD 21218, USA; mrevalski@stsci.edu

² Department of Physics and Astronomy, Georgia State University, 25 Park Place, Suite 605, Atlanta, GA 30303, USA

³ Center for Relativistic Astrophysics, School of Physics, Georgia Institute of Technology, Atlanta, GA 30332, USA

⁴ Institute for Astrophysics and Computational Sciences, Department of Physics, The Catholic University of America, Washington, DC 20064, USA

⁵ Telophase Corporation at NASA's Goddard Space Flight Center, Code 667, Greenbelt, MD 20771, USA

⁶ AURA for ESA, Space Telescope Science Institute, 3700 San Martin Drive, Baltimore, MD 21218, USA

⁷ Naval Research Laboratory, Washington, DC 20375, USA

⁸ Designer/Developer for the Astrophysics Source Code Library

⁹ Harvard-Smithsonian Center for Astrophysics, 60 Garden Street, Cambridge, MA 02138, USA

¹⁰ Department of Physics and Astronomy, Johns Hopkins University, Baltimore, MD 21218, USA

Received 2020 October 15; revised 2020 December 29; accepted 2021 January 12; published 2021 April 5

Abstract

Outflows of ionized gas driven by active galactic nuclei (AGN) may significantly impact the evolution of their host galaxies. However, determining the energetics of these outflows is difficult with spatially unresolved observations that are subject to strong global selection effects. We present part of an ongoing study using Hubble Space Telescope and Apache Point Observatory spectroscopy and imaging to derive spatially resolved mass outflow rates and energetics for narrow-line region outflows in nearby AGN that are based on multi-component photoionization models to account for spatial variations in gas ionization, density, abundances, and dust content. This expanded analysis adds Mrk 3, Mrk 78, and NGC 1068, doubling our earlier sample. We find that the outflows contain total ionized gas masses of $M \approx 10^{5.5} - 10^{7.5} M_{\odot}$ and reach peak velocities of $v \approx 800 - 2000 \text{ km s}^{-1}$. The outflows reach maximum mass outflow rates of $\dot{M}_{\text{out}} \approx 3 - 12 M_{\odot} \text{ yr}^{-1}$ and encompass total kinetic energies of $E \approx 10^{54} - 10^{56} \text{ erg}$. The outflows extend to radial distances of $r \approx 0.1 - 3 \text{ kpc}$ from the nucleus, with the gas masses, outflow energetics, and radial extents positively correlated with AGN luminosity. The outflow rates are consistent with in situ ionization and acceleration where gas is radiatively driven at multiple radii. These radial variations indicate that spatially resolved observations are essential for localizing AGN feedback and determining the most accurate outflow parameters.

Unified Astronomy Thesaurus concepts: Active galaxies (17); Active galactic nuclei (16); AGN host galaxies (2017); Emission line galaxies (459); Seyfert galaxies (1447); Markarian galaxies (1006); Supermassive black holes (1663); Galaxy kinematics (602); Galaxy winds (626); Interstellar medium wind (848)

Supporting material: machine-readable table

1. Introduction

1.1. Feedback from Outflows in Active Galaxies

Outflows of ionized and molecular gas may play an important role in the coevolution of active galactic nuclei (AGN) and their host galaxies by regulating supermassive black hole (SMBH) accretion rates and evacuating reservoirs of potential star-forming gas from galaxy bulges (Ciotti & Ostriker 2001; Hopkins et al. 2005; Kormendy & Ho 2013; Heckman & Best 2014; Fiore et al. 2017; Cresci & Maiolino 2018; Harrison et al. 2018; Storchi-Bergmann & Schnorr-Müller 2019; Veilleux et al. 2020; Laha et al. 2021). Outflows are observed over a range of spatial scales, and those connecting the subparsec central engine to the kiloparsec-scale

galaxy environment can be found in the narrow-line region (NLR), which is composed of ionized gas $\sim 1 - 1000 + \text{ pc}$ from the SMBH with densities of $n_{\text{H}} \approx 10^2 - 10^6 \text{ cm}^{-3}$ (Peterson 1997). These outflows are of particular interest because they extend from the smallest scales that can be spatially resolved in nearby galaxies (parsecs from the SMBH) to bulge-galaxy scales where they may affect galactic evolution. We can determine whether or not NLR outflows are providing significant feedback to their host galaxies through quantifying their impact by measuring the outflowing mass (M) and velocity (v) over a spatial extent (δr). These parameters are then used to calculate properties including mass outflow rates ($\dot{M} = Mv/\delta r$), kinetic energies ($E = 1/2 Mv^2$), kinetic energy flow rates ($\dot{E} = 1/2 \dot{M}v^2$), momenta ($p = Mv$), and momenta flow rates ($\dot{p} = \dot{M}v$).

Determining these quantities accurately for individual AGN has generally faced two obstacles. First, spatially unresolved observations only allow these properties to be determined globally, averaging over the spatial extent of the outflow to approximate the energetics with a single mass, velocity, and radial extent. Second, several methods for estimating the mass

* Based on observations made with the NASA/ESA Hubble Space Telescope, obtained from the Data Archive at the Space Telescope Science Institute, which is operated by the Association of Universities for Research in Astronomy, Inc., under NASA contract NAS 5-26555. These observations are associated with program Nos. 5140, 5754, 7404, 7573, and 8480.

† Based in part on observations obtained with the Apache Point Observatory 3.5 m telescope, which is owned and operated by the Astrophysical Research Consortium.

of the ionized gas that involve different assumptions yield a range of mass estimates for the same galaxies. While global techniques allow the mass to be quickly estimated for a large number of targets with available data, the underlying assumptions have not been critically examined for a large sample and in some cases are subject to systematics that overestimate the energetics by $\sim 1\text{--}3$ dex (Karouzos et al. 2016; Bischetti et al. 2017; Venturi & Marconi 2020). Recently, these systematic uncertainties are being better understood by utilizing spatially resolved imaging and spectroscopy to map how the outflows change as a function of distance from the nucleus (Durré & Mould 2018, 2019; Venturi et al. 2018; García-Bernetete et al. 2021; Comerón et al. 2021; Trindade Falcão et al. 2021).

To tackle the second issue of determining accurate gas masses, we have developed a technique using multi-component photoionization models that match the emission line spectra, which tightly constrains the gas densities and allows us to calculate the mass of the ionized outflows with high precision (Collins et al. 2009; Crenshaw et al. 2015; Revalski 2019). We have an ongoing program to quantify the energetic impact of spatially resolved NLR outflows that was launched in an initial investigation by Crenshaw et al. (2015) focused on NGC 4151. This bright, prototypical Seyfert 1 galaxy displays outflow velocities up to $\sim 800 \text{ km s}^{-1}$ with an outflow gas mass of $3 \times 10^5 M_{\odot}$ that reaches a peak mass outflow rate of $\sim 3 M_{\odot} \text{ yr}^{-1}$. This outflow rate is higher than the mass accretion rate onto the SMBH and the outflow rate seen for UV/X-ray absorbers at smaller radii (Crenshaw & Kraemer 2012), indicating the potential importance of NLR outflows as a feedback mechanism.

We expanded this work to higher luminosities by conducting a similar analysis for Mrk 573 (Revalski et al. 2018a) and Mrk 34 (Revalski et al. 2018b). These galaxies display more extended and energetic outflows than NGC 4151, highlighting the need for a systematic study of nearby AGN across a range of luminosities, SMBH masses, galaxy types, and environments (e.g., Rojas et al. 2020; Yesuf et al. 2020). In this study, we expand upon our earlier investigation with analyses of the nearby Seyfert galaxies Mrk 3, Mrk 78, and NGC 1068. These AGN were selected because they display clear signatures of outflow (Fischer et al. 2013, 2014) and have the archival Hubble Space Telescope (HST) spectroscopy and imaging required to implement our modeling technique. We complete the analysis for Mrk 78 in this paper and draw modeling results from Ruiz et al. (2001) and Collins et al. (2005, 2009) for Mrk 3 and Kraemer & Crenshaw (2000a, 2000b) for NGC 1068 to calculate the outflow energetics. We describe the observations (Section 2), analysis (Section 3), modeling (Section 4), and calculations (Section 5) for these new targets, as well as the results (Section 6), discussion (Section 7), and conclusions (Section 8) for the entire sample.

1.2. Characteristics of the Sample

The galaxies Mrk 3, Mrk 78, and NGC 1068 have been the subject of multiwavelength investigations in the radio (Ulvestad & Wilson 1984), optical (Fischer et al. 2013), UV (Ferland & Osterbrock 1986), and X-ray (Awaki et al. 1991). As shown in Figure 1, Mrk 3 is a Seyfert 2 galaxy with an S0 classification and a backward S-shaped NLR that is produced by external fueling as cold gas from a nearby companion galaxy is ionized within the AGN radiation field (see Gnilka et al. 2020 and references therein for an extensive review). The

Seyfert 2 galaxy Mrk 78 has an SB classification and intertwined radio and optical features obscured by a thick dust lane (Adams 1973; De Robertis 1987; Pedlar et al. 1989; Capetti et al. 1994; Ramos Almeida et al. 2006; Jackson & Beswick 2007; Fischer et al. 2011; Liu et al. 2017). The nearest Seyfert 2 galaxy, NGC 1068, has been studied extensively to understand the physical processes at work in AGN at the smallest resolvable spatial scales (e.g., Antonucci & Miller 1985; Pogge & De Robertis 1993; Jaffe et al. 2004; García-Burillo et al. 2014; May et al. 2014; Kraemer et al. 2015; May & Steiner 2017). The HST color-composite images of these AGN are presented in Figure 1, and their physical properties are provided in Table 1.

2. Observations

2.1. Hubble Space Telescope

The archival HST spectroscopy and [O III] imaging used in this study were obtained with the Space Telescope Imaging Spectrograph (STIS), Wide Field and Planetary Camera 2 (WFPC2), and Faint Object Camera (FOC). We retrieved calibrated data (DOI:10.17909/t9-4581-8p50) from the Mikulski Archive at the Space Telescope Science Institute (MAST) and combined multiple dithered spectroscopic exposures using the Interactive Data Language (IDL) and IRAF (Tody 1986, 1993) for imaging.

To investigate jet–gas interactions within the NLR, Mrk 78 was observed extensively with HST/STIS using the G140L, G430L, G430M, and G750M gratings with a $52'' \times 0.''2$ slit (Program ID 7404, PI: M. Whittle; Whittle & Wilson 2004; Whittle et al. 2005; Rosario 2007). As shown in Figure 1, the observations consist of four long-slit pointings labeled A, B, C, and D. Slits A–C are parallel and spatially offset from one another at a position angle (PA) of 88° , while slit D intersects these near the nucleus at a PA of 66° .

In our analysis, we focus on the medium-dispersion G750M observations to trace the ionized gas kinematics, as well as the low-dispersion G430L observations that contain the diagnostic emission lines required for photoionization modeling. Details of the observations are provided in Table 2, and extracted spectra for each slit are shown in Figure 2. For [O III] imaging, we use FOC observations through the F502M filter with F550M for continuum subtraction (Program ID 5140, PI: F. Macchetto).

Both Mrk 3 and NGC 1068 have been well studied, and we use portions of our previous investigations in this analysis. The spectroscopic results for Mrk 3 are based on HST/STIS long-slit observations using the G140L, G230L, G430L, and G750L gratings at a PA of 71° with the $52'' \times 0.''1$ slit (Program ID 8480, PI: S. Kraemer) that are described in Collins et al. (2005). The galaxy NGC 1068 was observed with the same gratings along a PA of 202° and the $52'' \times 0.''1$ slit (Program ID 7573, PI: S. Kraemer), with the details of the observations presented in Crenshaw & Kraemer (2000). For [O III] imaging, we use an FOC observation of Mrk 3 through the F502M filter and F550M for continuum subtraction (Program ID 5140, PI: F. Macchetto). The galaxy NGC 1068 was observed with the WFPC2/PC using the F502N filter with F547M for continuum subtraction (Program ID 5754, PI: H. Ford). Details for the images of Mrk 3, Mrk 78, and NGC 1068 are provided in Table 2.

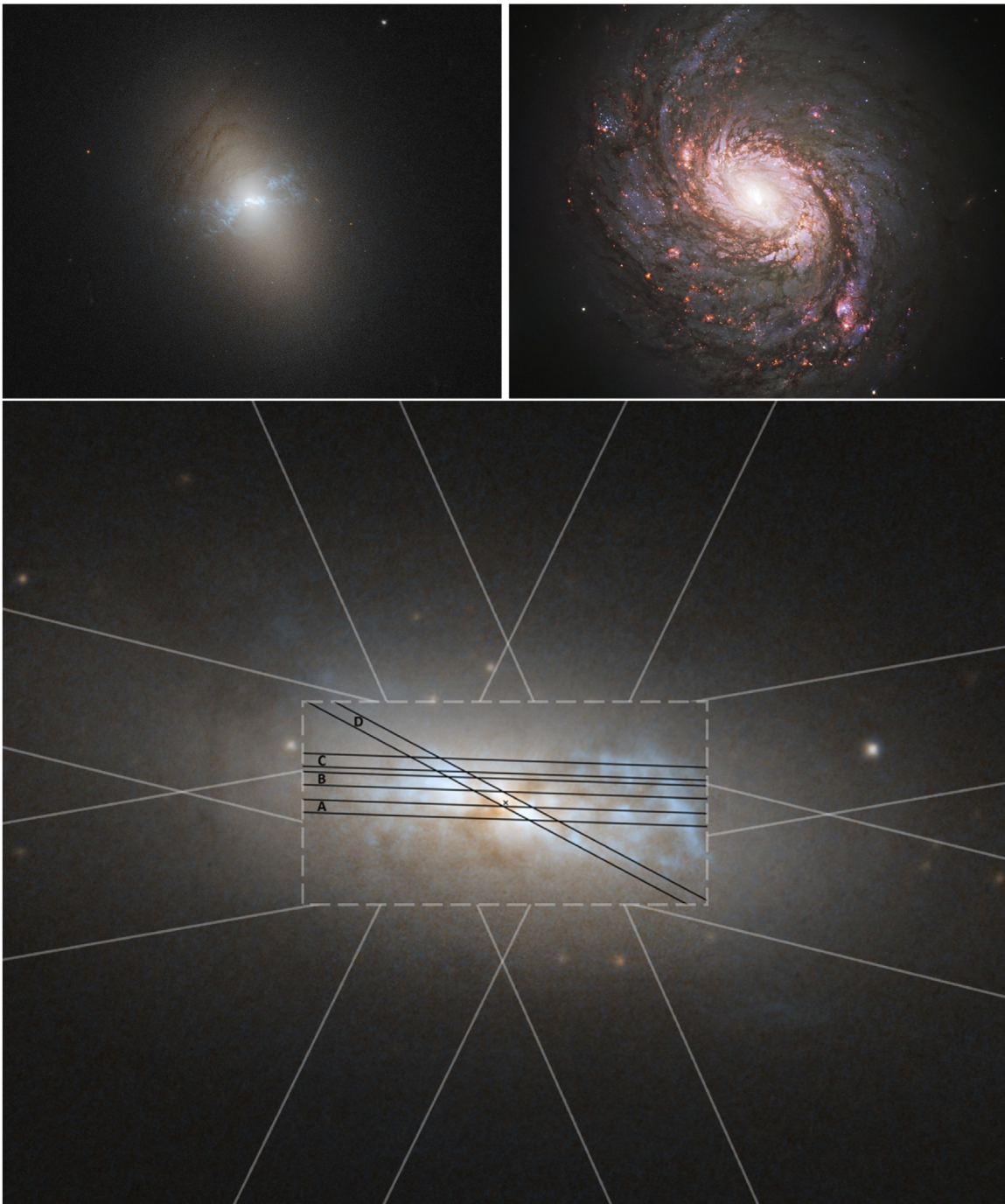


Figure 1. Shown are HST color-composite images of Mrk 3 (top left; $56'' \times 45''$, WPC2/WF F814W, WPC2/PC F606W), NGC 1068 (top right; $144'' \times 114''$, ACS/WFC F658N, F814W, WPC2 F606W, F450W), and Mrk 78 (bottom; $15'' \times 12''$, ACS/WFC F814W, STIS/CCD 50CCD, FOC/96 F502M). North is up and east is to the left in all panels, and high-resolution images are available at <https://www.flickr.com/photos/geckzilla/>. The image of Mrk 78 has a $6'' \times 3''$ inset rectangle, and the solid lines delineate the locations and slit widths of the observations, with HST/STIS ($0''.2$ wide slit) in black and APO/DIS ($2''.0$ wide slit) in gray. The HST and APO slits spatially overlap and are truncated at the dashed rectangle for visibility. The cross marks the location of the optical and infrared continuum peak (Ramos Almeida et al. 2006; Fischer et al. 2011). Bright white-blue emission near the nuclei shows AGN-ionized gas in the NLR and ENLR. Diffuse white is primarily stellar continuum emission, and the dark lanes and patches are due to dust. The red clumps in NGC 1068 are H II regions created by star formation outside of the nucleus.

2.2. Apache Point Observatory

We observed Mrk 78 with the Dual Imaging Spectrograph (DIS) on the Apache Point Observatory (APO) 3.5 m telescope to obtain deep spectroscopy of the ionized gas outside of the narrow HST slits. The DIS gathers spectra in blue and red channels simultaneously, enabling us to characterize the kinematics and

physical conditions of gas in the extended NLR (ENLR) on scales $>1''$ using a variety of emission lines surrounding $H\beta$ and $H\alpha$. We collected spectra using a $2''$ wide slit at PAs of 24° , 76° , 100° , and 152° to sample near the major and minor axes, with the photometric major axis of the host galaxy at a PA of $\sim 84^\circ$ (Schmitt & Kinney 2000). Details of the observations and instruments are presented in Table 2.

Table 1
Physical Properties of the Active Galaxy Sample

Catalog Name	Redshift (21 cm)	Distance (Mpc)	Scale (pc arcsec ⁻¹)	Inclination (deg)	log(L_{bol}) (erg s ⁻¹)	log(M_{BH}) (M_{\odot})	$L_{\text{bol}}/L_{\text{Edd}}$ (unitless)	References (Cols. 5, 6, 7)	Analysis Refs.
(1)	(2)	(3)	(4)	(5)	(6)	(7)	(8)	(9)	(10)
NGC 4151	0.0033	13.3	67.4	20	43.9	7.6	0.01	1, 2, 3	12
NGC 1068	0.0038	16.0	77.6	40	45.0	7.2	0.50	4, 5, 5	*
Mrk 3	0.0135	56.6	274.5	64 ^a	45.3	8.7	0.04	6, 6, 5	*
Mrk 573	0.0172	72.0	349.1	38	45.5	7.3	0.75	7, 8, 5	8
Mrk 78	0.0372	154.2	747.4	55	45.9	7.9	0.79	9, *, 5	*
Mrk 34	0.0505	207.9	1007.7	41	46.2	7.5	3.98	10, 10, 11	10

Note. Columns are (1) target name, (2) 21 cm redshift from the NASA/IPAC Extragalactic Database, (3) Hubble distance, (4) spatial scale assuming $H_0 = 71 \text{ km s}^{-1} \text{ Mpc}^{-1}$, (5) host galaxy inclination, (6) bolometric luminosity estimated from [O III] imaging, (7) black hole mass, and (8) corresponding Eddington ratio ($L_{\text{bol}}/L_{\text{Edd}}$) calculated using $L_{\text{Edd}} = 1.26 \times 10^{38} (M/M_{\odot}) \text{ erg s}^{-1}$. Column (9) gives the references for columns (5)–(7), and column (10) provides the reference for our mass outflow modeling.

^a The host galaxy inclination is 33°, but the outflows occupy a gas disk at an inclination of 64°, as described in Gnilka et al. (2020).

References. (1) Das et al. (2005), (2) Crenshaw & Kraemer (2012), (3) Bentz et al. (2006), (4) Das et al. (2006), (5) Woo & Urry (2002), (6) Collins et al. (2009), (7) Fischer et al. (2017), (8) Revalski et al. (2018a), (9) Schmitt & Kinney (2000), (10) Revalski et al. (2018b), (11) Oh et al. (2011), (12) Crenshaw et al. (2015), (*) this work.

We reduced the APO spectroscopy using IRAF (Tody 1986, 1993) and standard techniques, including bias subtraction, image trimming, bad-pixel replacement, flat-fielding, Laplacian edge cosmic-ray removal (van Dokkum 2001), image combining, and sky-line subtraction. Wavelength calibration was completed using comparison arc lamp images, and velocities were corrected to heliocentric. Flux calibration was completed using Oke standard stars (Oke 1990) and the airmass at mid-exposure. Finally, the DIS dispersion and spatial axes are not perpendicular, so we fit a line to the galaxy continuum and resampled the data so measurements of emission lines from the same pixel rows correspond to the same spatial locations.

3. Analysis

3.1. Spectral Fitting

We fit Gaussian profiles to the emission lines in our spectra at each location along the slits to derive the spatially resolved gas kinematics and emission line flux ratios required to generate photoionization models. We use a Bayesian fitting routine that we developed based on the Importance Nested Sampling algorithm in MultiNest (Feroz & Hobson 2008; Feroz et al. 2009, 2019; Buchner et al. 2014) that we have used in a variety of kinematic studies (Fischer et al. 2018). This procedure determines the number of meaningful kinematic components and characterizes each as a Gaussian with a variable velocity centroid, width, and height above the underlying continuum. The data are fit with an increasing number of kinematic components until the Bayesian likelihood criteria $\ln(Z)$ is <5 between models, at which point the simpler model with fewer components is selected. A detailed description of this process is given in Fischer et al. (2017), and we present examples of one-, two-, and three-component fits to the HST data in Figure 3.

We extracted spectra in 0".2 and 0".42 intervals along the slits for the HST and APO data, respectively, and adopted a minimum peak-flux signal-to-noise ratio (S/N) of >2 above the continuum for positive line detections. This over-samples the APO data, as flux is shared between adjacent pixels due to the seeing; however, the radial gradients are preserved, and we only derive the amplitude of the galaxy rotational velocity and

the large-scale extent of the ionized gas using these ground-based data.

We ensure that the fits to each emission line sample the same kinematic components of the gas by using a spectral template technique that fixes the line centroids and widths based on freely varying fits to the strong, velocity-resolved $\text{H}\alpha$ $\lambda 6563 \text{ \AA}$ + [N II] $\lambda \lambda 6548, 6584 \text{ \AA}$ emission lines in the HST/STIS G750M spectra. While the [O III] $\lambda \lambda 4959, 5007 \text{ \AA}$ emission lines are brighter, we found that $\text{H}\alpha$ produced fits with smaller residuals than when using [O III] in the lower-dispersion G430L spectra and did not require independently fitting the G430M spectra. The line widths were constrained to minimum values of the line spread functions (LSFs) for each grating, measured from calibration lamp exposures, and a maximum FWHM of 2000 km s^{-1} .

For all of the other emission lines, the fits are scaled from $\text{H}\alpha$ to preserve the same intrinsic velocity widths and centroids and account for the instrument LSFs between different gratings. The height of each Gaussian component is free to vary to enclose the total emission line flux, and the uncertainties are given by the residuals between the data and fits. This process allows us to accurately fit weak diagnostic emission lines that are important for comparison with photoionization models, but small differences in the intrinsic line widths may be neglected (see Section 3.1 of Revalski et al. 2018a).

We further constrain the fitting process by fixing the relative height ratios of doublet lines to their theoretical values (Osterbrock & Ferland 2006). Specifically, [O III] $\lambda \lambda 5007/4959 = 3.01$, [O I] $\lambda \lambda 6300/6363 = 3.0$, and [N II] $\lambda \lambda 6584/6548 = 2.95$. We fit blended or closely spaced lines such as $\text{H}\alpha$ and [N II], the [S II] doublet, and others simultaneously and fix the relative separations of these lines relative to $\text{H}\alpha$ to their laboratory values. We followed a similar procedure for the APO/DIS spectroscopic data, using the strong [O III] $\lambda 5007 \text{ \AA}$ emission line to trace the large-scale gas kinematics, because in this case, the blue and red spectra have essentially the same wavelength resolution.

3.2. Ionized Gas Kinematics

In Fischer et al. (2011), we used HST/STIS G430M observations of [O III] to explore the NLR kinematics

Table 2
Summary of Observations

Target Name	Observing Facility	Instrument Name	Proposal ID	Observation ID	Date (UT) (y-m-d)	Exposure Time (s)	Grating or Filter	Slit ID	Spectral Dispersion (\AA pixel^{-1})	Wavelength Range (\AA)	Spatial Scale (arcsec pixel^{-1})	Position Angle (deg)	Spatial Offset ^a (arcsec)	Mean Airmass	Mean Seeing (arcsec)
Mrk 78	HST	STIS	7404	O4DJ02030	1998-02-28	2052	G430L	A	2.73	2900–5700	0.051	88.05	0.125
Mrk 78	HST	STIS	7404	O4DJ02060	1998-02-28	1730	G430L	B	2.73	2900–5700	0.051	88.05	−0.27
Mrk 78	HST	STIS	7404	O4DJ02090	1998-03-01	2052	G430L	C	2.73	2900–5700	0.051	88.05	−0.55
Mrk 78	HST	STIS	7404	O4DJ04010	1998-03-01	1643	G430L	D	2.73	2900–5700	0.051	61.56	−0.05
Mrk 78	HST	STIS	7404	O4DJ02010	1998-02-28	1100	G750M	A	0.56	6480–7054	0.051	88.05	0.125
Mrk 78	HST	STIS	7404	O4DJ02040	1998-02-28	1199	G750M	B	0.56	6480–7054	0.051	88.05	−0.27
Mrk 78	HST	STIS	7404	O4DJ02070	1998-02-28	1172	G750M	C	0.56	6480–7054	0.051	88.05	−0.55
Mrk 78	HST	STIS	7404	O4DJ04030	1998-03-01	1320	G750M	D	0.56	6480–7054	0.051	61.56	−0.05
Mrk 78	HST	STIS	7404	O4DJ01020	1997-11-16	120	MIRVIS	1640–10270	0.051
Mrk 78	HST	FOC	5140	X2580303T	1994-03-19	800	F502M	4645–5389	0.014
Mrk 78	HST	FOC	5140	X2580304T	1994-03-19	1196	F550M	5303–5726	0.014
Mrk 78	APO	DIS	2016-01-02	2137	B1200	...	0.615	4257–5517	0.42	24	...	1.36	1.48
Mrk 78	APO	DIS	2016-01-02	2137	R1200	...	0.580	6020–7180	0.40	24	...	1.36	1.55
Mrk 78	APO	DIS	2014-10-25	2400	B1200	...	0.615	4760–6000	0.42	76	...	1.20	1.52
Mrk 78	APO	DIS	2014-10-25	2400	R1200	...	0.580	6002–7162	0.40	76	...	1.20	1.80
Mrk 78	APO	DIS	2015-02-19	2400	B1200	...	0.615	4481–5721	0.42	100	...	1.18	1.48
Mrk 78	APO	DIS	2015-02-19	2400	R1200	...	0.580	6002–7162	0.40	100	...	1.18	1.55
Mrk 78	APO	DIS	2015-12-03	2700	B1200	...	0.615	4278–5518	0.42	152	...	1.49	1.52
Mrk 78	APO	DIS	2015-12-03	2700	R1200	...	0.580	6020–7180	0.40	152	...	1.49	1.55
Mrk 3	HST	FOC	5140	X2580103T	1994-03-20	750	F502M	4645–5389	0.014
Mrk 3	HST	FOC	5140	X2580104T	1994-03-20	1196	F550M	5303–5726	0.014
NGC 1068	HST	WFPC2/PC	5754	U2M30103T	1995-01-17	300	F502N	4969–5044	0.045
NGC 1068	HST	WFPC2/PC	5754	U2M30104T	1995-01-17	600	F502N	4969–5044	0.045
NGC 1068	HST	WFPC2/PC	5754	U2M30101T	1995-01-17	140	F547M	5060–5885	0.045
NGC 1068	HST	WFPC2/PC	5754	U2M30102T	1995-01-17	300	F547M	5060–5885	0.045

Notes. A summary of the observations and data used in this study. The columns list the observing facility, instrument, HST proposal ID, MAST archive observation ID, observation date, exposure time, grating (for spectra) or filter (for imaging), four HST slit names, spectral dispersion, wavelength range (for spectra) or bandpass (for imaging, defined as the range where the system throughput exceeds 1%), spatial resolution, PAs of the slits, spatial offset from the continuum peak, airmass, and seeing. The seeing was calculated by measuring the FWHM of the brightness profiles of the standard stars along the slit. All HST values are defined in their respective instrument handbooks (McMaster et al. 2008; Riley 2017), with the exact STIS spatial scale quoted as $0.05078'' \text{ pixel}^{-1}$.

^a Observations with nonzero values are spatially offset from the nucleus. The data may be obtained from MAST using the following DOI:10.17909/t9-4581-8p50.

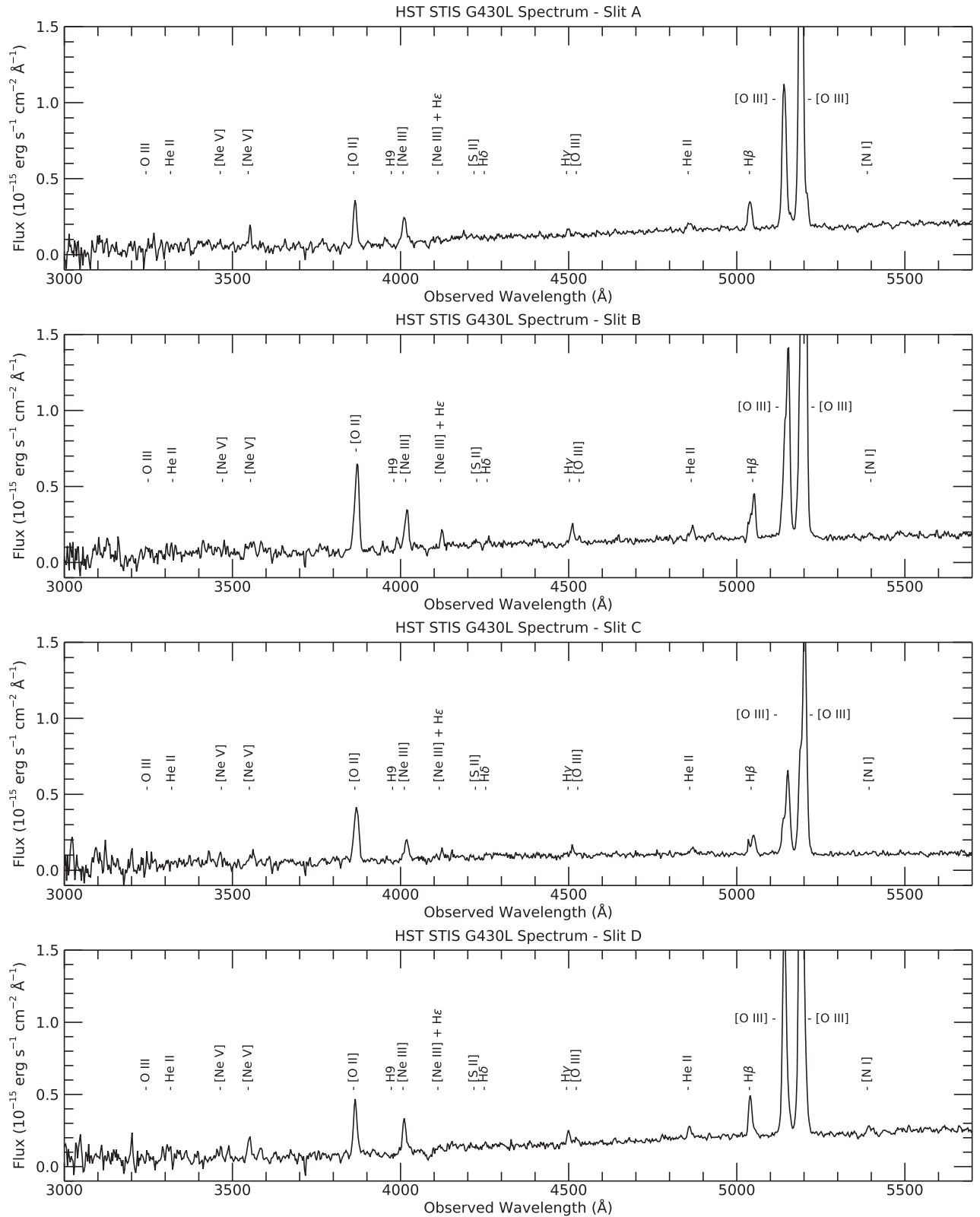


Figure 2. Shown are Mrk 78 spectral traces of the nuclear emission spatially summed over $\sim 1''$, with the positions of the emission lines labeled. The spectra are shown at observed wavelengths and from top to bottom are HST/STIS G430L and G750M for slits A, B, C, and D.

of Mrk 78. The four slit positions are labeled A, B, C, and D in Figure 1, and additional details are given in Fischer et al. (2011). We expand the analysis for Mrk 78 by fitting the HST/STIS G750M observations to determine the $H\alpha$ kinematics for the same slit positions. We present velocity

maps of the kinematic components in Figure 4 and plots of the gas velocity centroids, line widths, and fluxes for the HST and APO observations in Figures 5 and 6. There are a maximum of three kinematic components at each spatial location.

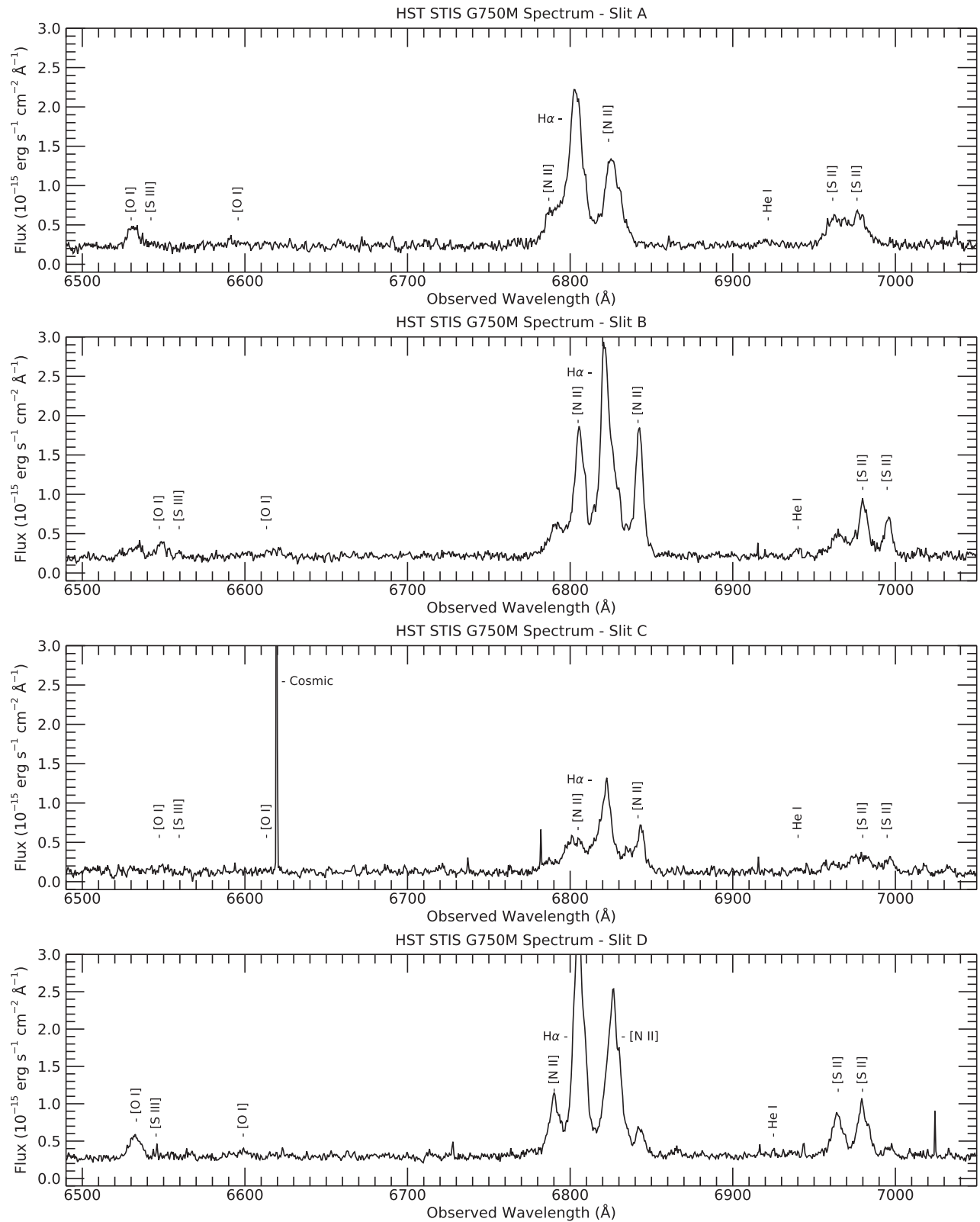


Figure 2. (Continued.)

Overall, the HST/STIS $H\alpha$ kinematics presented in Figures 4 and 5 show excellent agreement with the [O III] kinematics in Fischer et al. (2011). Variations in velocity, line width, and flux between the individual slits indicate the clumpy

and inhomogeneous nature of the gas and outflows. High-velocity outflows reaching $\sim 1000 \text{ km s}^{-1}$ are observed in all slits to radial extents of $\sim 1''$ ($\sim 750 \text{ pc}$), with moderate-velocity outflows up to $\sim 500 \text{ km s}^{-1}$ reaching out to $\sim 3''$ ($\sim 2.2 \text{ kpc}$)

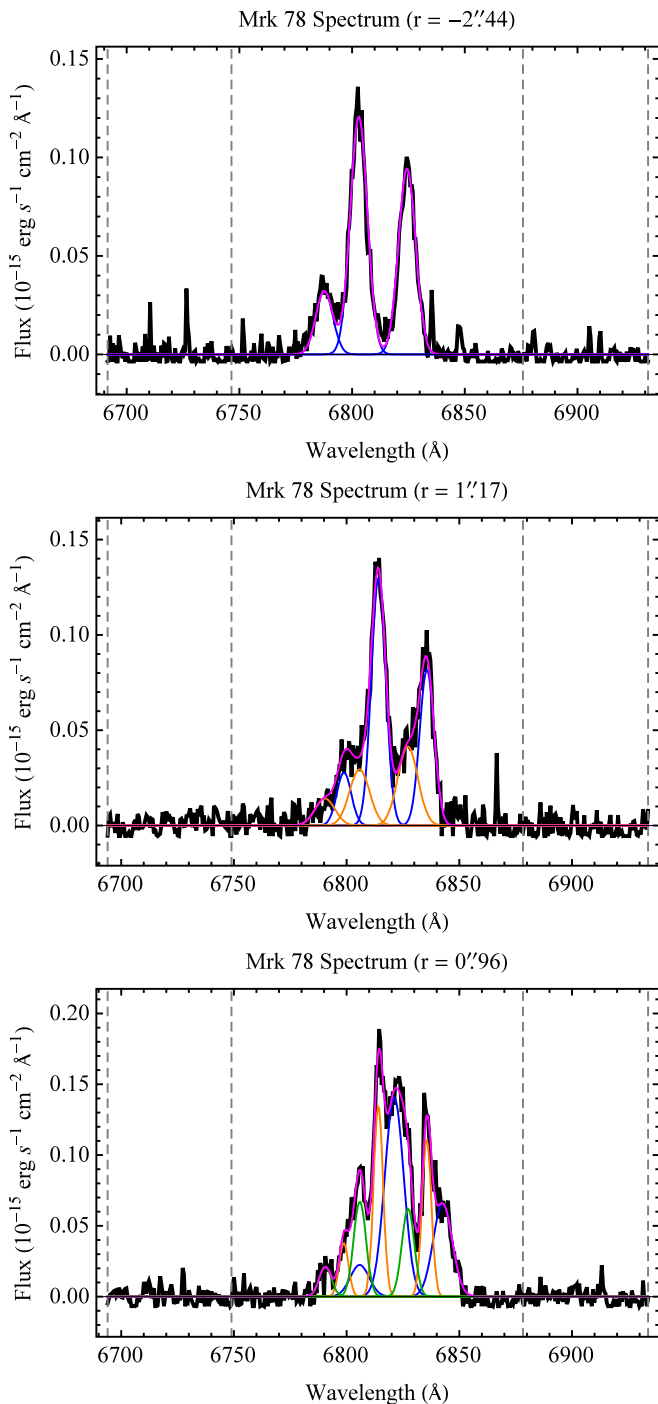


Figure 3. Examples of the $H\alpha + [N II]$ Bayesian spectral decomposition process for Mrk 78 HST/STIS G750M observations, which determine whether one (top), two (middle), or three (bottom) meaningful kinematic components exist at each spatial location along the slits. The spectra are fit with an increasing number of components until the difference between competing models is less than a Bayesian criterion, as described in the text. The data are shown in black, the continuum fit regions between gray dashed lines, and the first, second, and third components in order of decreasing peak flux are shown in blue, orange, and green, respectively. The sum of all Gaussian kinematic components is shown in magenta.

from the nucleus. The large FWHM values in excess of $\sim 250 \text{ km s}^{-1}$ are consistent with outflows dominating the kinematics to at least $3''$ from the central SMBH.

The APO [O III] kinematics in Figures 4 and 6 are dominated by rotational motion between $\sim 5''$ and $\sim 15''$ (~ 4 – 11 kpc) with

$\text{FWHM} < 250 \text{ km s}^{-1}$. The observed velocity amplitudes are $\sim 100 \text{ km s}^{-1}$ along PAs of 76° and 100° , both of which are close to the photometric major axis of $\sim 84^\circ$. The velocity centroids are blueshifted in the west and redshifted in the east, and based on the above photometric major axis and inclination of the host galaxy disk (55° ; Schmitt & Kinney 2000), the deprojected velocity amplitude of the galaxy’s rotation is approximately 125 km s^{-1} .

The higher velocities and FWHM of the brightest [O III] component inside of $5''$ – $7''$ (depending on the PA) are indicative of the outflow seen in the STIS data, although the velocity amplitudes near the center are somewhat reduced due to averaging over a much larger projected area within the APO/DIS slits. Interestingly, the APO observations are able to isolate a high-velocity (600 – 900 km s^{-1}), lower-flux redshifted component out to $\sim 5''$ ($\sim 4 \text{ kpc}$) from the nucleus and a similar (300 – 500 km s^{-1}) low-flux blueshifted component. These low-flux, high-velocity components indicate that weak outflows extend to radial distances of $\sim 4 \text{ kpc}$, beyond those detected in the HST observations. This is caused by the narrower slits and shorter integration times of the HST spectroscopy, highlighting the effect of sensitivity on the determination of outflow extents (Kang & Woo 2018). While these components have high velocities, they are significantly lower in flux than the primary outflow and rotational components, indicating a smaller contribution to the outflow mass and energy budget.

We describe the complex kinematics of the ionized gas in the NLR of Mrk 3 in Gnilka et al. (2020) based on HST/STIS, APO/DIS, and Gemini Near-Infrared Integral Field Spectrometer (NIFS) observations. As shown in Figure 7 of Gnilka et al. (2020), the HST/STIS [O III] and $H\alpha$ radial velocities peak at blueshifted and redshifted values of $\sim 700 \text{ km s}^{-1}$ close ($\sim 0''.2$) to the central SMBH and return to systemic values at a distance of $\sim 1''.2$ ($\sim 330 \text{ pc}$), similar to the pattern seen in Mrk 78. The NIFS observations cover the entire NLR over a span of $3''$ and show emission line knots with a range of blueshifted and redshifted velocities up to -1200 and $+1500 \text{ km s}^{-1}$, respectively. At larger radii, the APO kinematics show a transition from outflow to rotation between $1''.2$ and $4''$ and a rotational component thereafter in the ENLR that reaches up to $\sim 20''$ ($\sim 5.4 \text{ kpc}$) from the nucleus.

The kinematics of the NLR in NGC 1068 are described in detail by Das et al. (2005), based on an analysis of [O III] emission in multiple parallel HST/STIS observations using the G430M grating. The blueshifted and redshifted radial velocities of the ionized gas increase from near systemic to ~ 1000 – 1500 km s^{-1} at a projected distance of $1''.9$ ($\sim 150 \text{ pc}$) from the SMBH, followed by a decline to systemic velocity at around $5''.6$ ($\sim 435 \text{ pc}$). At larger distances, the radial velocities are near systemic out to at least $8''$ ($\sim 580 \text{ pc}$) and display correspondingly low FWHM that are indicative of rotational kinematics.

3.3. Biconical Outflow Models

To determine the mass outflow parameters, we need the true space velocities and distances of the ionized gas from the SMBHs for each AGN. We can obtain these by adopting kinematic models of the outflows whose geometries determine deprojection factors for the velocities and distances. We adopt biconical outflow models derived in our previous studies of Mrk 3 (Ruiz et al. 2001; Crenshaw et al. 2010a), Mrk 78 (Fischer et al. 2011), and NGC 1068 (Das et al. 2005). In these

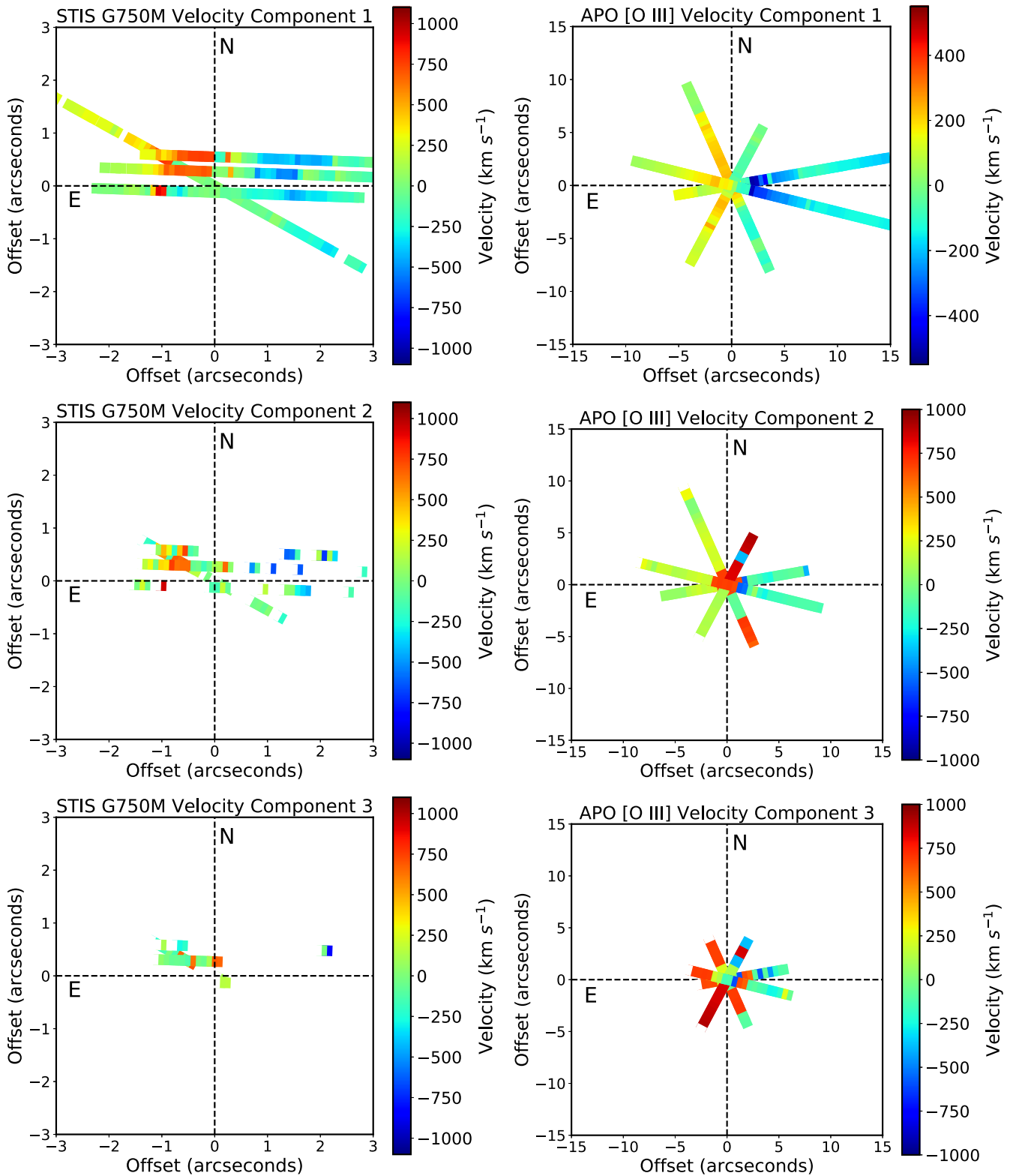


Figure 4. The Mrk 78 velocity maps of the ionized gas derived from fits to the HST/STIS H α (left) and APO/DIS [O III] (right) spectroscopy. The panels show the individual kinematic components for the highest (top), intermediate (middle), and lowest (bottom) flux components. The strong redshifts and blueshifts in the upper left panel indicate the presence of ionized outflows, while the lower-amplitude velocities in the upper right panel (which has a smaller color-bar range) trace the larger-scale rotation of gas in the ENLR. The HST panels span $\pm 3''$, and the slits are $0''.2$ in width; the APO panels span $\pm 15''$, and the slits are $2''.0$ in width but are represented by $1''.0$ wide rectangles for visibility.

models, the outflows increase from zero velocity at the SMBH to a maximum value (v_{\max}) at a turnover radius (r_{turn}) and then decline to the systemic (rotational) value at a maximum

distance (r_{\max}). The symmetric 3D biconical models are then sampled along the same PAs as the HST/STIS slits, and the model parameters are varied until a match is obtained with the

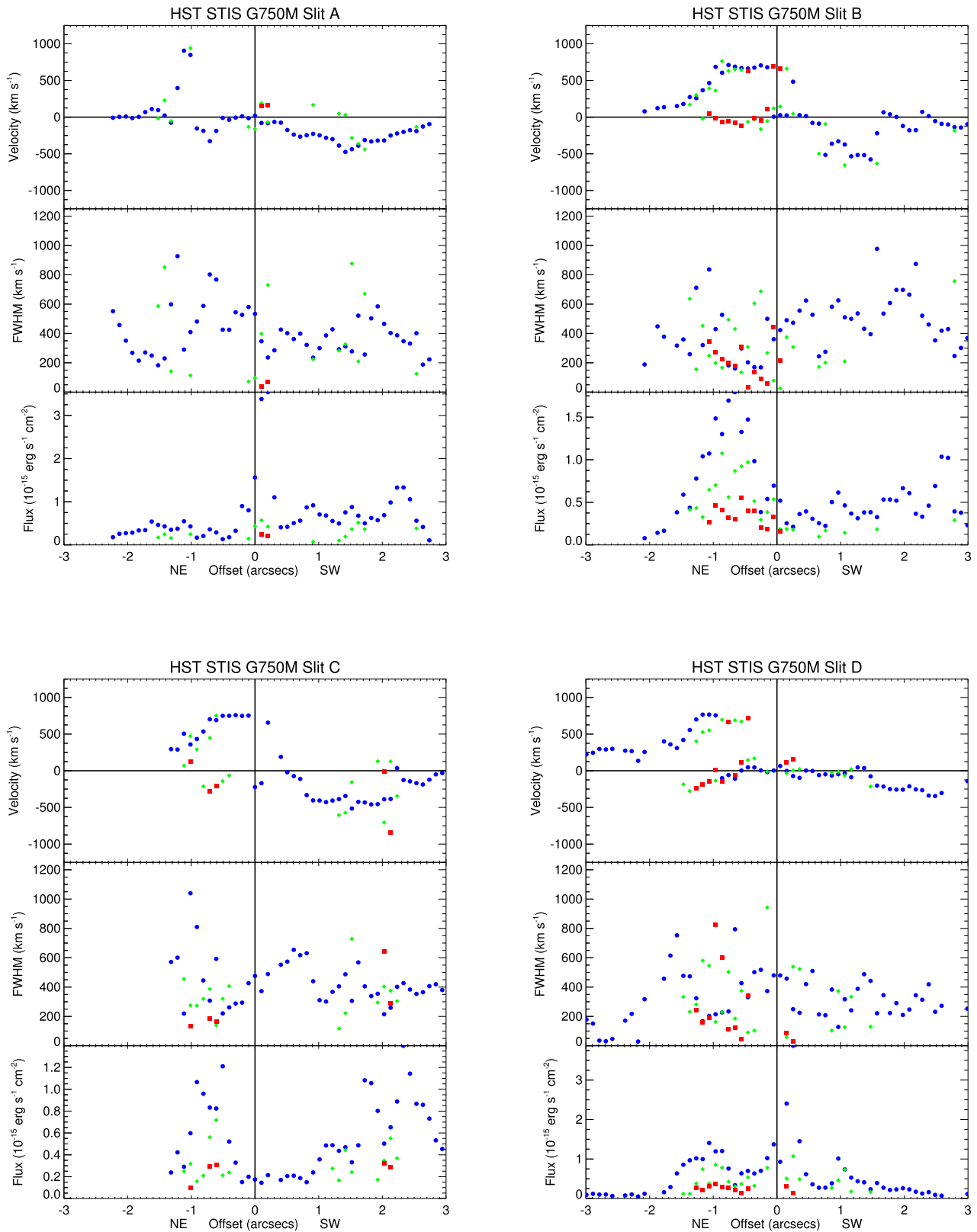


Figure 5. The Mrk 78 observed velocity centroids (top), FWHM (middle), and integrated line fluxes (bottom) for the $H\alpha$ $\lambda 6563$ emission line in each of the four HST/STIS G750M spectral observations. The points are color-coded from strongest to weakest peak flux in the order of blue circles, green diamonds, and red squares. Slits A, B, and C are at a PA of 88° , while slit D is at 61° east of north.

overall trend of the radial velocities. The bicones are hollow along their central axes and defined by minimum and maximum half-opening angles (HOAs).

In our previous studies of Mrk 573 (Revalski et al. 2018a) and Mrk 34 (Revalski et al. 2018b), we adopted a variation of this model where the outflows within the ionizing bicone travel

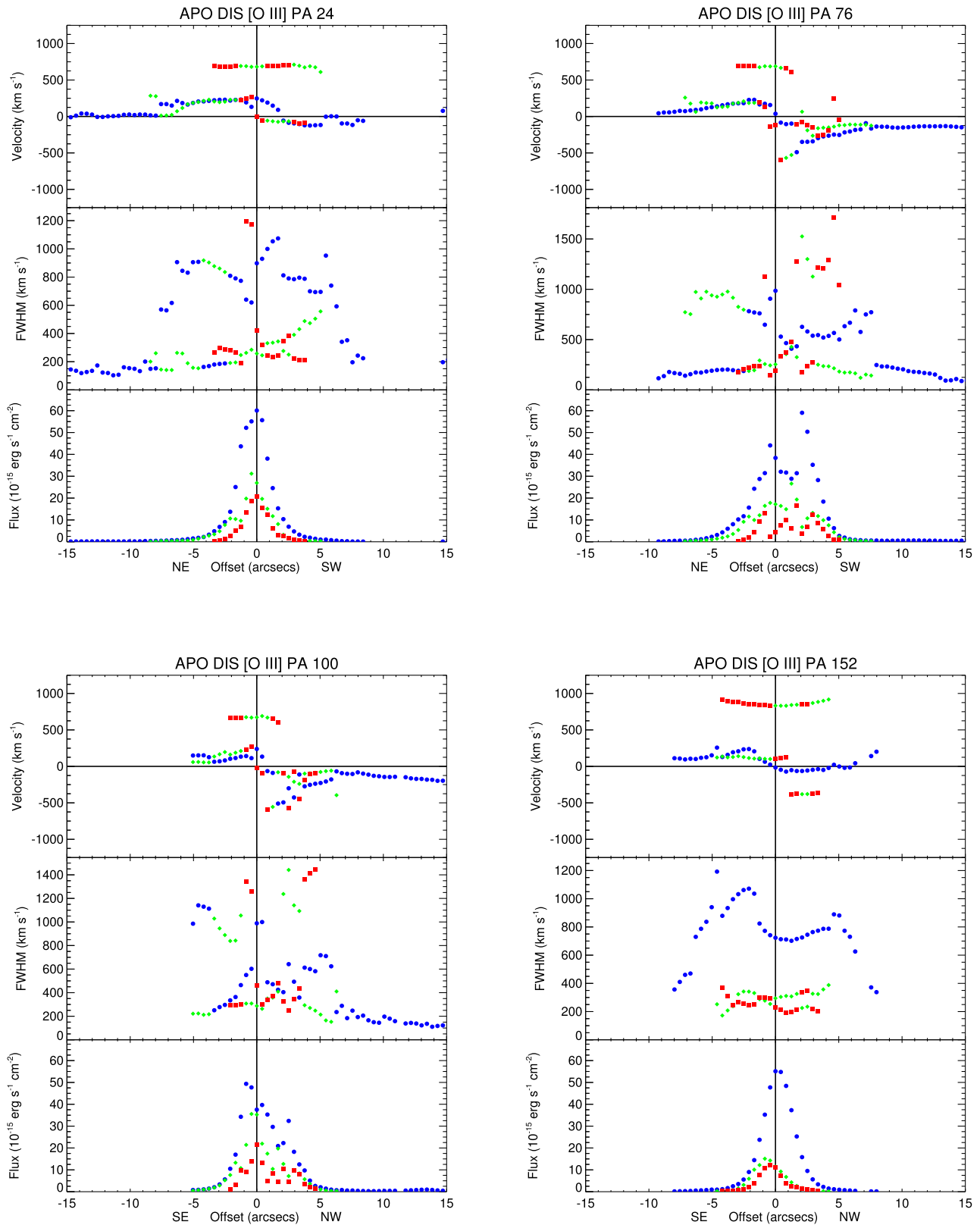


Figure 6. The Mrk 78 observed velocity centroids (top), FWHM (middle), and integrated line fluxes (bottom) for the [O III] $\lambda 5007$ emission line in each of the four APO/DIS long-slit observations. The points are color-coded from strongest to weakest peak flux in the order of blue circles, green diamonds, and red squares. From upper left to lower right are PA 24°, 76°, 100°, and 152° east of north.

along the disk of the galaxy rather than the edges that was based on evidence that they originate from ionized dust spirals in the host galaxy disk (Fischer et al. 2017). However, this

variation is not appropriate for Mrk 3 or NGC 1068 because the nearly equal blueshifts and redshifts on either side of the SMBH are consistent with flows along the sides of a mostly

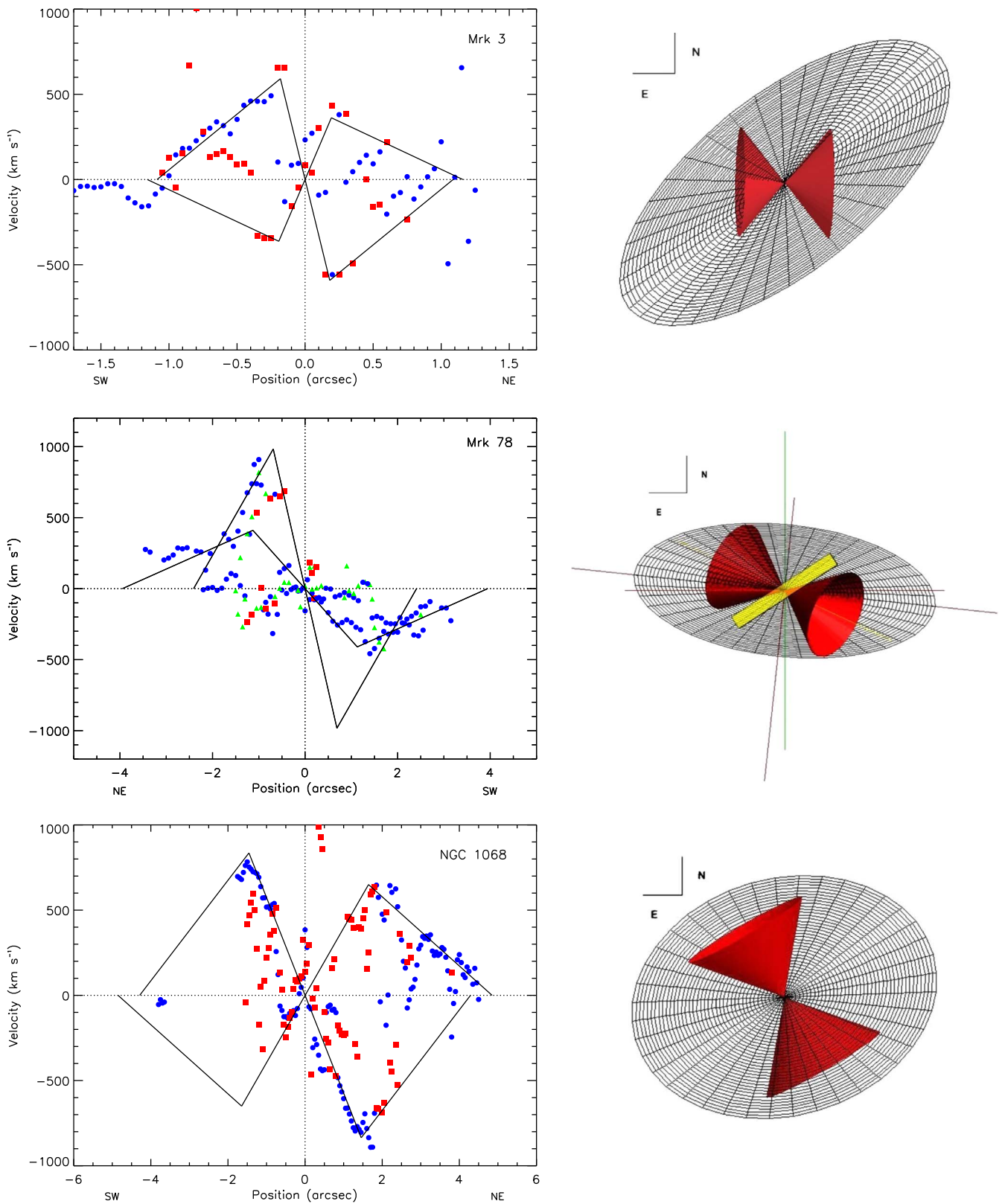


Figure 7. Biconical outflow model fits (left; black lines) and geometries (right) for the observed gas kinematics of Mrk 3 (top), Mrk 78 (middle), and NGC 1068 (bottom). Radial velocities are color-coded as in Figures 5 and 6. The geometric models highlight the outer opening angle of the ionized biconical outflows (red cones) and the host galaxy disk (black annuli) and have been reproduced from Crenshaw et al. (2010a), Fischer et al. (2011), and Crenshaw et al. (2010b). For Mrk 78, only slits A and D intersect the nucleus and are included in the figure, with slits B and C showing some points that partially match the more blueshifted cone model line. The galaxies Mrk 3 and NGC 1068 were observed with the low dispersion gratings and only required two kinematic components, with blue having the higher flux. Radial velocities are averaged within the photoionization model bins and matched to the nearest model line to obtain deprojection factors for the radial distances and velocities.

Table 3
Biconical Outflow Model Parameters

Name	PA	Incl.	HOA	r_{turn}	v_{max}	r_{max}	v_{deproj}	r_{deproj}	References
(1)	(deg)	(deg)	(deg)	(pc)	(km s^{-1})	(pc)	(near/far)	(near/far)	(10)
	(2)	(3)	(4)	(5)	(6)	(7)	(8)	(9)	(10)
Mrk 3	71	5 (NE)	20	55	1400	330	2.37/3.86	1.10/1.04	1, 2
Mrk 78	65	30 (SW)	10, 35	900	1200	3300	1.10/3.86	2.37/1.04	3
NGC 1068	30	5 (NE)	35	148	1300	435	1.56/2.00	1.30/1.16	4

Note. Columns are (1) target name, (2) PA of the bicone axis, (3) inclination angle of the bicone axis from the plane of the sky (direction closest to viewer), (4) model HOA, (5) turnover distance of maximum velocity, (6) maximum space velocity, (7) maximum outflow distance, (8) velocity and (9) distance deprojection factors, and (10) references for the original kinematic models: (1) Ruiz et al. (2001), (2) Crenshaw et al. (2010a), (3) Fischer et al. (2011), and (4) Das et al. (2005).

hollow bicone (Figure 7). In the case of Mrk 78, the STIS slit locations are close to the major axis of the galaxy disk ($\text{PA} = 84^\circ$), and the disk-flow model would result in observed radial velocities close to zero, in disagreement with the observations. Thus, we adopt our original biconical outflow models for this analysis.

For Mrk 3 and NGC 1068, we further simplify the models by choosing a single HOA between the minimum and maximum values that best fits the observed velocities weighted by the high-flux component, as shown by the black straight lines in Figure 7. The galaxy Mrk 78 has a significantly higher inclination, and separate HOAs for the near and far sides of each cone provide a better fit. Knowing the input model values, we determine deprojection factors for the near and far sides of each bicone.

The outflow models are shown in Figure 7, and the geometric parameters are provided in Table 3. Using these fits, we determine the deprojection factors for both velocity and distance from the center, average the radial velocities in each photoionization model bin (typically $0''.2$ – $0''.3$ in width), and choose the nearest velocity law. This is straightforward for Mrk 3 and NGC 1068 because the redshifted and blueshifted points are well separated due to their low inclinations. For Mrk 78, the sides of each cone are difficult to separate, and we choose the low-amplitude velocity law for radii $r > 2''$, the high-amplitude law for $r < 2''$, and a mean r_{deproj} of 1.68.

3.4. Emission Line Ratios

We use the Gaussian fit parameters to calculate integrated emission line fluxes and their ratios relative to $\text{H}\beta$ $\lambda 4861$. We sum the fluxes of the kinematic components at each radius for Mrk 78 because the biconical models are consistent with all of the gas outflowing in the STIS data, and the spectra generally display a low S/N. The four HST/STIS slits covering Mrk 78 show similar line ratios, and we calculate a single set of flux-weighted average line ratios to simplify the photoionization modeling process. This prevents us from detecting differences in the physical conditions of the kinematic components but is unavoidable given the low S/N of the spectra.

We calculate the flux-weighted average line ratios by deriving the observed emission line ratios for each of the four HST slits and correcting them for reddening using the procedure described in Section 3.3 of Revalski et al. (2018a). We then deproject the distances along the slits to radial distances from the nucleus using the Pythagorean theorem,

$$D = \sqrt{(\delta N \times S)^2 + (\delta R)^2}, \quad (1)$$

where δN is the distance in pixels from the pixel closest to the nuclear continuum peak, S is the HST/STIS plate scale of

$0''.05078 \text{ pixel}^{-1}$, and δR is the offset distance of each slit from the nucleus provided in Table 2. We then bin all of the measurements in $0''.2$ radial intervals together and calculate a single set of flux-weighted average line ratios and uncertainties for each radial distance.

These emission line ratios are given in Table 4, and the observed and reddening-corrected line ratios for the individual slits are available in the machine-readable format of Table 4. Unlike our previous targets, Mrk 78 displays a radial trend in the $[\text{O III}]/\text{H}\beta$ ratios, decreasing by a factor of 3 from ~ 18 to ~ 6 in the HST/STIS observations. This indicates a change in the ionization state of the optical emission line gas across the spatial extent of the outflow.

In the nuclear region, emission lines with a range of ionization potentials (IPs) are detected, from neutral $[\text{O I}]$ to $[\text{Ne V}]$. The number of detected lines and their fluxes decrease with increasing distance from the nucleus, which typically makes accurate modeling more difficult. This is alleviated by using a flux-weighted average of the four HST/STIS slits that intersect different emission line knots of various brightnesses. Despite the increased coverage afforded by four slits, the NLR emission is intrinsically weaker toward the northeast, resulting in larger uncertainties. The emission line ratios for Mrk 3 are given in Tables 2 and 3 of Collins et al. (2005), while for NGC 1068, they are provided in Tables 1 and 2 of Kraemer & Crenshaw (2000b). The measurements for these targets cover a similar swath of wavelengths, as well as emission lines in the UV portion of the spectrum.

3.5. Emission Line Diagnostics

We used the line ratios in Table 4 to create diagnostic diagrams that constrain the ionization, abundances, temperature, and density of the outflowing gas at each spatial location. In Figure 8, we present BPT diagrams that differentiate sources of ionization by comparing lines with different IPs and whose ratios vary significantly based on the spectral energy distribution (SED) of the ionizing source (Baldwin et al. 1981; Veilleux & Osterbrock 1987). At all spatial locations, the results are consistent with AGN ionization, indicating that the AGN's influence extends to radial distances of at least ~ 12 kpc, in agreement with Kozlova et al. (2020). The agreement of the HST and APO observations indicates that AGN ionization dominates on small and large scales without localized contributions to the ionization from jets or shocks. Interestingly, the $[\text{O III}]/\text{H}\beta$ ratios are ~ 18 in the nucleus and steadily decrease to ~ 6 at $\pm 3''$.

Next, we calculate the oxygen abundance using Equation (2) from Storch-Bergmann et al. (1998) and a reference solar

Table 4
Mrk 78 HST/STIS Flux-weighted Average Emission Line Ratios

Position	[Ne v] λ 3426	[O II] λ 3727	[Ne III] λ 3869	H γ λ 4340	[O III] λ 4363	He II λ 4686	H β λ 4861	[O III] λ 5007	[O I] λ 6300	H α λ 6563	[N II] λ 6584	[S II] λ 6716	[S II] λ 6731	H β Flux
-2.00	2.48 \pm 2.46	2.71 \pm 1.94	1.05 \pm 0.76	— \pm —	— \pm —	— \pm —	1.00 \pm 0.42	12.04 \pm 5.74	— \pm —	2.90 \pm 2.52	1.79 \pm 1.60	— \pm —	2.61 \pm 2.61	0.47 \pm 0.20
-1.80	1.49 \pm 1.49	4.84 \pm 4.56	0.88 \pm 0.88	— \pm —	— \pm —	— \pm —	1.00 \pm 0.70	16.43 \pm 13.48	— \pm —	2.87 \pm 2.75	1.90 \pm 1.74	0.68 \pm 0.68	0.95 \pm 0.95	1.37 \pm 0.96
-1.60	— \pm —	3.46 \pm 2.73	1.31 \pm 1.31	0.50 \pm 0.50	— \pm —	0.31 \pm 0.31	1.00 \pm 0.54	12.30 \pm 7.32	0.51 \pm 0.51	2.90 \pm 2.19	2.03 \pm 1.55	0.81 \pm 0.80	0.74 \pm 0.70	2.81 \pm 1.53
-1.40	1.05 \pm 0.82	5.25 \pm 3.72	2.10 \pm 1.87	0.57 \pm 0.41	— \pm —	0.56 \pm 0.30	1.00 \pm 0.45	13.99 \pm 6.94	0.29 \pm 0.29	2.90 \pm 1.82	2.24 \pm 1.47	0.60 \pm 0.55	0.60 \pm 0.60	13.82 \pm 6.25
-1.20	0.61 \pm 0.52	2.80 \pm 0.78	0.99 \pm 0.33	0.39 \pm 0.25	— \pm —	0.33 \pm 0.14	1.00 \pm 0.19	11.36 \pm 2.50	0.15 \pm 0.15	2.90 \pm 0.90	1.93 \pm 0.59	0.55 \pm 0.26	0.55 \pm 0.26	10.30 \pm 2.00
-1.00	0.62 \pm 0.48	3.14 \pm 1.97	1.71 \pm 0.87	0.49 \pm 0.32	0.20 \pm 0.14	0.38 \pm 0.22	1.00 \pm 0.31	13.03 \pm 4.81	0.19 \pm 0.19	2.90 \pm 1.31	1.81 \pm 0.81	0.58 \pm 0.23	0.52 \pm 0.33	17.56 \pm 5.40
-0.80	0.75 \pm 0.38	3.30 \pm 1.31	1.36 \pm 0.77	0.45 \pm 0.22	0.18 \pm 0.06	0.31 \pm 0.07	1.00 \pm 0.27	13.01 \pm 4.38	0.16 \pm 0.16	2.90 \pm 1.06	2.02 \pm 0.73	0.54 \pm 0.26	0.54 \pm 0.26	16.09 \pm 4.28
-0.60	0.52 \pm 0.52	2.09 \pm 0.98	0.93 \pm 0.58	0.28 \pm 0.16	— \pm —	0.27 \pm 0.13	1.00 \pm 0.36	12.18 \pm 5.02	0.25 \pm 0.25	2.90 \pm 1.38	2.20 \pm 1.06	0.58 \pm 0.36	0.54 \pm 0.32	7.33 \pm 2.66
-0.40	1.48 \pm 1.48	2.64 \pm 1.01	1.25 \pm 0.74	1.09 \pm 0.76	— \pm —	— \pm —	1.00 \pm 0.29	13.30 \pm 4.24	0.40 \pm 0.40	2.90 \pm 1.20	2.17 \pm 0.90	0.33 \pm 0.25	0.47 \pm 0.33	10.93 \pm 3.12
-0.20	— \pm —	3.36 \pm 3.36	5.00 \pm 5.00	— \pm —	— \pm —	— \pm —	1.00 \pm 0.92	16.00 \pm 16.00	— \pm —	2.90 \pm 2.90	2.50 \pm 2.50	— \pm —	— \pm —	25.04 \pm 22.95
\pm 0.10	— \pm —	1.50 \pm 1.50	1.20 \pm 1.20	— \pm —	— \pm —	— \pm —	1.00 \pm 0.55	17.85 \pm 10.64	— \pm —	2.90 \pm 2.01	2.22 \pm 1.53	0.48 \pm 0.41	0.65 \pm 0.56	2.85 \pm 1.57
0.20	1.05 \pm 0.46	1.62 \pm 0.43	1.49 \pm 0.50	0.38 \pm 0.18	0.25 \pm 0.12	0.40 \pm 0.15	1.00 \pm 0.16	15.64 \pm 3.49	0.26 \pm 0.15	2.90 \pm 0.71	1.59 \pm 0.38	0.35 \pm 0.12	0.38 \pm 0.12	32.90 \pm 5.42
0.40	1.24 \pm 0.55	5.38 \pm 3.19	3.12 \pm 2.00	0.63 \pm 0.63	— \pm —	0.28 \pm 0.16	1.00 \pm 0.35	15.65 \pm 6.31	0.42 \pm 0.36	2.90 \pm 1.30	2.11 \pm 1.02	0.60 \pm 0.34	0.62 \pm 0.36	42.51 \pm 14.72
0.60	3.15 \pm 3.15	3.76 \pm 3.76	4.60 \pm 4.33	0.98 \pm 0.98	— \pm —	— \pm —	1.00 \pm 0.66	12.81 \pm 8.65	1.09 \pm 1.09	2.90 \pm 2.58	1.81 \pm 1.65	1.41 \pm 1.41	0.77 \pm 0.77	3.17 \pm 2.10
0.80	2.41 \pm 1.11	2.98 \pm 1.47	1.50 \pm 0.88	0.38 \pm 0.37	— \pm —	0.54 \pm 0.54	1.00 \pm 0.24	11.98 \pm 3.15	0.58 \pm 0.58	2.89 \pm 1.30	1.87 \pm 0.87	0.68 \pm 0.53	0.66 \pm 0.53	3.61 \pm 0.87
1.00	0.81 \pm 0.60	3.90 \pm 1.79	1.73 \pm 0.89	0.43 \pm 0.29	0.47 \pm 0.36	0.32 \pm 0.19	1.00 \pm 0.26	11.91 \pm 3.64	0.15 \pm 0.13	2.90 \pm 1.22	1.65 \pm 0.69	0.54 \pm 0.26	0.55 \pm 0.30	8.31 \pm 2.14
1.20	1.83 \pm 1.83	4.53 \pm 2.79	1.51 \pm 1.17	0.61 \pm 0.58	— \pm —	0.23 \pm 0.22	1.00 \pm 0.49	9.83 \pm 5.33	— \pm —	2.90 \pm 1.97	1.89 \pm 1.26	0.75 \pm 0.60	0.85 \pm 0.76	4.49 \pm 2.22
1.40	— \pm —	4.07 \pm 2.08	1.56 \pm 1.12	0.77 \pm 0.77	0.19 \pm 0.11	0.28 \pm 0.19	1.00 \pm 0.33	9.44 \pm 3.52	0.34 \pm 0.34	2.90 \pm 1.65	1.94 \pm 1.16	0.74 \pm 0.50	0.68 \pm 0.47	3.89 \pm 1.28
1.60	— \pm —	4.43 \pm 2.50	0.94 \pm 0.47	0.44 \pm 0.42	0.18 \pm 0.06	0.21 \pm 0.08	1.00 \pm 0.32	9.31 \pm 3.50	— \pm —	2.89 \pm 1.52	1.58 \pm 0.84	0.38 \pm 0.29	0.58 \pm 0.43	6.43 \pm 2.03
1.80	0.65 \pm 0.65	4.88 \pm 3.60	1.11 \pm 0.72	0.60 \pm 0.45	— \pm —	0.35 \pm 0.12	1.00 \pm 0.46	8.76 \pm 4.64	0.46 \pm 0.46	2.90 \pm 1.94	1.75 \pm 1.15	0.70 \pm 0.60	0.68 \pm 0.51	6.23 \pm 2.86
2.00	— \pm —	6.79 \pm 4.36	1.28 \pm 1.13	0.77 \pm 0.77	0.18 \pm 0.07	0.18 \pm 0.14	1.00 \pm 0.40	9.29 \pm 4.59	0.50 \pm 0.50	2.90 \pm 1.68	2.23 \pm 1.25	0.71 \pm 0.46	0.71 \pm 0.42	5.71 \pm 2.29
2.20	— \pm —	5.27 \pm 2.03	0.88 \pm 0.32	0.59 \pm 0.28	0.40 \pm 0.40	0.21 \pm 0.12	1.00 \pm 0.21	7.52 \pm 2.02	0.38 \pm 0.38	2.90 \pm 1.07	2.47 \pm 0.88	0.75 \pm 0.33	0.94 \pm 0.41	3.87 \pm 0.81
2.40	— \pm —	4.77 \pm 2.44	0.91 \pm 0.71	0.45 \pm 0.20	0.16 \pm 0.08	0.18 \pm 0.14	1.00 \pm 0.26	6.82 \pm 2.43	0.32 \pm 0.32	2.90 \pm 1.16	2.05 \pm 0.83	0.82 \pm 0.48	0.81 \pm 0.33	4.60 \pm 1.17
2.60	1.07 \pm 1.07	3.82 \pm 1.28	0.74 \pm 0.40	0.47 \pm 0.26	0.17 \pm 0.11	0.14 \pm 0.08	1.00 \pm 0.21	6.41 \pm 1.72	0.26 \pm 0.26	2.90 \pm 0.98	1.87 \pm 0.59	0.80 \pm 0.35	0.71 \pm 0.31	3.76 \pm 0.78
2.80	0.62 \pm 0.29	4.24 \pm 1.39	0.58 \pm 0.36	0.51 \pm 0.34	— \pm —	0.17 \pm 0.16	1.00 \pm 0.20	6.11 \pm 1.72	0.39 \pm 0.39	2.89 \pm 1.02	2.04 \pm 0.69	0.94 \pm 0.41	0.91 \pm 0.42	2.89 \pm 0.59
3.00	0.77 \pm 0.77	3.73 \pm 2.02	1.11 \pm 0.77	0.50 \pm 0.42	— \pm —	0.70 \pm 0.70	1.00 \pm 0.34	7.20 \pm 2.93	0.52 \pm 0.52	2.90 \pm 1.57	2.45 \pm 1.27	0.95 \pm 0.56	0.84 \pm 0.47	1.06 \pm 0.36

Note. The flux-weighted average emission line ratios for slits A–D after correcting for reddening using a galactic extinction curve (Savage & Mathis 1979) and fixing the intrinsic H α /H β ratio to 2.90. The first column provides the deprojected distance from the nucleus in arcseconds, with positive toward the SW. The emission lines were fit using widths and centroids calculated from free fits to H α λ 6563, and the listed wavelengths are approximate vacuum values. Measurements for the weak [Ne III] λ 3969, [S II] λ 4074, and H δ λ 4102 lines, as well as the [O III] λ 4959, [O I] λ 6363, and [N II] λ 6548 lines that have relative strengths fixed to their brighter doublet counterparts (see Section 3.1), have been omitted for space and are available in the machine-readable version. The machine-readable version also contains the observations (A) and extinction-corrected values (B) from the individual slits. The last column lists the extinction-corrected H β flux (erg s $^{-1}$ cm $^{-2}$), which is the flux-weighted average of all measurements within each 0''/2 bin, with errors propagated from the H β flux and reddening-correction uncertainties. We required each line to have a minimum S/N of two in order to be considered a positive detection. Specifically, the height of the Gaussian fit must be at least twice the standard deviation of the flux in the continuum regions used for the fit. The uncertainty in each measurement is then the fractional uncertainty in the line flux added in quadrature with that of H β . We then add these in quadrature with the uncertainty in the reddening correction based on the errors in the H α /H β ratios. In regions with low flux, this results in effective S/N ratios of less than two for the reddening-corrected measurements. Positions marked with “— \pm —” are nondetections and those with uncertainties equal to the ratios are upper limits.

(This table is available in its entirety in machine-readable form.)

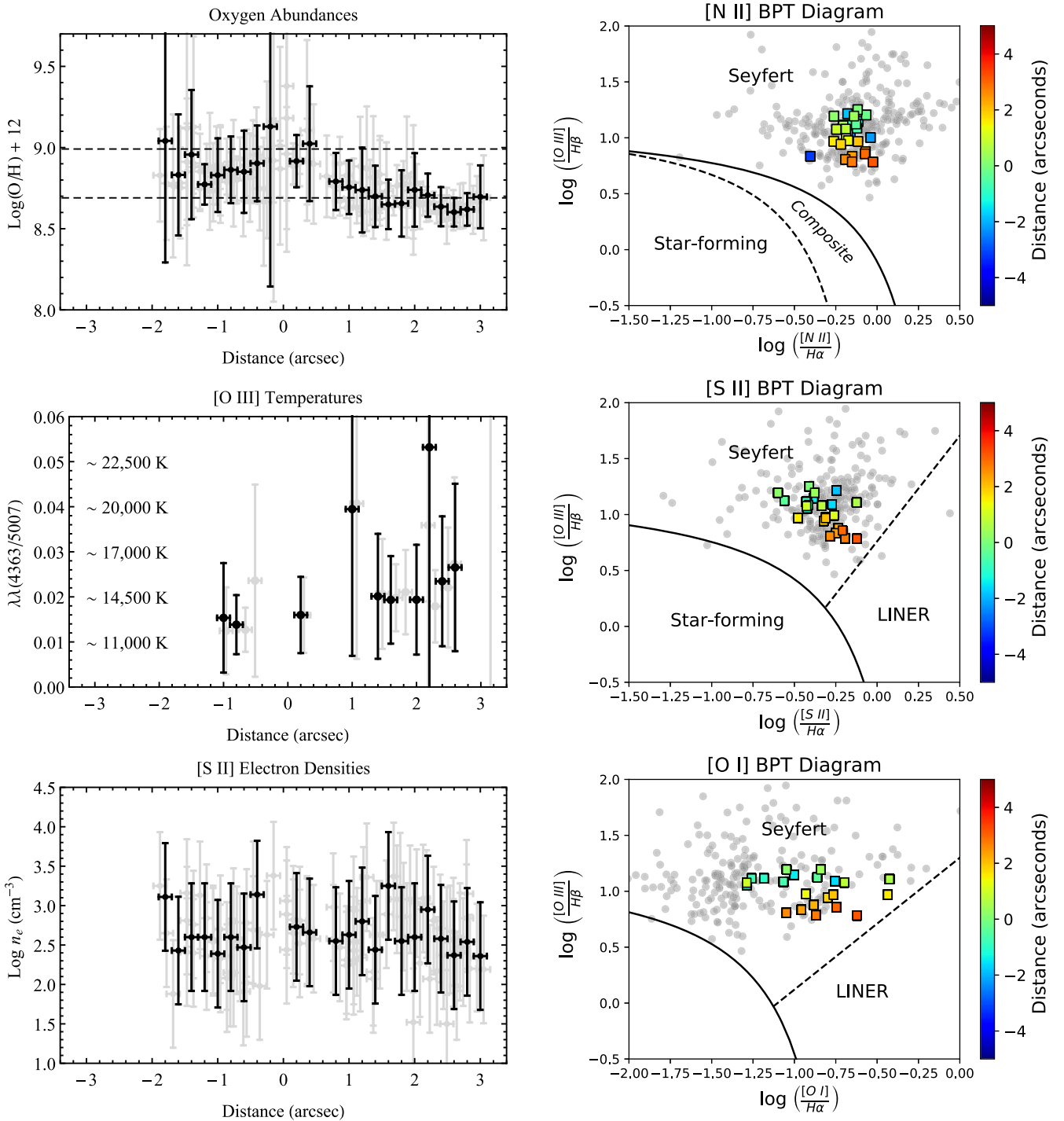


Figure 8. The Mrk 78 emission line diagnostic diagrams based on the line ratios in Table 4. The left column displays the oxygen abundances (top), temperatures (middle), and densities (bottom) derived from the HST/STIS spectroscopy. The flux-weighted mean of all four slits at each deprojected distance is shown in black, and the dispersion of the individual slits at their observed positions along the slits are shown in light gray. The lower and upper dashed lines in the abundance panel represent one and two times solar abundances, respectively. The right column displays the [N II] (top), [S II] (middle), and [O I] (bottom) BPT diagrams for the flux-weighted HST/STIS measurements (Table 4; colored squares) and the APO observations for all four PAs (gray circles). The grouping of APO points in the left portion of the [O I] diagram corresponds primarily to measurements along the NLR minor axis. The demarcation lines for distinguishing ionization mechanisms are from Kewley et al. (2001, 2006) and Kauffmann et al. (2003). The left-to-right orientation matches that in Figure 1 and all kinematic figures, with NE to the left (negative) and SW to the right (positive).

value (Z_{\odot}) of $\log(\text{O}/\text{H})+12 = 8.69$ (Asplund et al. 2009). As shown in the top left panel of Figure 8, the abundance of oxygen is $\sim 2 Z_{\odot}$ in the nuclear regions and steadily decreases to solar values toward the west, while remaining approximately constant at $\sim 1.4 Z_{\odot}$ in the east. These radial abundance

variations are in agreement with the study by Rosario (2007), and the adopted average is in general agreement with Dors et al. (2020).

The gas temperature is calculated self-consistently in photoionization models; thus, observational constraints are

useful for checking the validity of our modeling results. We use the [O III] emission lines to derive the gas temperatures shown in the middle left panel of Figure 8 and find typical NLR values of $\sim 10,000\text{--}15,000\text{ K}$ (Osterbrock & Ferland 2006). The average gas temperature is higher toward the west; however, the weak [O III] $\lambda 4363$ emission line introduces large uncertainties.

Finally, the goal of our modeling process is to accurately determine the gas density and thus mass, so we derive the electron density profile from the [S II] $\lambda\lambda 6716/6731$ line ratio. This doublet traces the low-ionization gas and is useful for that component of our photoionization models, with the [O III]–emitting gas typically less dense. The [S II] densities are shown in the bottom left panel of Figure 8 and are approximately constant, except for a small decrease at the furthest west extent. The large uncertainties are driven by the S/N of the doublet in the spectra, compounded by variations in the ratio between slits that are averaged over when combining into a flux-weighted average. This is encapsulated by the dispersion of the gray points in Figure 8, which show the densities for the individual HST slits.

3.6. [O III] Image Analysis

Our photoionization modeling process accounts for the emission and gas mass within the HST/STIS slits, and we use [O III] emission line images of the NLRs to calculate the total ionized gas mass as a function of distance from the nucleus for each AGN. As shown in Figure 9, we determine the [O III] radial flux profiles for each image by extracting fluxes within Elliptical Panda regions generated in the SAOImage DS9 software suite (Joye & Mandel 2003). We divide the elliptical annuli in half along the minor axis to account for asymmetries in the flux, density, and velocity profiles in each cone of the biconical outflows. The ellipses are centered on the continuum peak and radially spaced in increments matching the spatial sampling of our line ratios and photoionization models (typically $\sim 0''.2\text{--}0''.3$). The major axis lengths (a) of the ellipses are equal to the radial extent of our line ratio measurements along each slit, and the minor axis lengths (b) are calculated from the major axis length and NLR inclination (i) via the equation $b/a = \cos(i)$. The [O III] images, elliptical annuli, and extracted [O III] radial flux profiles are presented in Figure 9. We calculate the flux errors by measuring the standard deviation (σ) of the background in the line-free regions of each image. The uncertainty for each annular measurement is then equal to $\sqrt{N_{\text{pix}}} \times \sigma$, where N_{pix} is the number of pixels in the annulus. The background variations (σ , $\text{erg s}^{-1} \text{cm}^{-2} \text{pixel}^{-1}$) for each object are Mrk 78 = 1.9×10^{-18} , Mrk 3 = 9.9×10^{-18} , and NGC 1068 = 7.9×10^{-18} , resulting in typical uncertainties of $<1\%$ for the integrated [O III] flux measurements.

4. Photoionization Models

Our analysis is based on accurately converting the [O III] image fluxes to ionized gas masses at each radius. This requires accounting for local variations in the ionization state of the gas, as well as its abundances, temperature, and density. Accounting for these physical conditions is critical, because they set the gas emissivity, which directly determines the conversion between [O III] luminosity and the ionized gas mass. We use our previous photoionization model results for

Mrk 3 (Collins et al. 2009) and NGC 1068 (Kraemer & Crenshaw 2000b) and present here our new models for Mrk 78.

4.1. Input Parameters

We generate photoionization models using the Cloudy spectral synthesis code (version 13.04; Ferland et al. 2013). A self-consistent model requires supplying the number and energy distribution of the photons ionizing a gas cloud of specified composition and geometry. These conditions are encapsulated by the ionization parameter (U), which is the dimensionless ratio of the number of ionizing photons to atoms at the face of the gas cloud (Osterbrock & Ferland 2006, Section 13.6).¹¹ This is defined as

$$U = \frac{Q(H)}{4\pi r^2 n_H c}, \quad (2)$$

where r is the distance from the AGN, n_H is the hydrogen number density (cm^{-3}), c is the speed of light, and $Q(H)$ is the number of ionizing photons per second, given by $Q(H) = \int_{\nu_0}^{\infty} (L_\nu/h\nu) d\nu$, where L_ν is the luminosity of the AGN as a function of frequency (the SED), h is Planck's constant, and $\nu_0 = 13.6\text{ eV}/h$ is the IP of hydrogen (Osterbrock & Ferland 2006, Section 14.3). We use a common power-law SED from our previous studies (Kraemer & Crenshaw 2000a, 2000b) with $L_\nu \propto \nu^\alpha$. We adopt slopes of $\alpha = -0.5$ from 1 to 13.6 eV, $\alpha = -1.4$ from 13.6 eV to 0.5 keV, $\alpha = -1$ from 0.5 to 10 keV, and $\alpha = -0.5$ from 10 to 100 keV, with cutoffs below 1 eV and above 100 keV.

We determine the bolometric luminosity of the AGN by summing the observed [O III] fluxes in our APO long-slit observations and applying the correction factor from Heckman et al. (2004), namely, $L_{\text{bol}} = 3500 \times L_{[\text{O III}]}$, yielding $L_{\text{bol}} = 7.9 \times 10^{45} \text{ erg s}^{-1}$ ($\log L_{\text{bol}} \approx 45.9$). This estimate is in excellent agreement with the values found by Whittle et al. (1988) and González Delgado et al. (2001) when rescaled to our adopted distance. We then numerically compute the above integral, normalized to the bolometric luminosity, and find $Q(H) = 3.8 \times 10^{54} \text{ photons s}^{-1}$ ($\log Q(H) \approx 54.58$), in general agreement with Wilson et al. (1988), Whittle & Wilson (2004), and Rosario (2007).

The gas composition is set by the elemental abundances, dust content, and depletion fractions of elements onto dust grains. We found that the abundances vary with radial distance from the nucleus (Figure 8) but are consistent with an average value of $\sim 1.3 Z_\odot$ within the uncertainties across the NLR, and we adopt this average value for our models. The exact logarithmic values relative to hydrogen by number for dust-free models are He = -0.96 , C = -3.46 , N = -3.94 , O = -3.20 , Ne = -3.96 , Na = -5.65 , Mg = -4.29 , Al = -5.44 , Si = -4.38 , P = -6.48 , S = -4.77 , Ar = -5.49 , Ca = -5.55 , Fe = -4.39 , and Ni = -5.67 . The strong low-ionization lines are better reproduced when including a dusty component, and for models with a dust level of 50% relative to the interstellar medium, we accounted for depletion of elements in graphite and silicate grains (Seab & Shull 1983; Snow & Witt 1996; Collins et al. 2009). The logarithmic abundances relative to

¹¹ In some X-ray models, the ionization parameter is defined as $\xi = L_i/n_H r^2$, where L_i is the radiation energy density from 1 to 1000 Ry (13.6 eV–13.6 keV). A conversion for Seyfert power-law SEDs is $\log(U) \approx \log(\xi) - 1.5$ (Crenshaw & Kraemer 2012).

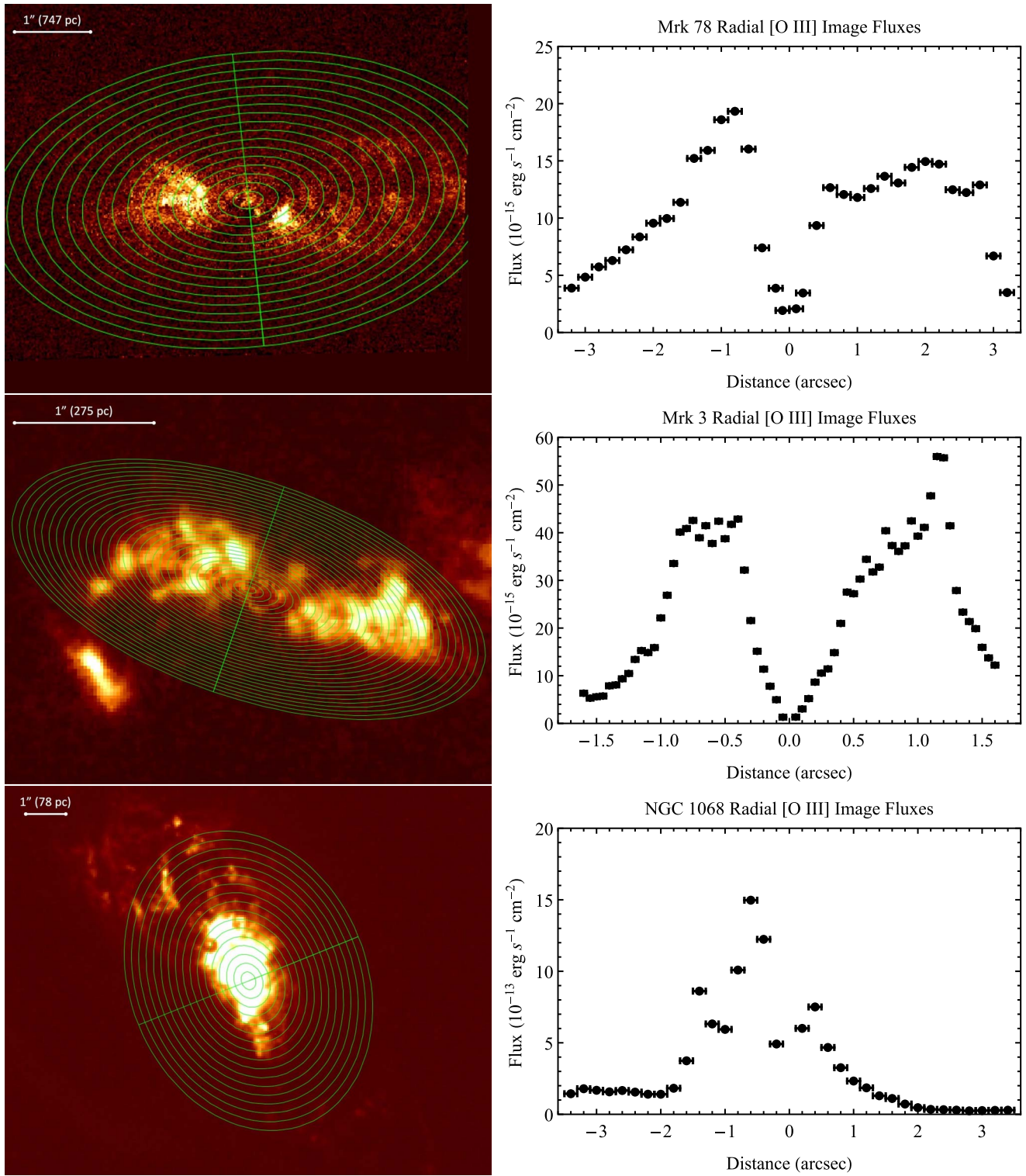


Figure 9. The [O III] images (left) and extracted radial flux profiles (right) for Mrk 78 (top), Mrk 3 (middle), and NGC 1068 (bottom). The annuli widths are $0''.2$ for Mrk 78, $0''.05$ for Mrk 3, which were summed to match the variable $0''.2$ – $0''.3$ extractions modeled in Collins et al. (2009), and $0''.2$ for NGC 1068, which were summed to match the $0''.4$ extractions modeled in Kraemer & Crenshaw (2000b). The extended emission for Mrk 78 falls off the edge of the detector, resulting in a minor underestimation of the flux and mass at $r > 2''.80$. The annular extractions extend to larger radii than the photoionization models, and the flux profile for NGC 1068 is vertically scaled 2 dex lower than the other targets because it is significantly brighter.

hydrogen by number for the dusty models are He = -0.96 , C = -3.63 , N = -3.94 , O = -3.32 , Ne = -3.96 , Na = -5.65 , Mg = -4.57 , Al = -5.70 , Si = -4.66 , P = -6.48 , S = -4.77 , Ar = -5.49 , Ca = -5.81 , Fe = -4.67 , and Ni = -5.93 .

4.2. Model Selection

We account for ionization stratification within the gas at each location by using up to three model components with different densities. These are denoted according to the value of their

ionization parameter (U) as HIGH, MED, and LOW ION. At each radius, the only unknown quantities in Equation (2) are U and n_{H} , so we choose a range of U values to produce the observed emission and solve for the corresponding density to maintain physical consistency. We then generate a grid of models and add fractional combinations of the HIGH, MED, and LOW components to create a composite model that matches the emission line ratios and is normalized to the $\text{H}\beta$ luminosity at each location along the slit.

We determine the best-fitting model for each radius using a simple optimization scheme that compares all fractional permutations of the HIGH, MED, and LOW model components in 5% intervals across our range of ionization parameters. The best-fitting model may be composed of one, two, or three components, and the simplest model matching all of the emission line criteria is selected. The criteria for a satisfactory fit vary by emission line, with sensitive diagnostic lines that constrain the gas density and mass having the strictest limits.

We initially require the predicted model line ratios to match the data (Table 4) within the following tolerances. The $\text{He II } \lambda 4686$ ratio that is sensitive to the column density and the $[\text{O III}] \lambda 5007$ ratio that determines our flux-to-mass scaling must match within 20%, which is smaller than the measurement uncertainties at each location along the slit (Table 4). The $[\text{O III}] \lambda 4363$, $[\text{O I}] \lambda 6300$, $[\text{N II}] \lambda 6584$, and $[\text{S II}] \lambda \lambda 6716, 6731$ ratios must match within a factor of 2. The remaining emission lines must match the observations to within a factor of 4. We successfully created models satisfying all of these starting criteria for 14/26 spatial positions. When these criteria resulted in multiple solutions, we incrementally tightened the criteria for the key diagnostic lines until a single best match was found. Similarly, when the initial criteria resulted in no solutions, we incrementally relaxed the criteria for all lines until a match was found. In cases with similar competing models, we selected the composite model that best matched the $\text{He II } \lambda 4686$ and $[\text{O III}] \lambda 5007$ lines, which are most sensitive to the gas column density and flux-to-mass scale factor, making them critical for determining accurate gas masses. The input and output parameters for our best-fitting Cloudy models are provided in Table 5.

4.3. Comparison to the Observations

A comparison of the model and data line ratios for the most important lines is shown in Figure 10, with the results for all lines and positions provided in the Appendix. Several factors contribute to the observed deviations, such as a poor Gaussian fit, the S/N of the measurements, the quality of atomic data for each element, and the accuracy of our multi-component models.

There is a mild underprediction for the overall strength of the $[\text{S II}] \lambda \lambda 6716, 6731$ lines at most locations, which may indicate the presence of more dust, that some of the $[\text{S II}]$ emission arises from the edges of the ionized NLR bicone, or that the low-ionization gas is exposed to a partially absorbed SED from a closer-in absorber (e.g., Maksym et al. 2016, 2017; Mingozi et al. 2019), as we found for Mrk 573 (Revalski et al. 2018a) and Mrk 3 (Collins et al. 2009). There is also a small but systematic offset between the observed and predicted $[\text{S II}]$ doublet ratios ($\sim 11\%$), indicating that the low-ionization model densities are slightly overpredicted. The model values are within the measurement uncertainties but could result in a minor underprediction of the mass in the low-ionization component of the gas.

The general underprediction of $[\text{O III}] \lambda 4363$ is a minor concern, as it indicates an underprediction of the temperature in more highly ionized zones; however, the most discrepant points have the largest uncertainties (see Figure 8) and may be partially attributed to blending with $\text{H}\gamma$. The $[\text{Ne V}]$ and $[\text{O II}]$ lines are generally underpredicted, which may indicate an overzealous reddening correction due to using a Galactic extinction curve, in agreement with the slight underprediction of $\text{H}\gamma$ at some positions. These lines were allowed less-stringent limits to properly match the key diagnostic lines that constrain the gas number and column densities that are used to calculate the gas masses.

Generating successful models for Mrk 78 is more difficult than for the majority of the targets in our sample because we are using a flux-weighted average of all measurements at each radial distance within four slits. These multiple extractions encompass emission with a larger range of physical conditions than are observed in a single slit. In general, there are insufficient high-ionization lines to tightly constrain the HIGH model component. While adding a third model component can improve the fit, it must be physically consistent with detected and nondetected emission lines. The locations with the strongest $[\text{Ne V}]$ detections, such as $-2''0$, $-0''4$, $+0''6$, and $+0''8$, all have contributions from a HIGH model component. Similarly, regions with weak or no detections of $[\text{Ne V}]$ (e.g., $-1''0$, $-1''6$) have either no HIGH component or they have a smaller contribution to the luminosity. The S/N was insufficient to measure emission line ratios at $-3''0$, $-2''8$, $-2''6$, $-2''4$, and $-2''2$, and for these positions, we adopt the physically consistent models from their positive counterparts. Overall, our models are able to successfully match all of the key diagnostic emission lines to within a factor of 2 or better at most locations across the NLR.

Finally, to confirm that our models are physically plausible, we also derive the surface areas ($A = L_{\text{H}\beta}/F_{\text{H}\beta}$) and thicknesses ($N_{\text{H}}/n_{\text{H}}$) of the emitting clouds, which must fit within the four HST spectral slits. This criterion is satisfied for all but two positions, which are at large radii and attributed to the significant line ratio uncertainties at those locations. We also calculate the depths of the clouds into the plane of the sky by dividing the cloud area by the projected slit width (~ 150 pc for Mrk 78) to verify that they are less than or equal to the line-of-sight distance across the bicone at each location. It is important to note that each ionized component may not be collocated within the slit, as the emission is spread across $0''2$ in the spatial and dispersion directions. These physical quantities are presented in Table 5.

5. Calculations

5.1. Mass of the Ionized Gas

We use the parameters from our photoionization models and the $\text{H}\beta$ luminosities to calculate the gas mass as a function of radius for the emission encompassed by the HST/STIS slits. The mass at each location is given by

$$M_{\text{slit}} = N_{\text{H}} \mu m_p \left(\frac{L_{\text{H}\beta}}{F_{\text{H}\beta_m}} \right) \quad (3)$$

(Crenshaw et al. 2015). In Equation (3), N_{H} is the model hydrogen column density, μ is the mean mass per proton (~ 1.4 for our abundances), m_p is the proton mass, $F_{\text{H}\beta_m}$ is the $\text{H}\beta$

Table 5
Cloudy Model Parameters for Mrk 78

Distance from Nucleus (arcsec) (1)	Comp ION Name (2)	Ionization Parameter $\log(U)$ (unitless) (3)	Column Density $\log(N_{\text{H}})$ (cm^{-2}) (4)	Number Density $\log(n_{\text{H}})$ (cm^{-3}) (5)	Dust Content Relative to ISM (6)	Fraction of Total Model (7)	$\log(F_{\text{H}\beta})$ Model Flux ($\text{erg s}^{-1} \text{cm}^{-2}$) (8)	Cloud Surface Area (10^3pc^2) (9)	Cloud Model Thickness (pc) (10)	Cloud Model Depth (pc) (11)
-2.00	HIGH	-1.20	21.40	0.89	0.0	0.15	-2.76	4.0	104.9	26.8
-2.00	MED	-1.80	21.40	1.49	0.5	0.50	-2.37	5.4	26.3	36.1
-2.00	LOW	-3.60	19.80	3.29	0.5	0.35	-2.21	2.7	<0.1	17.8
-1.80	HIGH	0.00
-1.80	MED	-1.80	21.40	1.58	0.5	0.85	-2.28	16.4	21.4	109.7
-1.80	LOW	-3.20	20.20	2.98	0.5	0.15	-2.12	2.0	0.1	13.5
-1.60	HIGH	0.00
-1.60	MED	-1.80	21.20	1.68	0.5	0.65	-2.19	14.0	10.7	94.0
-1.60	LOW	-3.80	19.80	3.68	0.5	0.35	-2.02	5.1	<0.1	34.0
-1.40	HIGH	0.00
-1.40	MED	-1.80	20.80	1.80	0.5	0.50	-2.39	56.3	3.2	376.6
-1.40	LOW	-3.20	20.20	3.20	0.5	0.50	-1.90	18.1	<0.1	121.0
-1.20	HIGH	-1.40	21.20	1.53	0.0	0.10	-2.28	8.3	15.2	55.4
-1.20	MED	-2.80	20.20	2.93	0.5	0.85	-1.80	23.5	0.1	157.3
-1.20	LOW	-3.00	20.40	3.13	0.5	0.05	-1.77	1.3	0.1	8.7
-1.00	HIGH	-1.80	20.60	2.09	0.0	0.10	-2.27	10.8	1.0	72.3
-1.00	MED	-1.80	21.60	2.09	0.5	0.40	-1.75	13.2	10.5	88.5
-1.00	LOW	-3.00	20.00	3.29	0.5	0.50	-1.64	12.6	<0.1	84.1
-0.80	HIGH	-1.20	21.40	1.68	0.0	0.05	-1.97	4.5	17.0	29.9
-0.80	MED	-1.80	21.60	2.28	0.5	0.40	-1.56	14.1	6.8	94.3
-0.80	LOW	-3.00	20.00	3.48	0.5	0.55	-1.45	14.7	<0.1	98.6
-0.60	HIGH	-1.40	21.80	2.13	0.0	0.15	-1.15	1.2	15.2	7.7
-0.60	MED	-1.80	21.60	2.53	0.5	0.30	-1.32	3.4	3.8	22.7
-0.60	LOW	-3.00	20.60	3.73	0.5	0.55	-1.16	4.3	<0.1	29.0
-0.40	HIGH	-1.20	21.40	2.28	0.0	0.20	-1.37	5.1	4.3	34.2
-0.40	MED	-2.60	21.00	3.68	0.5	0.70	-0.83	5.1	0.1	34.1
-0.40	LOW	-3.00	20.20	4.08	0.5	0.10	-0.83	0.7	<0.1	4.9
-0.20	HIGH	0.00
-0.20	MED	-2.40	21.00	4.09	0.5	1.00	-0.24	6.5	<0.1	43.8
-0.20	LOW	0.00
± 0.10	HIGH	0.00
± 0.10	MED	-1.80	21.80	4.09	0.5	0.95	0.25	0.5	0.2	3.0
± 0.10	LOW	-3.60	19.40	5.89	0.5	0.05	0.33	<0.1	0.0	0.1
0.20	HIGH	-1.40	20.60	3.09	0.0	0.10	-1.35	5.5	0.1	37.1
0.20	MED	-2.00	21.60	3.69	0.5	0.85	-0.30	4.1	0.3	27.6
0.20	LOW	-3.20	19.60	4.89	0.5	0.05	-0.41	0.3	<0.1	2.1
0.40	HIGH	0.00
0.40	MED	-1.80	21.40	2.88	0.5	0.45	-0.98	10.8	1.1	72.5
0.40	LOW	-3.00	20.20	4.08	0.5	0.55	-0.83	9.4	<0.1	63.2
0.60	HIGH	-1.00	21.20	1.73	0.0	0.10	-2.21	5.1	9.6	34.0
0.60	MED	-1.80	21.60	2.53	0.5	0.55	-1.32	3.6	3.8	24.0
0.60	LOW	-3.40	20.20	4.13	0.5	0.35	-1.16	1.6	<0.1	10.6
0.80	HIGH	-1.40	21.00	1.88	0.0	0.25	-2.15	7.7	4.3	51.4
0.80	MED	-1.80	21.60	2.28	0.5	0.50	-1.56	4.0	6.8	26.4
0.80	LOW	-3.20	20.40	3.68	0.5	0.25	-1.41	1.4	<0.1	9.2
1.00	HIGH	-1.20	21.40	1.49	0.0	0.05	-2.16	3.0	26.3	19.9
1.00	MED	-1.80	21.40	2.09	0.5	0.65	-1.77	15.7	6.6	104.9
1.00	LOW	-3.80	19.20	4.09	0.5	0.30	-1.67	5.8	<0.1	38.6
1.20	HIGH	0.00
1.20	MED	-1.20	21.80	1.33	0.0	0.50	-1.80	7.0	95.6	46.6
1.20	LOW	-3.40	20.20	3.53	0.5	0.50	-1.76	6.4	<0.1	42.7
1.40	HIGH	-1.40	21.40	1.40	0.0	0.10	-2.14	2.0	32.4	13.5
1.40	MED	-1.80	21.20	1.80	0.5	0.40	-2.07	6.8	8.1	45.6
1.40	LOW	-3.60	19.80	3.60	0.5	0.50	-1.90	5.8	<0.1	38.8
1.60	HIGH	-1.80	21.20	1.68	0.0	0.15	-2.03	4.4	10.7	29.2
1.60	MED	-1.80	21.40	1.68	0.5	0.35	-2.18	14.4	17.0	96.3
1.60	LOW	-3.80	19.20	3.68	0.5	0.50	-2.08	16.3	<0.1	109.0
1.80	HIGH	-0.80	21.80	0.58	0.0	0.10	-2.77	12.3	537.8	82.2
1.80	MED	-2.00	21.40	1.78	0.5	0.15	-2.21	5.1	13.5	33.9
1.80	LOW	-3.00	20.40	2.78	0.5	0.75	-2.12	20.4	0.1	136.8

Table 5
(Continued)

Distance from Nucleus (arcsec)	Comp ION Name	Ionization Parameter $\log(U)$ (unitless)	Column Density $\log(N_{\text{H}})$ (cm^{-2})	Number Density $\log(n_{\text{H}})$ (cm^{-3})	Dust Content Relative to ISM	Fraction of Total Model	$\log(F_{\text{H}\beta})$ Model Flux ($\text{erg s}^{-1} \text{cm}^{-2}$)	Cloud Surface Area (10^3pc^2)	Cloud Model Thickness (pc)	Cloud Model Depth (pc)
(1)	(2)	(3)	(4)	(5)	(6)	(7)	(8)	(9)	(10)	(11)
2.00	HIGH	-1.60	21.40	1.29	0.0	0.45	-2.22	15.8	41.7	105.5
2.00	MED	-3.00	20.00	2.69	0.5	0.05	-2.23	1.8	0.1	12.2
2.00	LOW	-3.80	19.20	3.49	0.5	0.50	-2.26	19.6	<0.1	130.9
2.20	HIGH	0.00
2.20	MED	-1.80	21.20	1.40	0.5	0.50	-2.47	24.2	20.4	162.1
2.20	LOW	-3.60	19.40	3.20	0.5	0.50	-2.34	18.0	<0.1	120.4
2.40	HIGH	-1.40	21.60	0.93	0.0	0.15	-2.38	7.1	151.6	47.4
2.40	MED	-1.80	21.60	1.33	0.5	0.25	-2.51	16.0	60.3	107.2
2.40	LOW	-4.00	18.80	3.53	0.5	0.60	-2.56	42.7	<0.1	285.4
2.60	HIGH	-1.20	21.80	0.66	0.0	0.35	-2.46	19.0	447.4	127.2
2.60	MED	-1.80	21.60	1.26	0.5	0.10	-2.58	7.2	70.9	48.0
2.60	LOW	-4.00	18.80	3.46	0.5	0.55	-2.63	43.7	<0.1	292.2
2.80	HIGH	-1.40	21.60	0.79	0.0	0.35	-2.52	16.7	209.2	111.7
2.80	MED	-3.60	19.80	2.99	0.5	0.15	-2.51	7.0	<0.1	46.9
2.80	LOW	-4.00	19.00	3.39	0.5	0.50	-2.58	27.6	<0.1	184.5
3.00	HIGH	-1.60	20.80	0.93	0.0	0.20	-3.26	28.9	24.0	193.2
3.00	MED	-2.60	18.60	1.93	0.5	0.40	-4.36	730.6	<0.1	4887.7
3.00	LOW	-3.80	19.60	3.13	0.5	0.40	-2.58	12.0	<0.1	80.2

Note. Best-fit Cloudy model input (columns (1)–(6)) and output (columns (7)–(11)) parameters. The columns are (1) position with positive values toward the SW, (2) component name, (3) log ionization parameter, (4) log column density, (5) log number density, (6) dust fraction relative to the ISM, (7) fraction of model contributing to the $\text{H}\beta$ luminosity, (8) log $\text{H}\beta$ model flux ($\text{erg s}^{-1} \text{cm}^{-2}$), (9) surface area of the gas divided by 10^3 , (10) gas cloud thickness ($N_{\text{H}}/n_{\text{H}}$), and (11) depth into the plane of the sky.

model flux, and $L_{\text{H}\beta}$ is the luminosity of $\text{H}\beta$ calculated from the extinction-corrected flux and distance. We calculate the masses for each of our HIGH, MED, and LOW ionization components separately by dividing up the $\text{H}\beta$ luminosity by the model fractional contributions and then summing the mass in each component. Conceptually, this process finds the area of the emitting clouds through the ratio of the luminosities and model fluxes, multiplies this area by the column density (projected particles per unit area) to yield the total number of particles, which is multiplied by the mean mass per particle to give the total ionized mass. The results of Equation (3) describe the number of $\text{H}\beta$ photons per unit mass that can be scaled to [O III] based on the [O III]/ $\text{H}\beta$ ratios. With the mass per unit [O III] flux at each location, we determine the total ionized gas mass outside of the slit by multiplying the mass in the slit by the flux ratio $F_{\text{image}}/F_{\text{slit}}$. This formalism eliminates the scale factor used in our previous investigations and simplifies the calculations. For Mrk 78, we retain the scale factor because the flux-weighted average line ratio luminosities do not allow for a direct comparison between the slit and annuli fluxes. The errors in the masses are dominated by the uncertainties in the $\text{H}\beta$ luminosities, which are determined from the emission line fit residuals and the reddening uncertainty. In addition, there is an uncertainty of ± 0.05 dex ($\sim 12\%$) in the model column densities, and thus the final masses, due to the Cloudy model grid step sizes.

5.2. Outflow Parameters

Our goal is to determine the impact of the outflows on their host galaxies. The energy carried in the outflows can be

quantified using six primary metrics: mass, kinetic energy, momentum, and their respective outflow rates. The mass outflow rate (\dot{M}_{out}) at each distance is

$$\dot{M}_{\text{out}} = \left(\frac{M_{\text{out}} v}{\delta r} \right), \quad (4)$$

where M_{out} is the outflowing mass in each annulus (which can be less than the total mass when a portion of the gas is in rotation, as we found for Mrk 34 in Revalski et al. 2018b), v is the deprojected velocity corrected for inclination and PA on the sky (Section 3.2 of Revalski et al. 2018a), and δr is the deprojected width of each annulus. The kinetic energy (E), kinetic energy flow rate (\dot{E}), momentum (p), and momentum flow rate (\dot{p}) at each radius are given by

$$E = \frac{1}{2} M_{\text{out}} v^2, \quad (5)$$

$$\dot{E} = \frac{1}{2} \dot{M}_{\text{out}} v^2, \quad (6)$$

$$p = M_{\text{out}} v, \quad (7)$$

$$\dot{p} = \dot{M}_{\text{out}} v. \quad (8)$$

We do not include contributions to the energetics from velocity dispersion, such as turbulence, which would add a σ_v term to the expressions. We obtain a single radial profile for each of these quantities by azimuthally summing the values derived for each of the semi-annuli.

6. Results

We present the spatially resolved gas-mass profiles and mass outflow rates for each AGN in Figure 11, as well as the kinetic

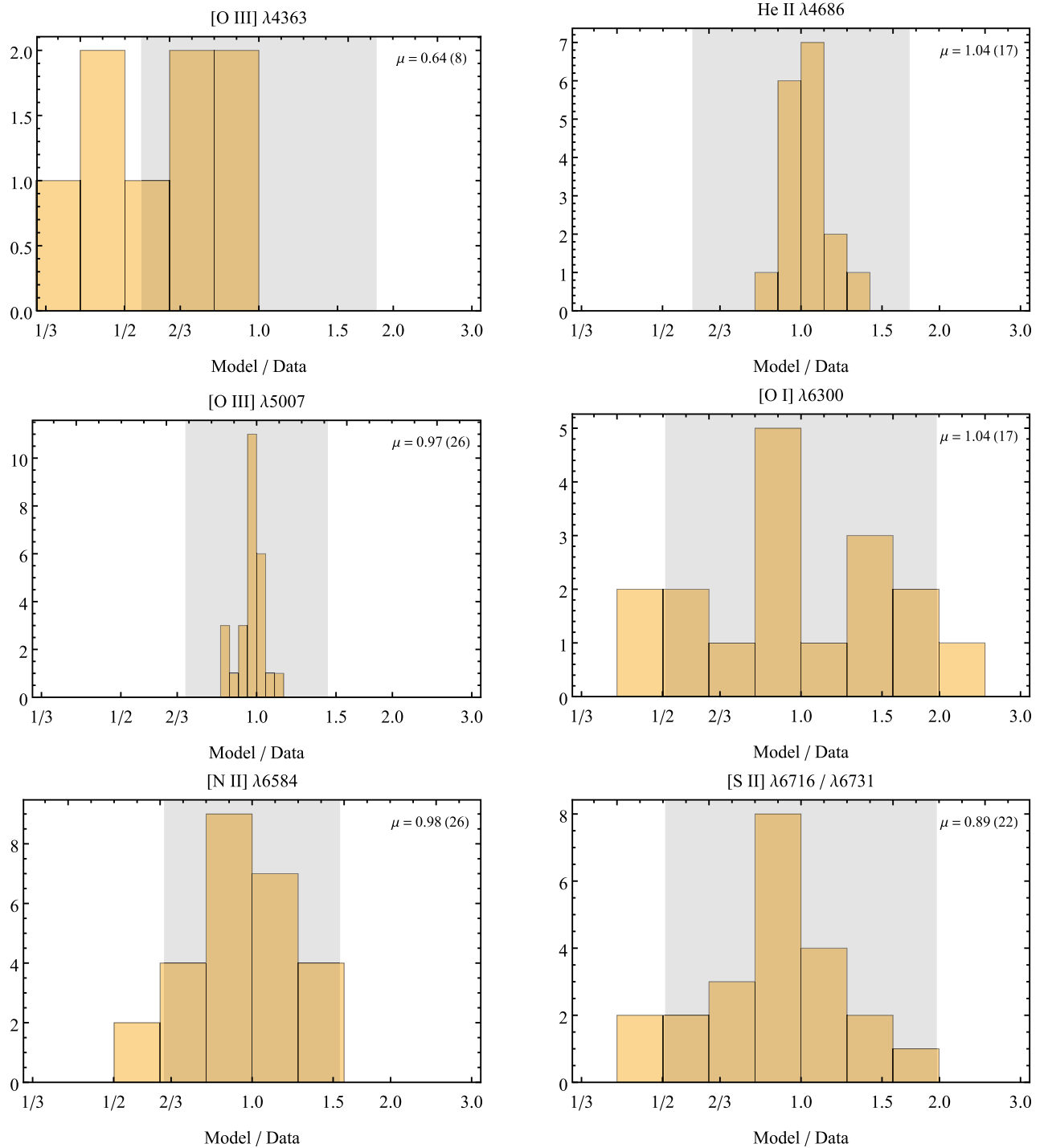


Figure 10. Histograms of the Mrk 78 model line ratios divided by the dereddened values (Table 4) for the select emission lines that are most important for constraining the gas masses. These are [O III] $\lambda 4363$ (temperature), He II $\lambda 4686$ (column density), [O III] $\lambda 5007$ (flux-to-mass), [O I] $\lambda 6300$ (column density and SED), [N II] $\lambda 6584$ (abundances), and [S II] $\lambda 6716/\lambda 6731$ (density). A value of unity indicates an exact match between the model and data, while the shaded regions are the mean uncertainties for each emission line over all positions. The mean of each distribution (μ) is shown in the upper right corner, along with the number of measurements in parentheses. The horizontal tick marks are logarithmically spaced for even distribution around unity. Points above unity are overpredicted, while points below unity are underpredicted by the models. Figures comparing the data and models for all emission lines at all positions are available in the Appendix. In general, all models match the data within the uncertainties, except for several underpredictions of [O III] $\lambda 4363$, indicating a mild underprediction of the gas temperature at some locations. The dispersion in [O I] $\lambda 6300$ may be due to its combined sensitivity to the SED, gas turbulence, temperature, and column density.

energies, momenta, and their outflow rates in Figures 12 and 13. In general, the rates rise from zero at the nucleus, where the outflow velocities are zero, to maximum values at hundreds of parsecs from the nuclei in the lower-luminosity targets. The higher-luminosity AGN, Mrk 34 and Mrk 78, reach their

peak mass outflow rates at ~ 0.5 and ~ 1.2 kpc, respectively, and display the largest peak mass outflow rates of $\dot{M}_{\text{out}} \approx 10 M_{\odot} \text{ yr}^{-1}$. The ionized outflows extend to radial distances of $r \approx 0.1\text{--}3$ kpc from the nucleus, with signatures of disturbed and/or rotational kinematics at larger radii.

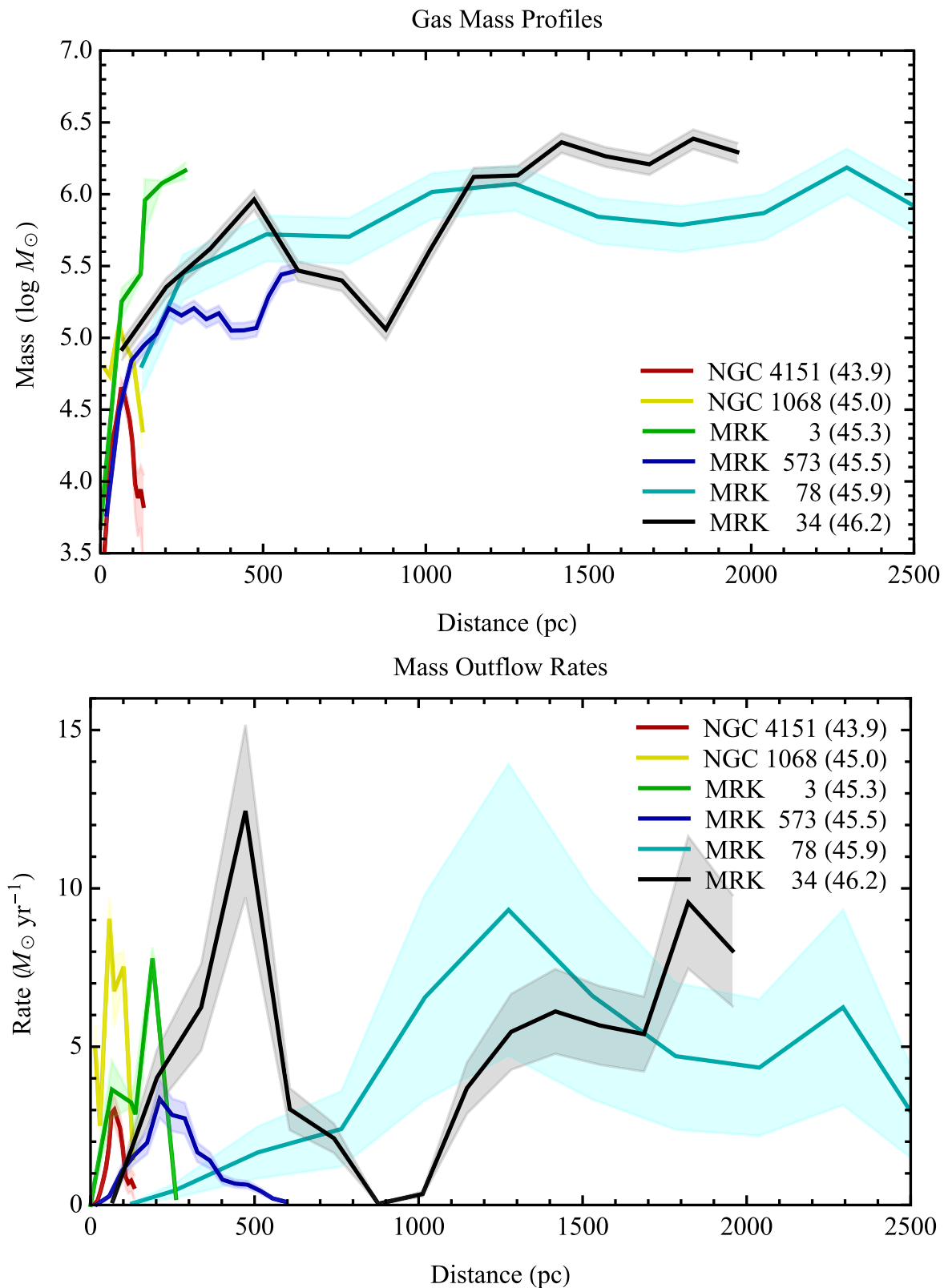


Figure 11. Spatially resolved gas-mass profiles (top) and mass outflow rates (bottom) for NGC 4151 (Crenshaw et al. 2015), NGC 1068 (this work), Mrk 3 (this work), Mrk 573 (Revalski et al. 2018a), Mrk 78 (this work), and Mrk 34 (Revalski et al. 2018b). The logarithmic bolometric luminosity for each AGN is provided in parentheses. The masses and outflow rates are the quantity in each radial bin, not enclosed totals, and each target has a different bin size. The uncertainties are propagated from the errors in the reddening-corrected $H\beta$ luminosities and the resolution of the parameters in the photoionization model grids. The integrated masses and peak rates are compared in Figure 14, and the results are available in tabular form in the Appendix.

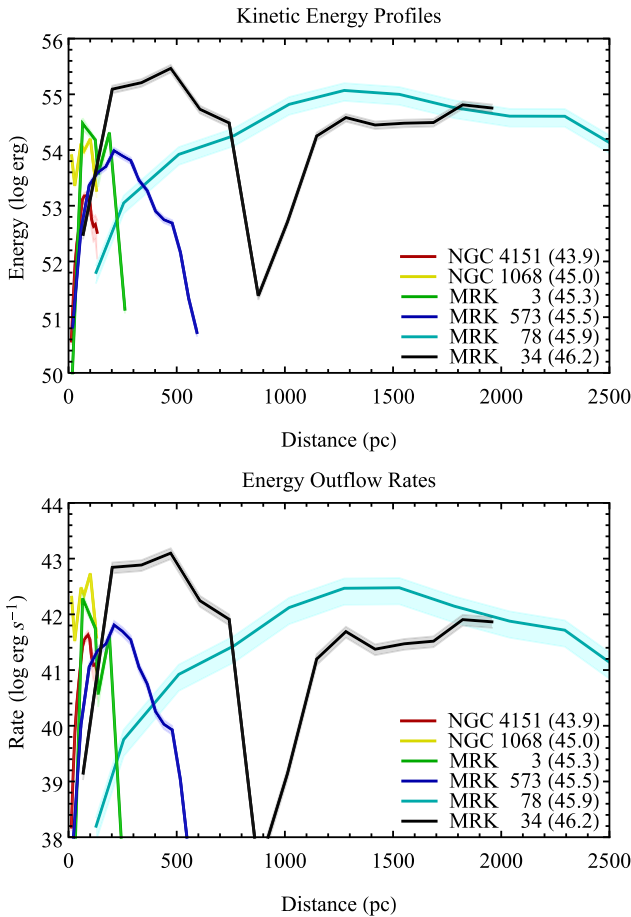


Figure 12. Same as Figure 11 for the spatially resolved kinetic energy and kinetic energy outflow rates.

6.1. Correlations with Luminosity

Overall, several trends are visible in the shapes of the profiles and magnitudes of the rates. The masses of the ionized outflows and their radial extents from the nuclei increase almost monotonically with AGN luminosity. The kinetic energies, momenta, and their outflow rates also scale with bolometric luminosity; however, the relative difference between each AGN varies depending on the adopted metric. To explore these correlations, we present the integrated gas masses, kinetic energies, and momenta, as well as their maximal outflow rates, in Figure 14 and Table 6. In general, the dispersions in these relationships are smallest for the integrated properties (left column of Figure 14), which are less sensitive to differences in the specific model parameters that are averaged over as compared to the peak quantities (right column of Figure 14). While the integrated quantities may provide a better measure of the total outflow impact, it is important to note that accurately determining these values required spatially resolved spectroscopy and photoionization models to account for variations in the gas density and outflow velocity at each location in the NLR.

The peak quantities also trend with increasing luminosity, with two notable outliers. The peak outflow rate for Mrk 573 is somewhat lower than that for targets of comparable luminosity. This may be due to true physical dispersion or a minor

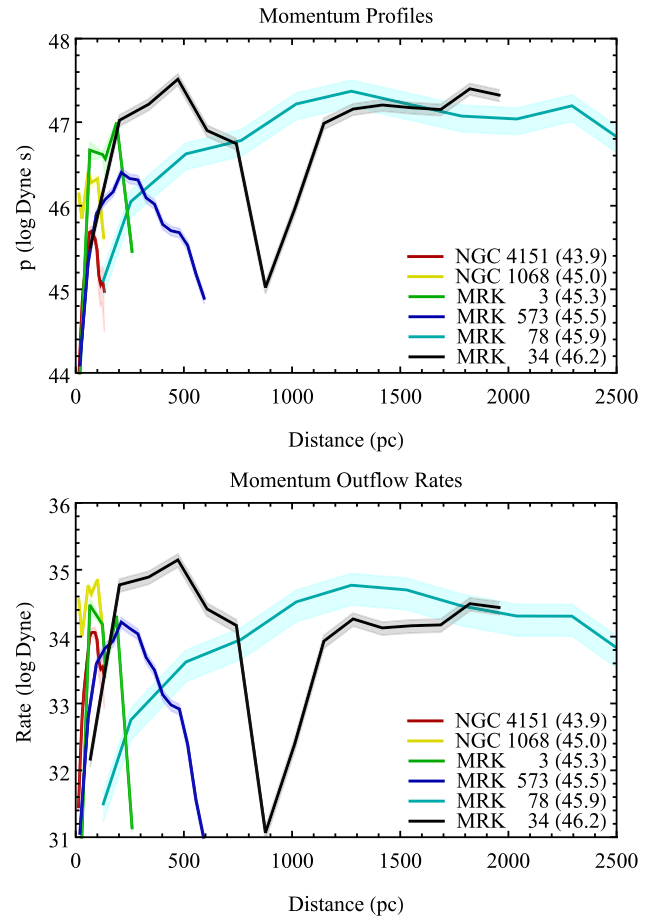


Figure 13. Same as Figure 11 for the spatially resolved momenta and momenta outflow rates.

underestimation in mass at the location of the peak outflow rate from using a single model component at large radial distances. This was required because there were insufficient emission lines to create multi-component photoionization models over the full spatial extent of the outflow in Mrk 573. Conversely, the peak energy and momentum outflow rates for NGC 1068 are higher than those for targets of comparable luminosity due to a combination of higher-than-average mass and outflow velocity at small radii.

In addition to the trends explored in Figure 14, it is well known that the extents of outflows and photoionized gas are correlated with AGN luminosity (e.g., Schmitt et al. 2003; Greene et al. 2011; Liu et al. 2013; Hainline et al. 2014; Bae et al. 2017; Fischer et al. 2018; Kang & Woo 2018; Storchi-Bergmann et al. 2018; Sun et al. 2018; Luo et al. 2020). However, we defer an analysis of the outflow radii, as these measurements are strongly affected by the depth and sensitivity of the observations, which, as discussed in Section 3.2, are not uniform for our sample.

These correlations are in good qualitative agreement with recent studies. Fiore et al. (2017) presented an extensive review of molecular, ionized, and X-ray outflow scaling relationships, primarily for AGN with $L_{\text{bol}} > 10^{44} \text{ erg s}^{-1}$. The relationship between mass outflow rate and L_{bol} is shallower than we find in Figure 14, which is in agreement with the conclusions of Shimizu et al. (2019) and Baron & Netzer (2019) that there is a

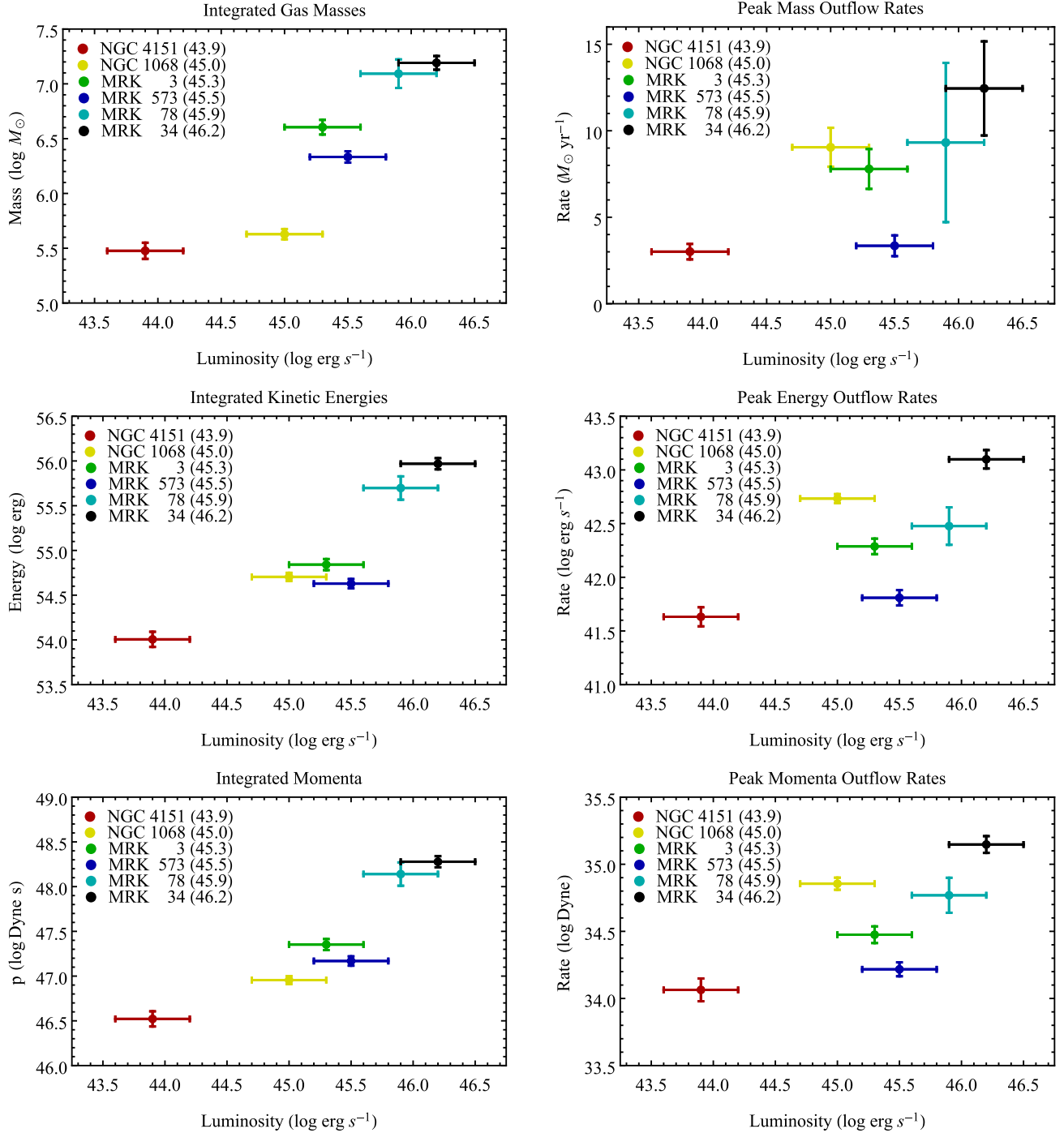


Figure 14. Total mass, kinetic energy, and momentum of the outflows (left column), as well as the maximum mass, kinetic energy, and momentum outflow rates (right column) for each AGN as a function of the bolometric luminosity, with exact values provided in parentheses. The uncertainties in luminosity are adopted from the typical ± 0.3 dex dispersion in the [O III]–to–bolometric luminosity scaling relationship, while the vertical errors are driven by the emission line fit residuals, reddening-correction uncertainty, and resolution of the parameters in the photoionization model grids (see text in Section 5.1). In general, all of the total and peak energetic quantities are positively correlated with increasing AGN luminosity (see text in Section 6.1).

steepening of these relationships at lower luminosities. Our results sit above the relationship in Figure 11 of Kakkad et al. (2020), but both results are consistent when we consider that we have a significant mass contribution from lower-density, higher-ionization gas that is not included in a single-density medium that primarily traces the [O III] emission line gas. We present further comparisons with recent studies in the discussion section.

6.2. Spatially Resolved Gas Properties

Our multi-component photoionization models allow us to explore the ionization stratification and range of densities in the outflows. The total ionized gas mass within the outflows ($r < 3''$) of Mrk 78 as derived from the [O III] imaging is $M_{\text{ion}} = 3.5 \times 10^7 M_{\odot}$. The four HST/STIS slits used to construct the models encompass $\sim 35\%$ of the [O III] image

Table 6
Integrated and Peak Outflow Properties

Catalog Name	$\log(L_{\text{bol}})$ (erg s^{-1})	Total M ($\log M_{\odot}$)	\dot{M}_{max} ($M_{\odot} \text{ yr}^{-1}$)	Total E ($\log \text{ erg}$)	\dot{E}_{max} ($\log \text{ erg s}^{-1}$)	Total p ($\log \text{ dyne s}$)	\dot{p}_{max} ($\log \text{ dyne}$)	$\dot{E}_{\text{max}}/L_{\text{bol}}$ (%)	$\dot{p}c/L_{\text{bol}}$ (%)
(1)	(2)	(3)	(4)	(5)	(6)	(7)	(8)	(9)	(10)
NGC 4151	43.9 ± 0.3	5.48 ± 0.07	3.01 ± 0.45	54.01 ± 0.08	41.63 ± 0.09	46.52 ± 0.08	34.06 ± 0.08	0.54 ± 0.11	437 ± 85
NGC 1068	45.0 ± 0.3	5.63 ± 0.05	9.04 ± 1.13	54.70 ± 0.05	42.73 ± 0.04	46.96 ± 0.05	34.86 ± 0.05	0.54 ± 0.05	214 ± 22
Mrk 3	45.3 ± 0.3	6.60 ± 0.07	7.79 ± 1.15	54.84 ± 0.06	42.29 ± 0.07	47.35 ± 0.06	34.47 ± 0.06	0.10 ± 0.02	44 ± 6
Mrk 573	45.5 ± 0.3	6.33 ± 0.05	3.35 ± 0.60	54.63 ± 0.05	41.81 ± 0.07	47.17 ± 0.05	34.22 ± 0.05	0.02 ± 0.01	15 ± 1
Mrk 78	45.9 ± 0.3	7.09 ± 0.13	9.32 ± 4.60	55.70 ± 0.13	42.48 ± 0.17	48.14 ± 0.13	34.77 ± 0.13	0.04 ± 0.02	22 ± 6
Mrk 34	46.2 ± 0.3	7.19 ± 0.06	12.45 ± 2.72	55.97 ± 0.06	43.10 ± 0.09	48.28 ± 0.06	35.15 ± 0.06	0.08 ± 0.02	26 ± 3

Note. The tabulated results from Figure 14. The columns are (1) target name, (2) bolometric luminosity, (3) total mass of the ionized gas, (4) peak mass outflow rate, (5) total kinetic energy, (6) peak kinetic energy outflow rate, (7) total momentum, (8) peak momentum outflow rate, (9) peak kinetic energy outflow rate divided by the bolometric luminosity (percentage), and (10) peak momentum outflow rate divided by the photon momentum (percentage).

flux, and thus mass, of the NLR. The mass is divided among the HIGH, MED, and LOW ION model components. Their contributions to the outflow gas mass (with model uncertainties) are

$$\text{HIGH} = 1.5(\pm 0.2) \times 10^7 M_{\odot} \rightarrow 42(\pm 6)\%$$

$$\text{MED} = 1.9(\pm 0.2) \times 10^7 M_{\odot} \rightarrow 56(\pm 5)\%$$

$$\text{LOW} = 7.0(\pm 0.7) \times 10^5 M_{\odot} \rightarrow 2(\pm 1)\%.$$

The densities of these components across all spatial locations vary by several orders of magnitude, from $\log(n_{\text{H}}) \approx 0.6$ to 6 cm^{-3} . The LOW ION component generally has the highest density and contributes $\sim 20\%$ – 50% of the $\text{H}\beta$ luminosity (Table 5) but contains only $\sim 2\%$ of the ionized gas mass. This is a stark demonstration of the selection effects present when calculating gas masses. The luminosity is weighted toward higher-density gas that emits efficiently because the free electrons can recombine quickly, but this component contains only a small fraction of the mass. The result is that even modest underestimates of the density for this luminous component significantly overestimate the gas mass.

The gas masses derived for Mrk 3 and Mrk 78 are consistent with the results of Collins et al. (2009) and Rosario (2007), respectively, with our estimates moderately larger due to the inclusion of emission outside of the HST/STIS slits. The rapid rise in the gas-mass profile for Mrk 3 may be due to a more compact reservoir that is externally fueled through its interaction with the nearby spiral galaxy UGC 3422 (Noordermeer et al. 2005; Collins et al. 2009; Gnilka et al. 2020). The galaxy NGC 1068 displayed an enhanced mass outflow rate of $\sim 17 M_{\odot} \text{ yr}^{-1}$ at $0''.8$ ($\sim 62 \text{ pc}$), which may be the result of a shock that results in additional radiation without additional mass, so we replaced it with the mean of itself and the adjacent two values.

The mass outflow rates for Mrk 78 are consistent with our previous studies, where gas is accelerated in situ at all radii. If the outflow were a steady nuclear flow, the peak outflow rate calculated from the mass in the central bin ($M_{\text{ion}} = 6.4 \times 10^4 M_{\odot}$) at the location of the peak velocity ($r = 1.2 \text{ kpc}$) would be $\sim 0.4 M_{\odot} \text{ yr}^{-1}$. This is ~ 24 times smaller than the observed peak outflow rate, indicating that material is entrained in the outflow and/or accelerated from reservoirs of gas at each radius. The outflow energetics are consistent with being radiatively driven for at least four of the AGN (Table 6), which have peak momentum outflow rates that are less than the

AGN photon momentum (L_{bol}/c). The energetics are also comparable to recent simulations of radiative driving (Mosallanezhad et al. 2019) but require additional mass modeling of the bulge and galaxy potentials for a proper comparison. Alternatives such as the disk-wind driving model of Menci et al. (2019) can also reproduce some of the observed correlations.

Finally, it is important to note that the masses, kinetic energies, and momenta can be summed over all radii to obtain enclosed totals; however, the outflow rates cannot. Integrating the outflow rates ($\dot{M} = Mv/\delta r$) over the radius (δr) simply returns the momentum ($p = Mv$), and calculating a “total” mass outflow rate is incorrect. As noted by Shimizu et al. (2019), this is because the rate needs to be calculated within a common radius. This differs from summing the rates azimuthally to obtain the radial profiles, as these measurements represent the mass flux through common boundaries.

7. Discussion

We discuss the assumptions of our analysis (Section 7.1), compare our results with recent outflow studies (Section 7.2), highlight connections with X-ray outflows (Section 7.3), and explore the implications of our results in the context of AGN feedback (Section 7.4).¹² The result-driven reader may choose to forgo Section 7.1 without a loss of continuity.

7.1. Assumptions

Our goal is to produce high-precision measurements of the radial gas-mass profiles, outflow rates, and energetics. We discuss here the assumptions underlying our techniques that were not explicitly addressed elsewhere and attempt to characterize their effects on our results.

Galaxy distances—Uncertainties in the adopted distance to each AGN have the potential to affect our results. We have calculated these distances using Hubble’s Law, which determines the distance to each galaxy based on its measured recessional velocity ($D = v/H_0$). This process assumes that a galaxy’s motion is dominated by Hubble flow due to the expansion of the universe. However, galaxies also have their own peculiar velocities that may be as large as $\sim 600 \text{ km s}^{-1}$.

¹² A portion of this discussion has been adapted from Revalski (2019), *Quantifying Feedback from Narrow Line Region Outflows in Nearby Active Galaxies*, Dissertation, Georgia State University, 2019; https://scholarworks.gsu.edu/phy_astr_diss/114.

This effect is negligible for galaxies at distances of >85 Mpc ($z > 0.02$), introducing an uncertainty of $<10\%$. The closest galaxy in our sample is NGC 4151, for which Crenshaw et al. (2015) adopted a distance of $D = 13.3$ Mpc. Subsequently, the distance to NGC 4151 has been independently measured to be 16.1 ± 0.5 Mpc using Cepheid variables (Yuan et al. 2020). Similarly, a Tully–Fisher estimate of the distance for NGC 1068 using a B -band calibration (Tully et al. 2008) and a k -corrected apparent magnitude of 9.23 ± 0.01 yields a distance of $D = 13.0 \pm 3.8$ Mpc, which agrees with the redshift estimate (Table 1) within the uncertainties (J. Robinson et al., private communication).

Changing the adopted distance for a galaxy corresponds to a shift in our adopted spatial scale, which would alter the outflow radii and bin sizes used to calculate the gas masses and outflow rates. If a new distance of D_1 is adopted, then, compared to the previous D_2 , the spatial scale would change by a factor of (D_1/D_2) . In addition, the luminosities used to calculate the gas-mass profiles would change by a factor of $(D_1/D_2)^2$. While the effects of distance uncertainties are small for our sample based on the accuracy of our adopted distances, the kinematic and modeling results can be scaled to calibrate the outflow results for different distance estimates.

Outflow geometries—Our results rely on adopting a geometric model of the host galaxy and outflow orientations to deproject the observed radial distances and line-of-sight velocities to their intrinsic values. In the cases of Mrk 573 and Mrk 34, the data support outflow along the galactic disk due to alignment between the ionizing bicone and the disk, based on the structure observed in HST imaging. Specifically, the [O III] emission corresponds to arcs of emission that can be traced to inner spiral dust lanes, as well as fueling flows of warm molecular gas in the case of Mrk 573 (Fischer et al. 2017), implying driving of the outflows off of spiral dust lanes within the host galaxy disk. The orientations of the disks were constrained with either kinematic models of the stellar velocity fields or isophotal ellipse fitting to continuum images (Fischer et al. 2017, 2018). In the cases of NGC 4151, NGC 1068, Mrk 3, and Mrk 78, the kinematics are well fit by biconical outflow models with material flowing along the axes of the bicone (Ruiz et al. 2001; Das et al. 2005; Crenshaw et al. 2010a; Fischer et al. 2011). These models are nevertheless consistent with in situ acceleration because the galactic disks have finite thicknesses that allow for ionization and acceleration of disk material by the ionizing bicone regardless of the orientation of the bicone with respect to the disk (Crenshaw et al. 2010b; Fischer et al. 2011). Interestingly, Takeo et al. (2020) suggested that the biconical morphology may play a key role in fueling AGN. If these systems were interpreted in the framework of the disk-flow model, then the deprojected outflow velocities would be higher, leading to larger outflow rates by up to factors of a few.

Azimuthal symmetry—The measured gas kinematics and quantities derived from our photoionization models are based on the emission that occupies the narrow HST/STIS long-slits. We then use HST [O III] images of the NLRs to calculate the total ionized gas mass and outflow rate at each radius. This process requires us to assume that the quantities derived within the long-slit are symmetric over all azimuthal angles at each distance, which may not be the case considering the biconical morphology of the NLR. Specifically, the outflow velocity,

density, and reddening laws that are derived within the spectral slits are assumed to hold elsewhere in the NLR.

As a first measure, we quantify the [O III] flux outside of the nominal bicone in each AGN by dividing the elliptical annuli into smaller azimuthal segments. We find that the large solid angles of weaker emission along the bicone minor axes correspond to a small fraction of the total [O III] luminosity. Specifically, for NGC 4151, Mrk 573, and Mrk 34, adopting bicone HOAs of $\theta = 33^\circ$, 38° , and 40° , respectively, results in only 31%, 19%, and 20% of the [O III] flux outside of the nominal bicones (Revalski 2019).

Supplementary studies of these AGN (Das et al. 2005; Storchi-Bergmann et al. 2010; Fischer et al. 2017) indicate that to first order, the outflow velocity is not a strong function of azimuthal angle within the ionizing bicones. In addition, while the derived density and reddening laws used to calculate the ionized gas masses are unlikely to hold precisely along the NLR minor axis, our APO/DIS observations indicate that this gas is AGN ionized; however, see the recent HST study by Ma et al. (2021). While the material may be susceptible to more foreground reddening, it would result in only a minor underestimation of the gas mass along the NLR minor axis, which already corresponds to $\lesssim 30\%$ of the total [O III] luminosity. We further reduced the impact of assuming azimuthal symmetry by dividing the elliptical annuli into two sections, modeling each half of the bicone independently. This refinement was important for Mrk 34 and Mrk 78, where the density and related physical conditions were bimodal across the NLR bicone.

Ionizing continuum—In our Cloudy photoionization models, we adopted a standard Seyfert power-law SED that has been derived primarily from studies of type 1 AGN (e.g., Schmitt et al. 1997; Alonso-Herrero et al. 2003; Jin et al. 2012). Due to the obscured nature of type 2 AGN, their ionizing source cannot be directly detected. We normalized the SEDs to calibrated measures, such as the 2–10 keV or [O III] luminosities. In the case of Mrk 34, the AGN is Compton thick, and even higher-energy X-rays were used to model the SED (Gandhi et al. 2014). These quantities are believed to be isotropic and thus are used to calculate the bolometric luminosities based on calibrations derived from type 1 AGN.

The scatters in these relationships are typically factors of ~ 3 – 4 and ultimately affect our estimate of the number of ionizing photons per second (Q_{ion}) emitted by the AGN that is used in our Cloudy models. The Q_{ion} and deprojected distances were used to constrain the gas densities as functions of the ionization parameter at each distance. Based on changes in the predicted emission line ratios over small ranges of ionization parameter and density, it is likely that changes in Q_{ion} by factors of ~ 2 – 4 would be indistinguishable within the uncertainties.

As each of the Cloudy model components may have a different ionization parameter and density, and thus a different mass, quantifying the resulting change in the total gas mass is not straightforward. However, larger changes in Q_{ion} that may occur if the AGN is changing in luminosity on timescales comparable to the light-crossing time of the NLR would be captured, as the best-fit models would be unable to reproduce the density-sensitive emission line ratios at the ionization parameters required to match their overall strengths relative to the $H\beta$ emission line. In the case of Mrk 78, the initial estimate of the bolometric luminosity from Woo & Urry (2002) was too

low by a factor of 40, resulting in low model densities that could not match all of the key diagnostic lines and overestimated the gas masses.

Extinction curves—We adopted a Milky Way Galactic extinction curve (Savage & Mathis 1979; Cardelli et al. 1989) to correct the observed emission line ratios that were used to model the ionized gas mass. This assumes that the standard Galactic reddening law applies within both our Galaxy and the AGN host galaxy. This is unlikely to be the case for all nearby AGN, and in the case of Mrk 3, Collins et al. (2005) found the attenuation to be consistent with an LMC-type extinction curve. It is difficult to distinguish between models without extensive UV spectroscopy, as the differences between various extinction curves are largest in the UV and have a smaller impact in the optical. For the majority of our galaxies, using a Milky Way Galactic extinction curve results in reddening-corrected emission line ratios that agree well with the model predictions, particularly for the H and He recombination lines that are robust and largely unaffected by the specific Cloudy model parameters.

7.2. Comparison with Recent Studies

We find peak mass outflow rates of $\dot{M}_{\text{out}} \approx 3\text{--}12 M_{\odot} \text{ yr}^{-1}$ that are correlated with AGN luminosity. These outflow rates are comparable to those found by several recent studies. At low redshifts, Storchi-Bergmann et al. (2010) and Barbosa et al. (2014) found global mass outflow rates of $\sim 2 M_{\odot} \text{ yr}^{-1}$ for NGC 4151 and NGC 1068, respectively, in agreement with our average values for these targets. Interestingly, our mass outflow rates are also comparable to those of local ultraluminous infrared galaxies that are fueled by major mergers, with Rose et al. (2018) reporting global mass outflow rates of $\dot{M}_{\text{out}} \approx 0.1\text{--}11 M_{\odot} \text{ yr}^{-1}$ for a sample of nine local ($z < 0.15$) galaxies. In a spatially resolved study of NGC 5728, Shimizu et al. (2019) found a peak outflow rate of $\sim 0.1 M_{\odot} \text{ yr}^{-1}$ at ~ 250 pc from the central AGN, with the outflows reaching radial extents of ~ 600 pc. This target has a comparable luminosity to NGC 4151 and displays strong signatures of inflow fueling the AGN.

At higher redshifts ($z \approx 0.6\text{--}2$), Förster Schreiber et al. (2019) found mass outflow rates of $\sim 0.2\text{--}20 M_{\odot} \text{ yr}^{-1}$, with AGN-driven outflows having significantly higher densities than those driven by star formation (see also Swinbank et al. 2019 and Fluetsch et al. 2020). Similarly, Leung et al. (2019) found a mean mass outflow rate of $\dot{M}_{\text{out}} \approx 13 M_{\odot} \text{ yr}^{-1}$ and comparable energy outflow rates to our AGN at even higher redshifts ($z \approx 1.4\text{--}3.8$), with a small number of targets displaying more energetic outflows. Finally, Kakkad et al. (2020) recently completed an investigation of AGN-driven outflows in a sample of more luminous AGN at $z \approx 2$ and, when combined with the results of other recent investigations, found a similar trend of increasing mass outflow rates across 5 orders of magnitude in luminosity.

The commonality in the majority of these studies is that they adopt gas densities of $n_{\text{H}} \sim 1000 \text{ cm}^{-3}$, which is significantly higher than the values of $\sim 100 \text{ cm}^{-3}$ used in earlier investigations. These higher densities correspond to lower mass and outflow rate measurements as $M_{\text{ion}} \propto L/n_{\text{H}}$. These higher densities are consistent with our MED and LOW ION model components that produce the majority of the observed luminosity and suggest that at least some previously reported outflow rates that adopt densities of $n_{\text{H}} \sim 100 \text{ cm}^{-3}$ are overestimated. This trend toward adopting higher densities

in mass outflow rate calculations is well supported by our results and recent studies. Previous estimates of the gas electron density have been obtained using the [S II] emission line doublet. As noted by Kraemer et al. (2000), Kakkad et al. (2018), Baron & Netzer (2019), Kewley et al. (2019), Revalski (2019), Shimizu et al. (2019), Davies et al. (2020), Comerón et al. (2021), and others, these lines only probe a single, low-ionization component of the outflows. The density derived from the doublet can be lower than the majority of the gas producing the observed luminosity, which significantly overestimates the mass of the ionized outflows. In a future study, we will present several methods for determining spatially resolved gas densities and compare the resulting gas masses with those derived from multi-component photoionization models.

7.3. Connecting Multiphase Outflows

Our results account for the optical and UV emission line gas; however, powerful outflows are also observed in the hot X-ray, neutral, and cold molecular gas phases (e.g., Perna et al. 2017; Bischetti et al. 2019; Fluetsch et al. 2019; Roberts-Borsani & Saintonge 2019; Catalán-Torrecilla et al. 2020; Lutz et al. 2020; Veilleux et al. 2020). Understanding the multiphase and multiscale properties of these outflows requires multiwavelength data sets at the highest possible spatial resolution (Gaspari et al. 2020). These data are being obtained with the current generation of observatories, including the Chandra X-ray Observatory and the Atacama Large Millimeter/submillimeter Array (ALMA), and will be enhanced with next-generation instruments on the James Webb Space Telescope. The connection to molecular outflows is discussed later, and in the X-rays, all of the targets in our sample have been observed by Chandra. Wang et al. (2011b, 2011a, 2011c) conducted a detailed analysis of the X-ray gas in NGC 4151 and found a global mass outflow rate of $\dot{M}_{\text{out}} \approx 2 M_{\odot} \text{ yr}^{-1}$. This was expanded to a spatially resolved analysis by Kraemer et al. (2020), which confirmed a peak outflow rate of $\dot{M}_{\text{out}} \approx 2 M_{\odot} \text{ yr}^{-1}$ at a distance of ~ 150 pc from the nucleus. In NGC 1068, Kraemer et al. (2015) found that the X-ray gas mass is an order of magnitude larger than the optical emission line gas, while in Mrk 3, Bogdán et al. (2017) found an X-ray gas mass of $M_{\text{ion}} \approx 1.1 \times 10^7 M_{\odot}$, which is comparable to the mass of the optical outflows that we and Collins et al. (2009) calculated. Chandra observations of Mrk 573 were modeled by Bianchi et al. (2010) and Gonzalez-Martin et al. (2010), with the former finding two photoionized components required to reproduce the observed emission and ionization parameters that are natural extensions of our optical model parameters. This supports the idea that the optical, UV, and soft X-ray emission arises from a single photoionized region (Bianchi et al. 2006), with localized contributions from shocks detected in the X-rays in similar AGN (e.g., Maksym et al. 2019). A similar multiwavelength study of NGC 1365 by Venturi et al. (2018) using MUSE and Chandra found comparable mass outflow rates for the optical and X-ray emission line gas, supporting the increased impact of multiphase outflows. These results indicate that outflows in the X-ray emission line gas may have a common origin with the optical outflows and can have comparable outflow energetics.

7.4. Implications for Feedback

A critical open question is: do outflows provide effective feedback to their host galaxies? The answer to this question depends on the criteria adopted for the definition of *effective*

feedback. The commonly used criteria are the theoretical thresholds for the peak kinetic luminosity (peak energy outflow rate), which needs to reach $\sim 0.5\%$ – 5% of the AGN bolometric luminosity to significantly impact the host galaxy (Di Matteo et al. 2005; Hopkins & Elvis 2010). Interestingly, the peak energy outflow rates of NGC 4151 and NGC 1068, our two lowest-luminosity targets, both exceed $\sim 0.5\%$ of their bolometric luminosities, while the higher-luminosity targets average $\sim 0.05\%$ (see Table 6). However, these criteria are primarily intended for high-redshift galaxies that are establishing their bulge structure through ongoing evolution with the central AGN radiating near the Eddington limit. In the local universe, AGN host galaxies have fully established bulges, and defining effective feedback in the context of evacuating reservoirs of potential star-forming gas and the disruption of star formation may be more relevant (e.g., Smith et al. 2020; García-Bernete et al. 2021).

The gas masses and outflow rates for our sample indicate that the ionized gas can be evacuated from the inner bulges on timescales of $\tau \approx M/\dot{M} \approx 10^6$ yr. Recent observations of Mrk 573 with ALMA reveal that the nuclear region ($r < 1.4$ kpc) contains $\sim 10^8 M_\odot$ of cold molecular gas (Wiklind et al., private communication), which is consistent with the cold-to-ionized gas ratio of similar AGN. If the ionized gas reservoir is continually replenished through the ionization of the cold molecular gas, as seen in NGC 4151 (May et al. 2020), then the evacuation timescale for the cold gas in the bulge of Mrk 573 is $\tau \approx M/\dot{M} \approx 10^8$ yr, which is comparable to the duty cycle of an AGN. However, if the molecular gas is also outflowing with comparable velocities, then the enhanced outflow rate would lead to more rapid depletion (see, e.g., Baron et al. 2020; Fluetsch et al. 2020; García-Bernete et al. 2021). Observations of the molecular gas with ALMA and bulge-mass decomposition modeling (Fischer et al. 2017) of each AGN are required to calculate more precise evacuation timescales and determine if the outflows reach escape velocities.

We also observe that AGN-ionized gas in the ENLR extends to kiloparsec scales and can encompass $> 10^8 M_\odot$ of gas. This may inhibit star formation by heating the gas in the galaxy disk and inducing turbulence that prevents collapse into star-forming regions, as evidenced by the high-FWHM lines that often extend beyond the outflow regions (Fischer et al. 2018). This heating- and turbulence-induced feedback mechanism has been suggested by several recent studies (e.g., Cheung et al. 2016; Morganti 2017; Chen et al. 2019; Lacerda et al. 2020; Wylezalek et al. 2020; Zhuang & Ho 2020; Zinger et al. 2020), and there is evidence that at least some nearby AGN sit below the Kennicutt–Schmidt law (Kennicutt 1998; Wang et al. 2007) that describes the star formation rate per unit area as a function of gas surface density. This is worthy of future investigation and will require determining the ENLR gas mass of each AGN from deep [O III] imaging, measuring their star formation rates, and comparing them with a matched sample of quiescent galaxies with similar host galaxy types, colors, and gas masses (e.g., Rosario et al. 2018, 2019).

8. Conclusions

We provide the largest sample to date of spatially resolved NLR mass outflow energetics that are based on multi-component photoionization models. These results provide important constraints for determining accurate gas masses

and outflow rates using spatially resolved spectroscopy. Our main conclusions are the following.

1. Spatially resolved observations are required to properly constrain the properties of ionized outflows. These include the outflow velocity profile, luminosity distribution, radial extent, and separation of kinematic components. Global techniques that utilize spatially integrated spectra and provide a single estimate of the outflow mass and energetics are susceptible to strong selection effects.
2. The adopted gas densities have a profound effect on the derived gas masses, and modeling the optical emission line gas is a multiphase problem that requires multiple density components. When using a single density, estimates from the [S II] doublet or assuming a constant density of $n_H = 100 \text{ cm}^{-3}$ can overestimate the gas mass for NLR outflows by more than an order of magnitude in some instances.
3. The outflows are photoionized by the central AGN and likely driven by radiation pressure, as evidenced by the correlation of mass outflow properties with bolometric luminosity. Shocks are not required for ionizing or driving the optical emission line gas, with a localized contribution from shocks detected in only one object, NGC 1068.
4. The outflows contain total ionized gas masses of $M \approx 10^{5.5} - 10^{7.5} M_\odot$ and reach peak velocities of $v \approx 800 - 2000 \text{ km s}^{-1}$. They extend to radial distances of $r \approx 0.1 - 3$ kpc from the nucleus, reaching maximum mass outflow rates of $\dot{M}_{\text{out}} \approx 3 - 12 M_\odot \text{ yr}^{-1}$ and encompassing total kinetic energies of $E \approx 10^{54} - 10^{56}$ erg.
5. The ionized gas masses, outflow rates, energetics, and radial extents of the outflows are all positively correlated with the AGN bolometric luminosity. The dispersion in these trends is smaller for the integrated quantities as compared to the peak rates.
6. The outflow rates are consistent with in situ acceleration, where gas is accelerated at multiple radii by the radiation field, rather than a steady nuclear flow. The mass, kinetic energy, and momentum profiles may be summed radially to obtain the enclosed totals; however, the radial rates cannot, because they must be sampled within a common radius.

As interest in spatially resolved outflow studies grows, it has become clear that the choice of gas densities plays a critical role in calculating accurate outflow gas masses. In a forthcoming paper, we will present the results of several density estimate techniques and compare the spatially resolved gas masses and outflow rates to those obtained using multi-component photoionization models.

In addition, we will expand our sample to properly quantify the slopes and dispersions in the luminosity scaling relations through an approved Cycle 28 HST program (HST PID 16246, PI: M. Revalski) that is obtaining [O III] and continuum images of additional Seyfert galaxies with archival HST/STIS spectroscopy. When combined with archival targets, our expanded sample of 22 AGN will span ~ 4 dex in bolometric luminosity.

M.R. thanks Jenny Novacescu and the STScI library staff for ADS reference support and Justin H. Robinson for helpful discussions. The authors thank the anonymous referee for helpful comments that improved the clarity of this paper.

This work was supported by the STScI Directors Discretionary Research Fund (DDRF) Proposal 82490. W.P.M. acknowledges

support by Chandra grants GO8-19096X, GO5-16101X, GO7-18112X, and GO8-19099X. Support for this work was provided by NASA through grant No. HST-GO-15350.001-A from the Space Telescope Science Institute, which is operated by AURA, Inc., under NASA contract NAS 5-26555.

This paper used the photoionization code Cloudy, which can be obtained from <http://www.nublado.org>, and the Atomic Line List, available at <http://www.pa.uky.edu/~peter/atomic/>. This research has made use of NASA’s Astrophysics Data System. This research has made use of the NASA/IPAC Extragalactic Database (NED), which is operated by the Jet Propulsion Laboratory, California Institute of Technology, under contract with the National Aeronautics and Space Administration. IRAF is distributed by the National Optical Astronomy Observatories, which are operated by the Association of Universities for

Research in Astronomy, Inc., under cooperative agreement with the National Science Foundation.

Facilities: HST(STIS, WFPC2, FOC), ARC(DIS).

Software: IRAF (Tody 1986, 1993), MultiNest (Feroz et al. 2019), Cloudy (Ferland et al. 2013), Mathematica (<https://www.wolfram.com/mathematica>), Python (Van Rossum & Drake 2009, <https://www.python.org>), IDL (<https://www.harrisgeospatial.com/Software-Technology/IDL>).

Appendix Photoionization Modeling Results for Mrk 78

In this Appendix, we provide the complete results for Figures 10–13 in tabular form, as well as a comparison of the model and dereddened line ratios for all spatial positions listed in Table 4.

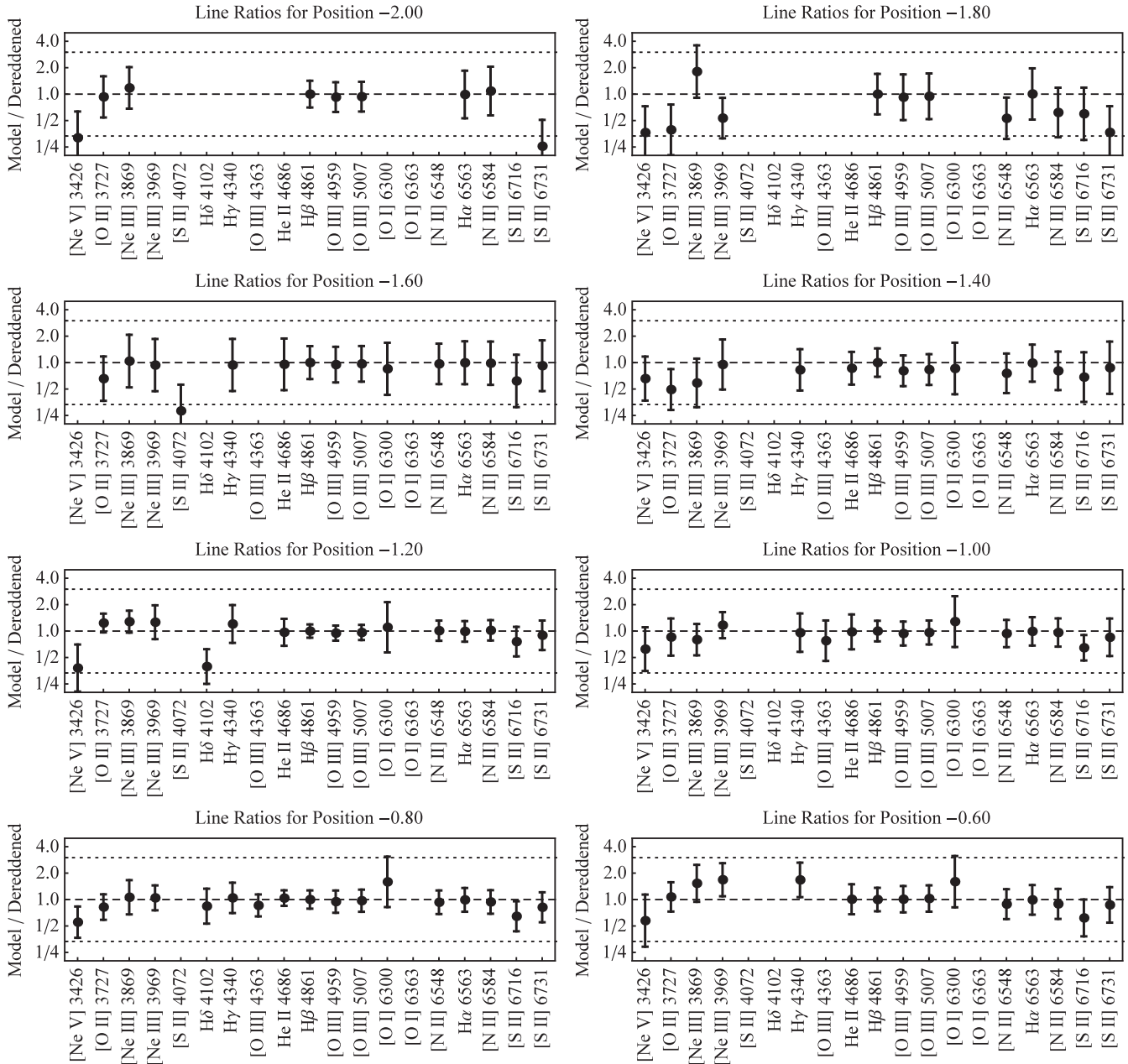


Figure A1. Composite model line ratios divided by the dereddened values (Table 4) for each position (see Section 4). The dashed unity lines indicate an exact match between the model and data, while the dotted lines are factor of 3 boundaries. The vertical tick marks are logarithmically spaced for even distribution around the unity line. Points above this line are overpredicted, while points below are underpredicted by the model.

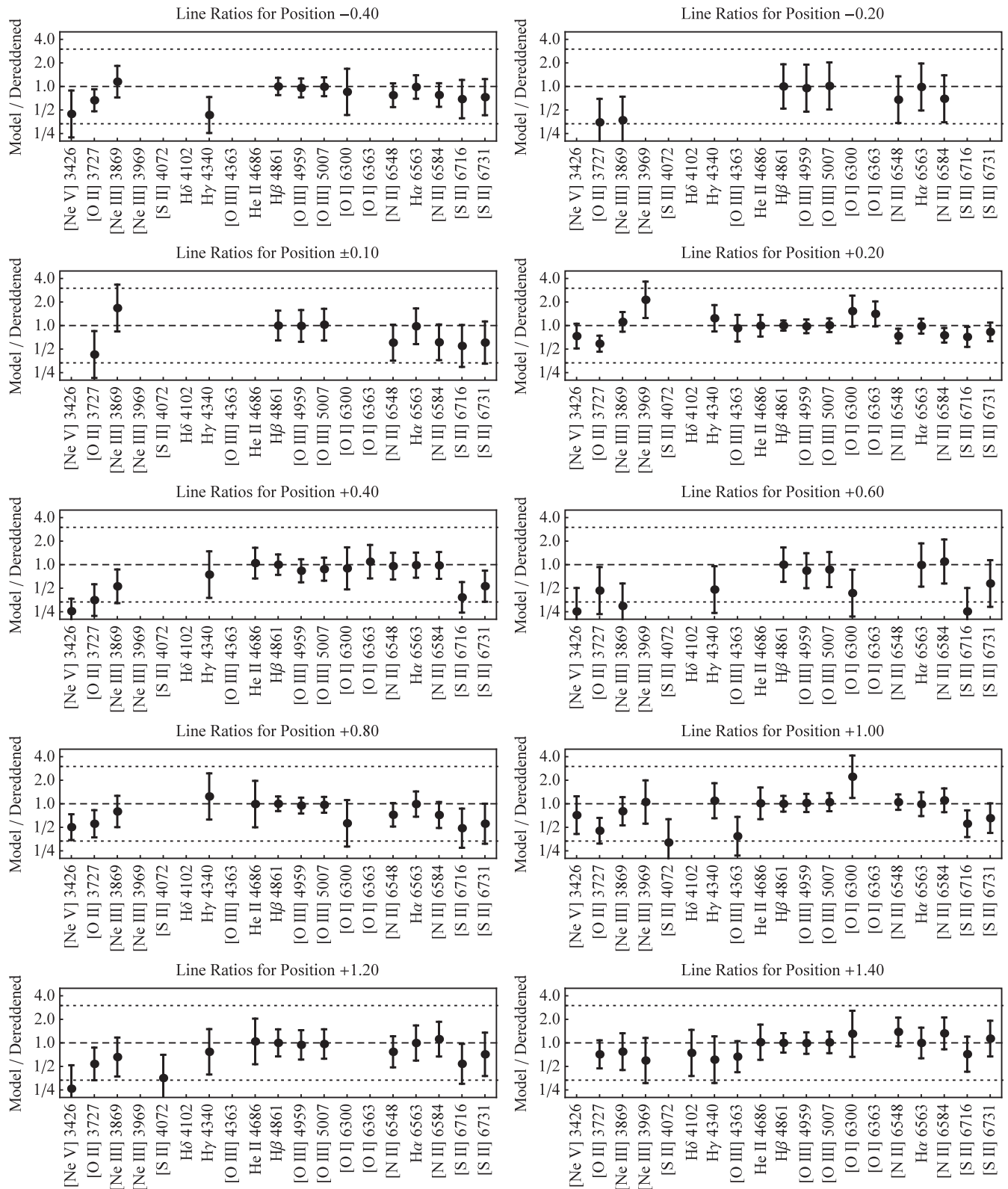


Figure A1. (Continued.)

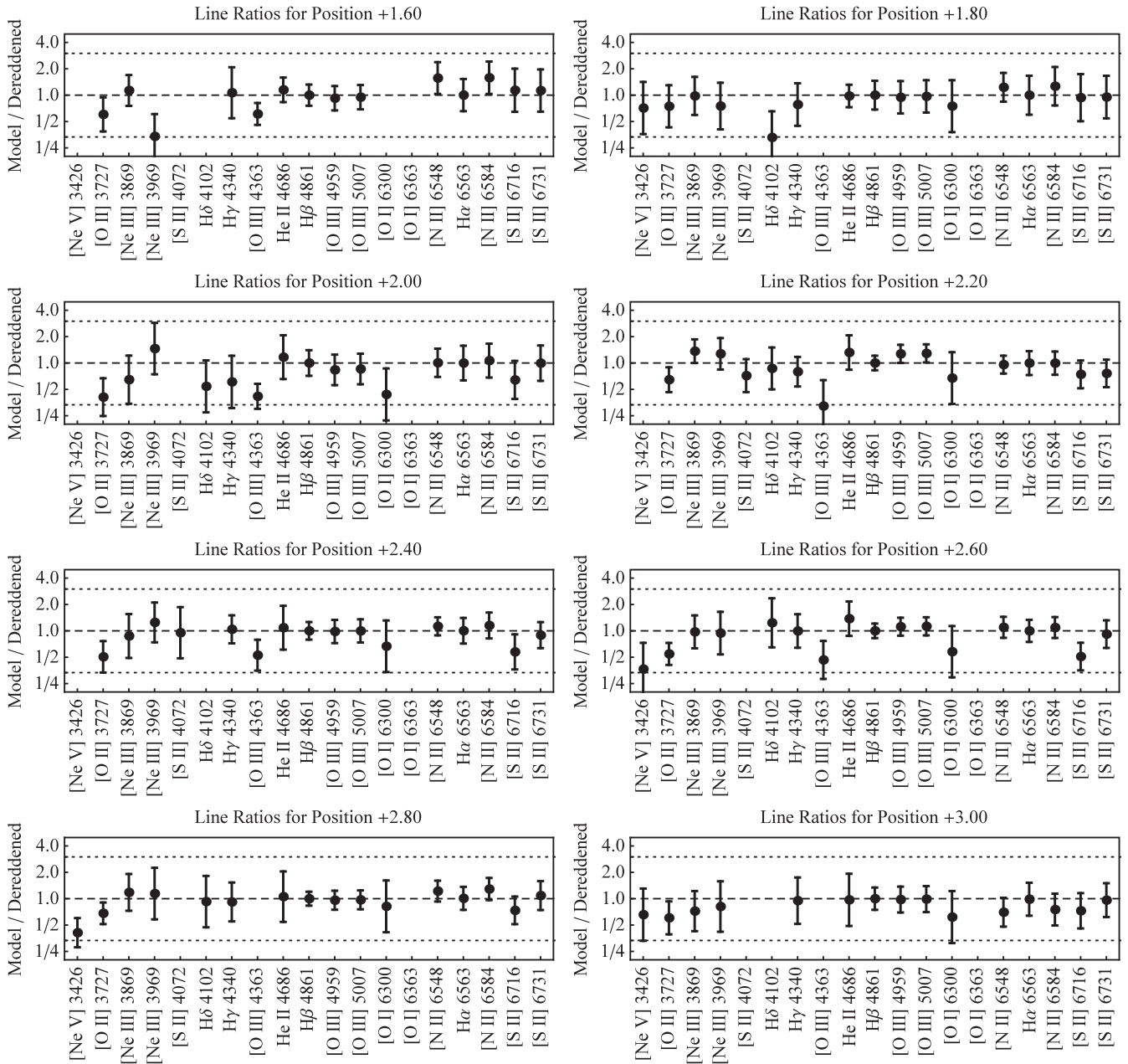


Figure A1. (Continued.)

Table A1
Radial Mass Outflow and Energetic Results

Distance (pc) (1)	Velocity (km s ⁻¹) (2)	Mass (log M _⊙) (3)	\dot{M} (M _⊙ yr ⁻¹) (4)	Energy (log erg) (5)	\dot{E} (log erg s ⁻¹) (6)	Momentum (log dyne s) (7)	\dot{p} (log dyne) (8)
NGC 4151							
12.8	106.6	0.03 ± 0.01	0.04 ± 0.01	50.57 ± 0.19	38.18 ± 0.19	43.85 ± 0.19	31.46 ± 0.19
21.4	178.3	0.07 ± 0.01	0.14 ± 0.02	51.31 ± 0.19	39.15 ± 0.19	44.36 ± 0.19	32.20 ± 0.19
29.9	249.1	0.14 ± 0.02	0.42 ± 0.05	51.94 ± 0.19	39.92 ± 0.19	44.85 ± 0.19	32.82 ± 0.19
38.4	319.9	0.20 ± 0.03	0.78 ± 0.10	52.31 ± 0.19	40.40 ± 0.19	45.11 ± 0.19	33.19 ± 0.19
47.0	391.5	0.25 ± 0.03	1.17 ± 0.16	52.58 ± 0.18	40.75 ± 0.18	45.28 ± 0.18	33.46 ± 0.18
55.5	462.3	0.32 ± 0.04	1.81 ± 0.24	52.84 ± 0.18	41.09 ± 0.18	45.47 ± 0.18	33.72 ± 0.18
64.1	534.0	0.45 ± 0.06	2.91 ± 0.39	53.11 ± 0.18	41.42 ± 0.18	45.68 ± 0.18	33.99 ± 0.18
72.6	604.8	0.41 ± 0.06	3.01 ± 0.43	53.18 ± 0.18	41.54 ± 0.18	45.70 ± 0.18	34.06 ± 0.18
81.2	676.4	0.33 ± 0.05	2.72 ± 0.45	53.18 ± 0.16	41.59 ± 0.16	45.65 ± 0.16	34.06 ± 0.16

Table A1
(Continued)









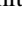

Distance (pc) (1)	Velocity (km s^{-1}) (2)	Mass ($\log M_{\odot}$) (3)	\dot{M} ($M_{\odot} \text{ yr}^{-1}$) (4)	Energy ($\log \text{ erg}$) (5)	\dot{E} ($\log \text{ erg s}^{-1}$) (6)	Momentum ($\log \text{ dyne s}$) (7)	\dot{p} ($\log \text{ dyne}$) (8)
89.7	747.2	0.27 ± 0.05	2.44 ± 0.42	53.18 ± 0.15	41.63 ± 0.15	45.60 ± 0.15	34.06 ± 0.15
98.3	793.5	0.19 ± 0.04	1.80 ± 0.41	53.07 ± 0.10	41.55 ± 0.10	45.47 ± 0.10	33.95 ± 0.10
106.8	771.1	0.10 ± 0.04	0.89 ± 0.33	52.75 ± 0.03	41.22 ± 0.03	45.17 ± 0.03	33.64 ± 0.03
115.3	748.8	0.08 ± 0.04	0.69 ± 0.32	52.63 ± 0.13	41.09 ± 0.13	45.06 ± 0.13	33.51 ± 0.13
123.9	726.1	0.09 ± 0.04	0.77 ± 0.35	52.66 ± 0.12	41.11 ± 0.12	45.10 ± 0.12	33.55 ± 0.12
132.4	703.8	0.07 ± 0.04	0.57 ± 0.38	52.52 ± 0.39	40.95 ± 0.39	44.98 ± 0.39	33.41 ± 0.39
NGC 1068							
14.4	1142.7	0.61 ± 0.08	4.92 ± 0.71	53.90 ± 0.18	42.31 ± 0.17	46.14 ± 0.18	34.55 ± 0.17
28.8	648.4	0.54 ± 0.04	2.50 ± 0.16	53.36 ± 0.24	41.52 ± 0.24	45.85 ± 0.24	34.01 ± 0.24
57.6	1029.9	1.24 ± 0.09	9.04 ± 0.65	54.12 ± 0.23	42.48 ± 0.24	46.40 ± 0.23	34.77 ± 0.24
72.0	1018.1	0.93 ± 0.17	6.75 ± 1.13	53.98 ± 0.15	42.34 ± 0.15	46.28 ± 0.15	34.64 ± 0.15
100.8	1509.9	0.70 ± 0.05	7.53 ± 0.48	54.20 ± 0.24	42.73 ± 0.25	46.32 ± 0.24	34.86 ± 0.25
129.6	915.7	0.23 ± 0.06	1.48 ± 0.43	53.28 ± 0.08	41.59 ± 0.04	45.62 ± 0.08	33.93 ± 0.04
Mrk 3							
0.0	6.7	0.05 ± 0.01	0.01 ± 0.01	48.32 ± 0.10	33.84 ± 0.06	42.80 ± 0.10	28.32 ± 0.06
65.1	1299.3	1.79 ± 0.43	3.65 ± 0.89	54.48 ± 0.09	42.29 ± 0.08	46.66 ± 0.09	34.47 ± 0.08
123.8	742.8	2.78 ± 0.20	3.24 ± 0.16	54.18 ± 0.24	41.75 ± 0.26	46.61 ± 0.24	34.18 ± 0.26
136.8	201.0	9.08 ± 3.65	2.86 ± 1.15	53.56 ± 0.07	40.56 ± 0.07	46.56 ± 0.07	33.56 ± 0.07
188.9	416.5	11.92 ± 0.52	7.79 ± 0.34	54.31 ± 0.26	41.63 ± 0.26	46.99 ± 0.26	34.31 ± 0.26
260.6	9.8	14.61 ± 1.88	0.22 ± 0.03	51.14 ± 0.19	36.83 ± 0.19	45.45 ± 0.19	31.14 ± 0.19
Mrk 573							
19.2	106.7	0.06 ± 0.01	0.02 ± 0.01	50.82 ± 0.18	37.78 ± 0.13	44.10 ± 0.18	31.06 ± 0.13
57.5	342.0	0.31 ± 0.04	0.28 ± 0.05	52.56 ± 0.19	40.02 ± 0.14	45.32 ± 0.19	32.78 ± 0.14
95.8	580.7	0.70 ± 0.09	1.08 ± 0.19	53.37 ± 0.19	41.06 ± 0.14	45.90 ± 0.19	33.60 ± 0.14
134.1	667.8	0.89 ± 0.11	1.58 ± 0.28	53.59 ± 0.19	41.35 ± 0.14	46.07 ± 0.19	33.82 ± 0.14
172.4	689.8	1.07 ± 0.14	1.97 ± 0.35	53.70 ± 0.19	41.47 ± 0.14	46.17 ± 0.19	33.93 ± 0.14
210.7	781.3	1.61 ± 0.20	3.35 ± 0.60	53.99 ± 0.19	41.81 ± 0.14	46.40 ± 0.19	34.22 ± 0.14
249.1	744.7	1.43 ± 0.18	2.84 ± 0.51	53.90 ± 0.19	41.70 ± 0.14	46.33 ± 0.19	34.13 ± 0.14
287.4	637.7	1.61 ± 0.20	2.74 ± 0.49	53.81 ± 0.19	41.54 ± 0.14	46.31 ± 0.19	34.04 ± 0.14
325.7	463.0	1.35 ± 0.17	1.67 ± 0.30	53.46 ± 0.19	41.05 ± 0.14	46.09 ± 0.19	33.69 ± 0.14
364.0	355.1	1.48 ± 0.19	1.41 ± 0.25	53.27 ± 0.19	40.75 ± 0.14	46.02 ± 0.19	33.50 ± 0.14
402.3	267.3	1.12 ± 0.14	0.80 ± 0.14	52.90 ± 0.19	40.26 ± 0.14	45.78 ± 0.19	33.13 ± 0.14
440.6	224.0	1.13 ± 0.14	0.67 ± 0.12	52.75 ± 0.19	40.03 ± 0.14	45.70 ± 0.19	32.98 ± 0.14
478.9	204.8	1.17 ± 0.15	0.64 ± 0.11	52.69 ± 0.19	39.93 ± 0.14	45.68 ± 0.19	32.92 ± 0.14
517.3	86.3	1.95 ± 0.25	0.45 ± 0.08	52.16 ± 0.19	39.02 ± 0.14	45.52 ± 0.19	32.39 ± 0.14
555.6	28.0	2.75 ± 0.35	0.21 ± 0.04	51.33 ± 0.19	37.71 ± 0.14	45.19 ± 0.19	31.56 ± 0.14
593.9	13.6	2.90 ± 0.37	0.11 ± 0.02	50.72 ± 0.19	36.78 ± 0.14	44.89 ± 0.19	30.95 ± 0.14
Mrk 78							
127.4	100.0	0.64 ± 0.22	0.05 ± 0.02	51.80 ± 0.02	38.20 ± 0.12	45.10 ± 0.02	31.50 ± 0.12
254.9	200.0	2.82 ± 0.99	0.45 ± 0.22	53.05 ± 0.02	39.75 ± 0.17	46.05 ± 0.02	32.75 ± 0.17
509.7	400.0	5.25 ± 1.84	1.66 ± 0.82	53.92 ± 0.02	40.92 ± 0.17	46.62 ± 0.02	33.62 ± 0.17
764.6	600.0	5.06 ± 1.77	2.40 ± 1.19	54.26 ± 0.02	41.43 ± 0.17	46.78 ± 0.02	33.96 ± 0.17
1019.5	800.0	10.38 ± 3.63	6.56 ± 3.25	54.82 ± 0.02	42.12 ± 0.17	47.22 ± 0.02	34.52 ± 0.17
1274.3	1000.0	11.80 ± 4.12	9.32 ± 4.60	55.07 ± 0.02	42.47 ± 0.17	47.37 ± 0.02	34.77 ± 0.17
1529.2	1200.0	6.97 ± 2.44	6.61 ± 3.27	55.00 ± 0.02	42.48 ± 0.17	47.22 ± 0.02	34.70 ± 0.17
1784.0	971.4	6.12 ± 2.14	4.70 ± 2.32	54.76 ± 0.02	42.15 ± 0.17	47.07 ± 0.02	34.46 ± 0.17
2038.9	742.9	7.39 ± 2.59	4.34 ± 2.15	54.61 ± 0.02	41.88 ± 0.17	47.04 ± 0.02	34.31 ± 0.17
2293.8	514.3	15.35 ± 5.36	6.24 ± 3.08	54.61 ± 0.02	41.72 ± 0.17	47.20 ± 0.02	34.31 ± 0.17
2548.6	384.0	7.17 ± 2.51	2.18 ± 1.08	54.02 ± 0.02	41.01 ± 0.17	46.74 ± 0.02	33.72 ± 0.17
2803.5	352.0	4.84 ± 1.69	1.35 ± 0.66	53.78 ± 0.02	40.72 ± 0.16	46.53 ± 0.02	33.48 ± 0.16
3058.4	320.0	11.05 ± 3.86	2.80 ± 1.38	54.05 ± 0.02	40.96 ± 0.17	46.85 ± 0.02	33.75 ± 0.17
3313.2	288.0	17.88 ± 6.25	4.07 ± 2.02	54.17 ± 0.02	41.03 ± 0.17	47.01 ± 0.02	33.87 ± 0.17
3568.1	256.0	8.24 ± 2.88	1.67 ± 0.83	53.73 ± 0.02	40.54 ± 0.17	46.62 ± 0.02	33.43 ± 0.17
3823.0	224.0	2.83 ± 0.99	0.50 ± 0.25	53.15 ± 0.01	39.90 ± 0.17	46.10 ± 0.01	32.85 ± 0.17

Table A1
(Continued)

Distance (pc) (1)	Velocity (km s ⁻¹) (2)	Mass (log M _⊙) (3)	\dot{M} (M _⊙ yr ⁻¹) (4)	Energy (log erg) (5)	\dot{E} (log erg s ⁻¹) (6)	Momentum (log dyne s) (7)	\dot{p} (log dyne) (8)
Mrk 34							
67.5	191.8	0.84 ± 0.13	0.12 ± 0.03	52.49 ± 0.17	39.15 ± 0.11	45.50 ± 0.17	32.17 ± 0.11
202.4	2347.9	2.26 ± 0.35	4.02 ± 0.88	55.09 ± 0.17	42.84 ± 0.11	47.02 ± 0.17	34.77 ± 0.11
337.4	1976.6	4.17 ± 0.64	6.24 ± 1.36	55.21 ± 0.17	42.89 ± 0.11	47.21 ± 0.17	34.89 ± 0.11
472.4	1789.2	9.18 ± 1.42	12.45 ± 2.72	55.47 ± 0.17	43.10 ± 0.11	47.51 ± 0.17	35.15 ± 0.11
607.3	1358.2	2.94 ± 0.45	3.03 ± 0.66	54.73 ± 0.17	42.25 ± 0.11	46.90 ± 0.17	34.41 ± 0.11
742.3	1108.4	2.51 ± 0.39	2.11 ± 0.46	54.49 ± 0.17	41.91 ± 0.11	46.74 ± 0.17	34.17 ± 0.11
877.2	46.0	1.15 ± 0.18	0.04 ± 0.01	51.38 ± 0.17	37.43 ± 0.10	45.02 ± 0.17	31.06 ± 0.10
1012.2	113.0	4.06 ± 0.63	0.35 ± 0.08	52.71 ± 0.17	39.15 ± 0.11	45.96 ± 0.17	32.39 ± 0.11
1147.1	368.6	13.20 ± 2.04	3.69 ± 0.81	54.25 ± 0.17	41.20 ± 0.11	46.99 ± 0.17	33.93 ± 0.11
1282.1	533.5	13.53 ± 2.09	5.47 ± 1.20	54.58 ± 0.17	41.69 ± 0.11	47.16 ± 0.17	34.26 ± 0.11
1417.0	350.7	23.01 ± 3.55	6.11 ± 1.34	54.45 ± 0.17	41.37 ± 0.11	47.21 ± 0.17	34.13 ± 0.11
1552.0	407.1	18.39 ± 2.84	5.67 ± 1.24	54.48 ± 0.17	41.47 ± 0.11	47.17 ± 0.17	34.16 ± 0.11
1687.0	440.4	16.17 ± 2.50	5.40 ± 1.18	54.49 ± 0.17	41.52 ± 0.11	47.15 ± 0.17	34.18 ± 0.11
1821.9	517.0	24.38 ± 3.77	9.55 ± 2.09	54.81 ± 0.17	41.91 ± 0.11	47.40 ± 0.17	34.49 ± 0.11
1956.9	538.7	19.68 ± 3.04	8.03 ± 1.76	54.75 ± 0.17	41.87 ± 0.11	47.32 ± 0.17	34.44 ± 0.11

Note. Numerical results for the mass and energetic quantities as functions of radial distance that are shown in Figures 11–14. The columns are (1) deprojected distance from the nucleus, (2) mass-weighted mean velocity of the outflowing kinematic components, (3) logarithmic gas mass, (4) mass outflow rates, (5) kinetic energies, (6) kinetic energy outflow rates, (7) momenta, and (8) momentum flow rates. The value at each distance is the quantity contained within the annuli of width δr as shown in Figure 9. Values for the last two rows of Mrk 78 are lower limits because the HST image does not fully cover the NLR emission.

ORCID iDs

Mitchell Revalski  <https://orcid.org/0000-0002-4917-7873>
 Beena Meena  <https://orcid.org/0000-0001-8658-2723>
 Francisco Martinez  <https://orcid.org/0000-0001-5099-8700>
 Garrett E. Polack  <https://orcid.org/0000-0001-5862-2150>
 D. Michael Crenshaw  <https://orcid.org/0000-0002-6465-3639>
 Steven B. Kraemer  <https://orcid.org/0000-0002-6928-9848>
 Nicholas R. Collins  <https://orcid.org/0000-0002-8837-8803>
 Travis C. Fischer  <https://orcid.org/0000-0002-3365-8875>
 Henrique R. Schmitt  <https://orcid.org/0000-0001-7376-8481>
 Judy Schmidt  <https://orcid.org/0000-0002-2617-5517>
 W. Peter Maksym  <https://orcid.org/0000-0002-2203-7889>
 Marc Rafelski  <https://orcid.org/0000-0002-9946-4731>

References

- Adams, T. F. 1973, *ApJ*, 179, 417
 Alonso-Herrero, A., Quillen, A. C., Rieke, G. H., Ivanov, V. D., & Efstathiou, A. 2003, *AJ*, 126, 81
 Antonucci, R. R. J., & Miller, J. S. 1985, *ApJ*, 297, 621
 Asplund, M., Grevesse, N., Sauval, A. J., & Scott, P. 2009, *ARA&A*, 47, 481
 Awaki, H., Koyama, K., Inoue, H., & Halpern, J. P. 1991, *PASJ*, 43, 195
 Bae, H.-J., Woo, J.-H., Karuzos, M., et al. 2017, *ApJ*, 837, 91
 Baldwin, J. A., Phillips, M. M., & Terlevich, R. 1981, *PASP*, 93, 5
 Barbosa, F. K. B., Storchi-Bergmann, T., McGregor, P., Vale, T. B., & Rogemar Riffel, A. 2014, *MNRAS*, 445, 2353
 Baron, D., & Netzer, H. 2019, *MNRAS*, 486, 4290
 Baron, D., Netzer, H., Davies, R. I., & Prochaska, J. X. 2020, *MNRAS*, 494, 5396
 Bentz, M. C., Denney, K. D., Cackett, E. M., et al. 2006, *ApJ*, 651, 775
 Bianchi, S., Chiaberge, M., Evans, D. A., et al. 2010, *MNRAS*, 405, 553
 Bianchi, S., Guainazzi, M., & Chiaberge, M. 2006, *A&A*, 448, 499
 Bischetti, M., Maiolino, R., Carniani, S., et al. 2019, *A&A*, 630, A59
 Bischetti, M., Piconcelli, E., Vietri, G., et al. 2017, *A&A*, 598, A122
 Bogdán, Á., Kraft, R. P., Evans, D. A., Andrade-Santos, F., & Forman, W. R. 2017, *ApJ*, 848, 61
 Buchner, J., Georgakakis, A., Nandra, K., et al. 2014, *A&A*, 564, A125
 Capetti, A., Macchetto, F., Sparks, W. B., & Boksenberg, A. 1994, *ApJ*, 421, 87
 Cardelli, J. A., Clayton, G. C., & Mathis, J. S. 1989, *ApJ*, 345, 245
 Catalán-Torrecilla, C., Castillo-Morales, Á., Gil de Paz, A., et al. 2020, *ApJ*, 890, 5
 Chen, J., Shi, Y., Dempsey, R., et al. 2019, *MNRAS*, 489, 855
 Cheung, E., Bundy, K., Cappellari, M., et al. 2016, *Natur*, 533, 504
 Ciotti, L., & Ostriker, J. P. 2001, *ApJ*, 551, 131
 Collins, N. R., Kraemer, S. B., Crenshaw, D. M., et al. 2005, *ApJ*, 619, 116
 Collins, N. R., Kraemer, S. B., Crenshaw, D. M., Bruhweiler, F. C., & Meléndez, M. 2009, *ApJ*, 694, 765
 Comerón, S., Knapen, J. H., Ramos Almeida, C., & Watkins, A. E. 2021, *A&A*, 645, 130
 Crenshaw, D. M., Fischer, T. C., Kraemer, S. B., & Schmitt, H. R. 2015, *ApJ*, 799, 83
 Crenshaw, D. M., & Kraemer, S. B. 2000, *ApJ*, 532, 247
 Crenshaw, D. M., & Kraemer, S. B. 2012, *ApJ*, 753, 75
 Crenshaw, D. M., Kraemer, S. B., Schmitt, H. R., et al. 2010a, *AJ*, 139, 871
 Crenshaw, D. M., Schmitt, H. R., Kraemer, S. B., Mushotzky, R. F., & Dunn, J. P. 2010b, *ApJ*, 708, 419
 Cresci, G., & Maiolino, R. 2018, *NatAs*, 2, 179
 Das, V., Crenshaw, D. M., Hutchings, J. B., et al. 2005, *AJ*, 130, 945
 Das, V., Crenshaw, D. M., Kraemer, S. B., & Deo, R. P. 2006, *AJ*, 132, 620
 Davies, R., Baron, D., Shimizu, T., et al. 2020, *MNRAS*, 498, 4150
 De Robertis, M. M. 1987, *ApJ*, 316, 597
 Di Matteo, T., Springel, V., & Hernquist, L. 2005, *Natur*, 433, 604
 Dors, O. L., Maiolino, R., Cardaci, M. V., et al. 2020, *MNRAS*, 496, 3209
 Durré, M., & Mould, J. 2018, *ApJ*, 867, 149
 Durré, M., & Mould, J. 2019, *ApJ*, 870, 37
 Ferland, G. J., & Osterbrock, D. E. 1986, *ApJ*, 300, 658
 Ferland, G. J., Porter, R. L., van Hoof, P. A. M., et al. 2013, *RMxAA*, 49, 137
 Feroz, F., & Hobson, M. P. 2008, *MNRAS*, 384, 449
 Feroz, F., Hobson, M. P., & Bridges, M. 2009, *MNRAS*, 398, 1601
 Feroz, F., Hobson, M. P., Cameron, E., & Pettitt, A. N. 2019, *OJAp*, 2, 10
 Fiore, F., Feruglio, C., Shankar, F., et al. 2017, *A&A*, 601, A143
 Fischer, T. C., Crenshaw, D. M., Kraemer, S. B., et al. 2011, *ApJ*, 727, 71
 Fischer, T. C., Crenshaw, D. M., Kraemer, S. B., & Schmitt, H. R. 2013, *ApJS*, 209, 1
 Fischer, T. C., Crenshaw, D. M., Kraemer, S. B., Schmitt, H. R., & Turner, T. J. 2014, *ApJ*, 785, 25
 Fischer, T. C., Kraemer, S. B., Schmitt, H. R., et al. 2018, *ApJ*, 856, 102
 Fischer, T. C., Machuca, C., Diniz, M. R., et al. 2017, *ApJ*, 834, 30
 Fluetsch, A., Maiolino, R., Carniani, S., et al. 2019, *MNRAS*, 483, 4586

- Fluetsch, A., Maiolino, R., Carniani, S., et al. 2020, arXiv:2006.13232
- Förster Schreiber, N. M., Übler, H., Davies, R. L., et al. 2019, *ApJ*, **875**, 21
- Gandhi, P., Lansbury, G. B., Alexander, D. M., et al. 2014, *ApJ*, **792**, 117
- García-Bernete, I., Alonso-Herrero, A., García-Burillo, S., et al. 2021, *A&A*, **645**, 21
- García-Burillo, S., Combes, F., Usero, A., et al. 2014, *A&A*, **567**, A125
- Gaspari, M., Tombesi, F., & Cappi, M. 2020, *NatAs*, **4**, 10
- Gnilka, C. L., Crenshaw, D. M., Fischer, T. C., et al. 2020, *ApJ*, **893**, 80
- González Delgado, R. M., Heckman, T., & Leitherer, C. 2001, *ApJ*, **546**, 845
- Gonzalez-Martín, O., Acosta-Pulido, J. A., Perez Garcia, A. M., & Ramos Almeida, C. 2010, *ApJ*, **723**, 1748
- Greene, J. E., Zakamska, N. L., Ho, L. C., & Barth, A. J. 2011, *ApJ*, **732**, 9
- Hainline, K. N., Hickox, R. C., Greene, J. E., et al. 2014, *ApJ*, **787**, 65
- Harrison, C. M., Costa, T., Tadhunter, C. N., et al. 2018, *NatAs*, **2**, 198
- Heckman, T. M., & Best, P. N. 2014, *ARA&A*, **52**, 589
- Heckman, T. M., Kauffmann, G., Brinchmann, J., et al. 2004, *ApJ*, **613**, 109
- Hopkins, P. F., & Elvis, M. 2010, *MNRAS*, **401**, 7
- Hopkins, P. F., Hernquist, L., Cox, T. J., et al. 2005, *ApJ*, **630**, 705
- Jackson, N., & Beswick, R. J. 2007, *MNRAS*, **376**, 719
- Jaffe, W., Meisenheimer, K., Röttgering, H. J. A., et al. 2004, *Natur*, **429**, 47
- Jin, C., Ward, M., & Done, C. 2012, *MNRAS*, **425**, 907
- Joye, W. A., & Mandel, E. 2003, in ASP Conf. Ser. 295, *Astronomical Data Analysis Software and Systems XII*, ed. H. E. Payne, R. I. Jedrzejewski, & R. N. Hook (San Francisco, CA: ASP), 489
- Kakkad, D., Groves, B., Dopita, M., et al. 2018, *A&A*, **618**, A6
- Kakkad, D., Mainieri, V., Vietri, G., et al. 2020, *A&A*, **642**, 147
- Kang, D., & Woo, J.-H. 2018, *ApJ*, **864**, 124
- Karouzos, M., Woo, J.-H., & Bae, H.-J. 2016, *ApJ*, **833**, 171
- Kauffmann, G., Heckman, T. M., Tremonti, C., et al. 2003, *MNRAS*, **346**, 1055
- Kennicutt, R. C. 1998, *ApJ*, **498**, 541
- Kewley, L. J., Dopita, M. A., Sutherland, R. S., Heisler, C. A., & Trevena, J. 2001, *ApJ*, **556**, 121
- Kewley, L. J., Groves, B., Kauffmann, G., & Heckman, T. 2006, *MNRAS*, **372**, 961
- Kewley, L. J., Nicholls, D. C., Sutherland, R., et al. 2019, *ApJ*, **880**, 16
- Kormendy, J., & Ho, L. C. 2013, *ARA&A*, **51**, 511
- Kozlova, D. V., Moiseev, A. V., & Smirnova, A. A. 2020, *CoSka*, **50**, 309
- Kraemer, S. B., & Crenshaw, D. M. 2000a, *ApJ*, **532**, 256
- Kraemer, S. B., & Crenshaw, D. M. 2000b, *ApJ*, **544**, 763
- Kraemer, S. B., Crenshaw, D. M., Hutchings, J. B., et al. 2000, *ApJ*, **531**, 278
- Kraemer, S. B., Sharma, N., Turner, T. J., George, I. M., & Crenshaw, D. M. 2015, *ApJ*, **798**, 53
- Kraemer, S. B., Turner, T. J., Couto, J. D., et al. 2020, *MNRAS*, **493**, 3893
- Lacerda, E. A. D., Sánchez, S. F., Cid Fernandes, R., et al. 2020, *MNRAS*, **492**, 3073
- Laha, S., Reynolds, C. S., Reeves, J., et al. 2021, *NatAs*, **5**, 13
- Leung, G. C. K., Coil, A. L., Aird, J., et al. 2019, *ApJ*, **886**, 11
- Liu, G., Zakamska, N. L., Greene, J. E., Nesvadba, N. P. H., & Liu, X. 2013, *MNRAS*, **430**, 2327
- Liu, Z. W., Zhang, J. S., Henkel, C., et al. 2017, *MNRAS*, **466**, 1608
- Luo, R., Woo, J.-H., Karouzos, M., et al. 2020, arXiv:2012.10065
- Lutz, D., Sturm, E., Janssen, A., et al. 2020, *A&A*, **633**, A134
- Ma, J., Maksym, W. P., Fabbiano, G., et al. 2021, *ApJ*, **908**, 155
- Maksym, W. P., Fabbiano, G., Elvis, M., et al. 2016, *ApJ*, **829**, 46
- Maksym, W. P., Fabbiano, G., Elvis, M., et al. 2017, *ApJ*, **844**, 69
- Maksym, W. P., Fabbiano, G., Elvis, M., et al. 2019, *ApJ*, **872**, 94
- May, D., Steiner, J., Menezes, R. B., & Ricci, T. V. 2014, *RMxAC*, **44**, 193
- May, D., & Steiner, J. E. 2017, *MNRAS*, **469**, 994
- May, D., Steiner, J. E., Menezes, R. B., Williams, D. R. A., & Wang, J. 2020, *MNRAS*, **496**, 1488
- McMaster, M. 2008, *Wide Field and Planetary Camera 2 Instrument Handbook v.10.0* (Baltimore, MD: Space Telescope Science Institute)
- Menci, N., Fiore, F., Feruglio, C., et al. 2019, *ApJ*, **877**, 74
- Mingozi, M., Cresci, G., Venturi, G., et al. 2019, *A&A*, **622**, A146
- Morganti, R. 2017, *FRASS*, **4**, 42
- Mosallanezhad, A., Yuan, F., Ostriker, J. P., Zeraatgari, F. Z., & Bu, D.-F. 2019, *MNRAS*, **490**, 2567
- Noordermeer, E., van der Hulst, J. M., Sancisi, R., Swaters, R. A., & van Albada, T. S. 2005, *A&A*, **442**, 137
- Oh, K., Sarzi, M., Schawinski, K., & Yi, S. K. 2011, *ApJS*, **195**, 13
- Oke, J. B. 1990, *AJ*, **99**, 1621
- Osterbrock, D. E., & Ferland, G. J. 2006, *Astrophysics of Gaseous Nebulae and Active Galactic Nuclei* (Mill Valley, CA: Univ. Science Books)
- Pedlar, A., Meaburn, J., Axon, D. J., et al. 1989, *MNRAS*, **238**, 863
- Perna, M., Lanzuisi, G., Brusa, M., Mignoli, M., & Cresci, G. 2017, *A&A*, **603**, A99
- Peterson, B. M. 1997, *An Introduction to Active Galactic Nuclei* (Cambridge: Cambridge Univ. Press)
- Pogge, R. W., & De Robertis, M. M. 1993, *ApJ*, **404**, 563
- Ramos Almeida, C., Pérez García, A. M., Acosta-Pulido, J. A., et al. 2006, *ApJ*, **645**, 148
- Revalski, M. 2019, PhD thesis, Georgia State Univ. https://scholarworks.gsu.edu/phy_astr_diss/114
- Revalski, M., Crenshaw, D. M., Kraemer, S. B., et al. 2018a, *ApJ*, **856**, 46
- Revalski, M., Dashtamirova, D., Crenshaw, D. M., et al. 2018b, *ApJ*, **867**, 88
- Riley, A. 2017, *STIS Instrument Handbook for Cycle 25, Version 16.0* (Baltimore, MD: Space Telescope Science Institute)
- Roberts-Borsani, G. W., & Saintonge, A. 2019, *MNRAS*, **482**, 4111
- Rojas, A. F., Sani, E., Gavignaud, I., et al. 2020, *MNRAS*, **491**, 5867
- Rosario, D. J., Burtscher, L., Davies, R. I., et al. 2018, *MNRAS*, **473**, 5658
- Rosario, D. J., Togi, A., Burtscher, L., et al. 2019, *ApJL*, **875**, L8
- Rosario, D. J. V. 2007, PhD thesis, Univ. Virginia
- Rose, M., Tadhunter, C., Ramos Almeida, C., et al. 2018, *MNRAS*, **474**, 128
- Ruiz, J. R., Crenshaw, D. M., Kraemer, S. B., et al. 2001, *AJ*, **122**, 2961
- Savage, B. D., & Mathis, J. S. 1979, *ARA&A*, **17**, 73
- Schmitt, H. R., Donley, J. L., Antonucci, R. R. J., et al. 2003, *ApJ*, **597**, 768
- Schmitt, H. R., & Kinney, A. L. 2000, *ApJS*, **128**, 479
- Schmitt, H. R., Kinney, A. L., Calzetti, D., & Storchi Bergmann, T. 1997, *AJ*, **114**, 592
- Seab, C. G., & Shull, J. M. 1983, *ApJ*, **275**, 652
- Shimizu, T. T., Davies, R. I., Lutz, D., et al. 2019, *MNRAS*, **490**, 5860
- Smith, K. L., Koss, M., Mushotzky, R., et al. 2020, *ApJ*, **904**, 83
- Snow, T. P., & Witt, A. N. 1996, *ApJL*, **468**, L65
- Storchi-Bergmann, T., Dall'Agnol de Oliveira, B., Longo Micchi, L. F., et al. 2018, *ApJ*, **868**, 14
- Storchi-Bergmann, T., Lopes, R. D. S., McGregor, P. J., et al. 2010, *MNRAS*, **402**, 819
- Storchi-Bergmann, T., Schmitt, H. R., Calzetti, D., & Kinney, A. L. 1998, *AJ*, **115**, 909
- Storchi-Bergmann, T., & Schnorr-Müller, A. 2019, *NatAs*, **3**, 48
- Sun, A.-L., Greene, J. E., Zakamska, N. L., et al. 2018, *MNRAS*, **480**, 2302
- Swinbank, A. M., Harrison, C. M., Tiley, A. L., et al. 2019, *MNRAS*, **487**, 381
- Takeo, E., Inayoshi, K., & Mineshige, S. 2020, *MNRAS*, **497**, 302
- Tody, D. 1986, *Proc. SPIE*, **627**, 733
- Tody, D. 1993, in ASP Conf. Ser. 52, *Astronomical Data Analysis Software and Systems II*, ed. R. J. Hanisch, R. J. V. Brissenden, & J. Barnes (San Francisco, CA: ASP), 173
- Trindade Falcão, A., Kraemer, S. B., Fischer, T. C., et al. 2021, *MNRAS*, **500**, 1491
- Tully, R. B., Shaya, E. J., Karachentsev, I. D., et al. 2008, *ApJ*, **676**, 184
- Ulvestad, J. S., & Wilson, A. S. 1984, *ApJ*, **278**, 544
- van Dokkum, P. G. 2001, *PASP*, **113**, 1420
- Van Rossum, G., & Drake, F. L. 2009, *Python 3 Reference Manual* (Scotts Valley, CA: CreateSpace)
- Veilleux, S., Maiolino, R., Bolatto, A. D., & Aalto, S. 2020, *A&ARv*, **28**, 2
- Veilleux, S., & Osterbrock, D. E. 1987, *ApJS*, **63**, 295
- Venturi, G., & Marconi, A. 2020, arXiv:2006.11215
- Venturi, G., Nardini, E., Marconi, A., et al. 2018, *A&A*, **619**, A74
- Wang, J., Fabbiano, G., Elvis, M., et al. 2011a, *ApJ*, **736**, 62
- Wang, J., Fabbiano, G., Elvis, M., et al. 2011c, *ApJ*, **742**, 23
- Wang, J., Fabbiano, G., Risaliti, G., et al. 2011b, *ApJ*, **729**, 75
- Wang, J.-M., Chen, Y.-M., Yan, C.-S., Hu, C., & Bian, W.-H. 2007, *ApJL*, **661**, L143
- Whittle, M., Pedlar, A., Meurs, E. J. A., et al. 1988, *ApJ*, **326**, 125
- Whittle, M., Rosario, D. J., Silverman, J. D., Nelson, C. H., & Wilson, A. S. 2005, *AJ*, **129**, 104
- Whittle, M., & Wilson, A. S. 2004, *AJ*, **127**, 606
- Wilson, A. S., Ward, M. J., & Haniff, C. A. 1988, *ApJ*, **334**, 121
- Woo, J.-H., & Urry, C. M. 2002, *ApJ*, **579**, 530
- Wylezalek, D., Flores, A. M., Zakamska, N. L., Greene, J. E., & Riffel, R. A. 2020, *MNRAS*, **492**, 4680
- Yesuf, H. M., Faber, S. M., Koo, D. C., et al. 2020, *ApJ*, **889**, 14
- Yuan, W., Fausnaugh, M., Hoffmann, S., et al. 2020, *ApJ*, **902**, 26
- Zhuang, M.-Y., & Ho, L. C. 2020, *ApJ*, **896**, 108
- Zinger, E., Pillepich, A., Nelson, D., et al. 2020, *MNRAS*, **499**, 768